Artificial Intelligence & Sustainable Materials

Vol 1 Iss 1
ISSN pending

Mason Publish Group

Artificial Intelligence and Sustainable Materials

This journal is published in collaboration with Mason Publish Group and Wuhan University of Technology.

To foster a deeper understanding of how materials principles intersect with digital innovation and enable transformative changes in technology, society, and the global economy, the Journal of Artificial Intelligence and Sustainable Materials aims to publish theoretical and applied investigations on sustainable materials by employing artificial intelligence techniques (AI). The journal is a forum for discussion of research on optimized design, production and manufacture, properties evaluations, modeling and computational calculation of sustainable materials based on AI techniques.

PUBLISHER

Journal of Artificial Intelligence and Sustainable Materials is published by Mason Publish Group, Seattle, USA; editorialoffice@masonpublish.org. For submission instructions, subscription and all other information visit: https://masonpublish.org.

COPYRIGHT AND LICENSING

DISCLAIMER

ONLINE OPEN

Artificial Intelligence and Sustainable Materials accepts articles for Open Access publication. Please visit https://masonpublish.org for further information about Online Open.

Editor-in-Chief:

Associate Editors:

Advisory Board:

Artificial Intelligence and Sustainable Materials

Volume 1 2025

Articles

The impact of Cement Mortar Reinforced with Recycled Polyethylene for Construction Applications in Tropical Regions

Moses K. Flomo[1], Salifu T. Azeko[2*], Jamal-Deen Kukura[3], Kabiru Mustapha[4], Ebenezer Annan[5] and Benjamin Agyei-Tuffour[6]

[1]Lecturer, Department of Chemistry, Cuttington University, Suakoko, Liberia. Email: mflomo1989@gmail.com

[2*]Senior Lecturer, Department of Mechanical Engineering, Tamale Technical University, Tamale, Ghana. Email: azekotahiru@gmail.com

[3]Lecturer, Department of Mechanical Engineering, Tamale Technical University, Tamale, Ghana. Email: 2gsjamal@gmail.com

[4]Senior Lecturer, Department of Materials Science and Engineering, Kwara State University, Malete, Nigeria. Email: mustkabir@gmail.com

[5]Senior Lecturer, Department of Materials Science and Engineering, University of Ghana, Legon, Accra, Ghana. Email: ebenk45@gmail.com

[6]Senior Lecturer, Department of Materials Science and Engineering, University of Ghana, Legon, Accra, Ghana. Email: bagyeituffour@gmail.com

Abstract

This current research work combines both experimental and theoretical study of the impact of cement mortar reinforced with recycled polyethylene for applications in the tropical regions. The work explores incorporating low density polyethylene (LDPE) waste into cement mortar to improve its fracture toughness and flexural strength with balanced compressive strength. Different volume fractions (0, 5, 10, 15, 20, 30, and 40 %) of the powdered LDPE were mixed with cement and the density, compressive strength, flexural strength, and the fracture toughness were observed under different testing conditions. All specimens were tested after curing of 7, 14, and 28 days. The results show that there was ~6 % increase in the fracture toughness at 5 vol. %, ~7 % increase at 10 vol. %, and 24 vol. % increases at 20 vol. % of LDPE. Also, it was observed that the weight and compressive strength decreased with increasing volume fraction up to 40 vol. % of LDPE waste. The results for the survival/failure probability show that the PE-mortar composites with PE volume percentages up to 20 vol. % had the highest survival probability. The composite with this volume percentage can withstand crackup to 7 mm, with a survival probability of 0.6.

Keywords: Polyethylene; Survival/Failure probability; Brittle fracture modelling, Mechanical testing; Crack opening tip displacement

1 Introduction

The collapse of buildings poses major challenges and threats to the health and wellbeing of the human race worldwide. Over time, major damages have been reported resulting in expansive loss of huge investments in housing and properties (Blunden 2016), with many people losing their lives. In most cases, people have sleepless nights and state of unrest. The world is, however, relatively unstable as a result of the geometrical order of population growth, urban development in coastal areas, poor planning and housing developments in high risk areas of cities (Davy 2009).

Furthermore, researchers and engineers throughout West Africa have shown that building collapses occurs to a diversity of factors (Opara 2007). Some of these factors include but not limited to employment of incompetent artisans (Opara 2007; Michael and Razak 2013), weak work supervision of workmen at building sites, endemic poor work ethics and non-enforcement of existing laws (Opara 2007; Michael and Razak 2013). Research carried out by Michael and Razak (2013) showed that cases of building collapse are not restricted by climatology or level of urbanization since these cut across cultural and ethnical barriers. Additionally, other main causes and major challenges have being attributed to non-compliance with specifications standards a well as using of sub-standard building materials and equipment (Yilidirim and Sengul 2011; Siegel et al. 2013). In line with this non-compliance or use of sub-standard material, the type and quality of cement used in concrete structures plays a significant role in building and constructions. Furthermore, concrete ability to withstand certain loads has significant impact on its durability. There is, therefore a need to investigate the quality of materials used in making the concrete for construction in the Africa and the world at large (Siegel et al. 2013).

Globally, Cements often used as binders are very expensive for the construction of modern buildings. This binder is not environmental friendly and therefore, there is the need to substitute whole or part of this polluting cement with materials that can be recycled. Recently, a couple ofworks have been carried out to fully or partially replace industrial cement with several natural and artificial wastes (Tonoli et al. 2007; Setién et al. 2009; Terzietć al. 2013; Bouasker et al. 2014; Gesoğlu et al., 2014; Mustapha et al. 2015; Azeko et al. 2016a; Azeko et al. 2016b; Mustapha et al. 2016; Azeko et al. 2018) for composite processing in building applications. These recycled materials including polyethylene (Azeko et al. 2016a) and natural straws (Mustapha et al. 2015) in cement have shown to possess excellent compressive strengths, flexural strengths, fracture toughness, and erosion resistance that are comparable to cement-based structures produced from sea/river sand.

Although these research methods have greatly influenced the mechanical and physical properties of reinforced bricks/blocks, there is still the need to provide more insight into the solving of cracking and failure associated problems in the building and construction industries. This work therefore recycled waste polyethylene into pellets and mixed with cement mortar to produce polyethylene-cement composites in different proportions for sustainable building applications.

2 Modelling

2.1 Modeling of Brittle Fracture

Assuming linear elastic fracture mechanics (LEFM) conditions are applicable in polymer- reinforced composites, the stress distribution, σ_{ij} ahead of a crack that is dominant and causes failure in these composites could be estimated from (Azeko et al. 2016b):

$$\sigma_{ij} = \frac{K_I}{\sqrt{2\pi r}} f(\theta) \tag{1}$$

where K_I is the stress intensity factor, while r and θ are the polar coordinates from the crack-tip, and *f*(θ) depends on the mode of loading (Azeko et al. 2016b). Also, assuming that the distribution of size of the plastic reinforcement can be compared to the distribution of size of inclusions ahead ofthe crack-tip, then the indigenous circumstances for interfacial cracking de-cohesion can be expressed as (Azeko et al. 2016b; Soboyejo 2007):

$$\sigma_c = \frac{\pi E_m G_m}{(1-v_m^2)\, d_c} \tag{2}$$

where E_m represents the Elastic/Young's modulus of the matrix, G_m is the matrix fracture energy, v_m is the matrix poison's ratio, whereas d is the critical diameter of the particle. Since the disparities in the particle sizes are known from experiments, the discrepancies in the particle strengths can be related directly to the variations in particle strength.

Furthermore, the puniest link statistics could be used to determine the probability of failure or survival within the fracture process zone. The probability of failure within the process zone is expressed as (Soboyejo 2002; Fashina et al. 2017):

$$\Delta\phi = 1 - \exp\left[-\Delta v \int_0^s g(\sigma)d\sigma\right] \tag{3}$$

Where Δv the incremental volume, g is represents the strength distribution, σ denote the strength and s is the applied stress. Therefore, survival probability is given by:

$$\Phi = 1 - \exp\left[-\int_0^v dv \int_0^s g(\sigma)d\sigma\right] \tag{4}$$

where v is the volume of the process zone and g(σ)dσ is the elemental strength distribution proposed by Weibull (Weibull 1951) and given by (Azeko et al. 2016b) to be:

$$\int_0^s g(\sigma)d\sigma = \left(\frac{s - s_u}{s_0}\right)^m Z_f N_1 \tag{5}$$

where mis the Weibull modulus or shape parameter, S_u is the particle strength of lower bound, Zf is the fraction of particles that partakes in the fracture process and N_I is the number of particles in one unit volume. Therefore, since the size distribution of particles is known with the stress distribution within the process zone, the failure probabilities can be calculated directly from equations 5. In the case of brittle fracture under linear elastic fracture conditions, the failure probability for linear elastic conditions can be obtained by applying the Hutchinson-Rice- Rosengreen (HRR) conditions. From the HRR approach, the crack-tip field is given by:

$$\frac{s_{ij}}{s_{ys}} = \left[\frac{EJ}{\alpha s_{ys}^2 I_n r}\right]^{\frac{1}{n+1}} \tilde{s}_{ij}^{\,n+1}(n,\theta) \tag{6}$$

where E represents the Young's modulus, J is the J integral, S_{ys} denote the yield stress, n is the strain hardening exponent and I_n is a constant of integration dependent on n and stress state. If we now assume that weak link statistics prevail, the survival probability in the elemental volume is given by (Weibull 1951):

$$P_s\left(\bar{s}_i\right) = \exp\left[-\Delta v_i \left(\frac{\bar{s}_i - s_u}{s_0}\right)^m\right] \tag{7}$$

where Δv_i is the volume of the plastic zone, s_u represents the lower bound strength , s_o is the mean strength and $\bar{s}_i$ is the annular element average stress component. When Δv_i is close to zero, the average stress is equal to s atr.

If we now assume that the survival probability in the first annular element is regarded as P_1 and the second annular element is P_2 and soon, then one can estimate the survival probability in the fracture process zone with z annular volumes as

$$P_s(z) = P_s(1).P_s(2).P_s(3)...P_s(z) \tag{8}$$

Therefore, substituting equation 7 into 8 yields:

$$P_s(z) = \prod_{i=1}^{z} \exp\left[-\Delta v_i \left(\frac{s_i - s_u}{s_o}\right)\right]^m \tag{9}$$

Equation 19 can be simplified andre-written as:

$$P_s(z) = \exp\left[-\Delta v_i \sum_{i=1}^{k} \left(\frac{s_i - s_u}{s_o}\right)^m\right] \tag{10}$$

Hence, the Total Survival Probability can now be expressed in integral form as:

$$P_s(r) = \exp\left[-2B\beta f N \int_0^{\pi} \int_{r_o}^{r_p} \left(\frac{s - s_u}{s_o}\right)^m r dr d\theta\right] \tag{11}$$

where r_o is the radial distance at which HRR stresses are truncated by crack-tip blunting and r_p is the plastic zone size which is given by:

$$r_p = \lambda \left(\frac{K_I}{s_{ys}}\right)^2 \tag{12}$$

where K_I is the stress intensity factor and S_{ys} is the yield stress. The crack tip opening displacement (CTOD), Δ, is given by:

$$\Delta = d_n s_{ys} K_I^2 / E' \tag{13}$$

where $E' = E / (1-v^2)$ for plain strain conditions and $E' = E$ for plane stress conditions. The parameter d_n is given by:

$$d_n = 2\tilde{\mu}_{ij}(\pi, n)\left[\frac{\alpha s_y}{E'}\left(\tilde{\mu}_x(\pi, n) + \tilde{\mu}_y(\pi, n)\right)\right]^{\frac{1}{n}} \tag{14}$$

where $\tilde{\mu}_x$ *(π, n)* and $\tilde{\mu}_y$ *(π, n)* are functions of n, and the other constants have their usual meanings. Using atypical value of dn of 0.5 and substituting equation 13 into 12 gives:

$$r_p = \lambda \frac{E\delta}{d_n\left(1-\nu\right)s_{ys}} \tag{15}$$

Hence, the total failure probability, Φ, is given by (Azeko et al. 2016b; Soboyejo 2007):

$$\Phi = 1 - P_s(r) = 1 - \exp\left[-2B\beta f N \int_0^{\pi}\int_{r_o}^{r^p}\left(\frac{s-s_u}{s_o}\right)^m r dr d\theta\right] \tag{16}$$

3 Experimental Procedures

3.1 Production of Low Density Polyethylene Pellets

Waste water sachets classified as linear low density polyethylene found littering everywhere were collected in huge quantity from streets, market place, dumpsite, etc. Detergents such as tween 80 and sodium dodecyl sulphate were used to wash the water sachets to remove microbes and other dirty substances. The plastics were then dried in the sun for about two hours to remove moisture. A hot plate was plugged to provide heat. Kerosene was placed on the hot plate. It was heated for about one hour thirty minutes until it reached its initial boiling temperature of 140 ℃. (Azeko et al. 2016a). The plastics were then melted in the kerosene until they completely dissolved and formed a viscous liquid. The polymer's long chains were broken down upon heating at its melting temperature. The viscous liquid was rapidly quenched/ cooled in a block of ice at a temperature of between -6 ℃ and -8 ℃. After it was rapidly cooled and squeezed to remove traces of kerosene, the slurry was washed severally with ethanol and acetone and squeezed to further remove traces of kerosene. The powder particles were dried in the sun for 24 hours and the plastic pellets obtained in different sizes by sieving.

3.2 Composite Processing by Volume fraction

During the preparation of the cement mortar/composite, two different types of samples were prepared - the one without the polyethylene labelled DM/0.00 and the one with the polyethylene labelled DM/c, where c represent the volume percentages of polyethylene (PE) that partially replaced certain percentage of sand. The volume percentages of polyethylene pellets used were 0%, 5%, 10%, 15%, 20%, 30% and 40%. The different percentages of PE pellets were then casted into a mould with dimensions 40 × 40 × 160 cm^3 with mix ratio was 2:1:6 as described by (Davy 2009) [2]. Mixing of concrete and compaction of the blocks was done mechanically. The prepared mortars were packed on boards for 24 hours before curing started.

3.3 Properties of Dangote 3X Cement

According to the standard organization of Nigeria, the Dangote 3X cement also known as extra life and extra yield is the latest version of cement produced by the Dangote cement company in few countries across West Africa such as Nigeria and Ghana. This cement produces a high quality with 42.5 grades. According to Oare Ojeikre, Group Chief Marketing Officer of the Dangote group, this 42.5 R grade cement coupled with the unveiling of a new product (42.5 3X), with the recent maelstrom surrounding the ban of the 32.5 grade cement because of its low grade.

Moreover, this new cement has unique mechanical properties that slightly distinguish it from other cement. For example, unlike other cement (32.5, Portland), the Dangote 3X provides extra strength and rapid drying property which makes the product the first choice for builders and contractors. Furthermore, a bag of the new Dangote 3X Cement - 42.5R variety is observed as equivalent to one and half bag of the regular cement bag.

In terms of Xtra Life, it is speculated that 42.5 is ground finer than 32.5, giving a finer finish to concrete work, adding that the mixed cement has fewer air-pockets and therefore, adheres better and has longer life. Because of its higher strength characteristics, it is believed that 42.5 grade cement gives users higher yield than 32.5 in situations where strength is not a crucial factor, for ordinary applications, cement users could mix more sand into the same quantity of 42.5 cement, thus increasing the volume and making more blocks. Its setting characteristics is said to be rapid (R) as against others that are normal (N). This 42.5R cement is has a tendency to set more rapidly than 42.5N cement. For example, if 'N' reaches a strength level of 10 MPa in two days, 'R' would reach 20 MPa in the sametime.

3.4 Mechanical Testing

The composite samples produced with or without the polyethylene were subjected to different mechanical testing such as compressive/flexural strengths and fracture toughness. A universal mechanical testing machine (TIRAtest model 2810, Schalkau, Thuringia, Germany) was used for the compressive/flexural strength and fracture toughness measurement. The compressive/flexural tests were carried out using a displacement rate of 0.05 mm/s and a strain

rate of 0.05/s. The samples were loaded monotonically using a load cell of 25 kN until failure occurred in the samples.

The flexural strength was calculated from the expression $\sigma = \frac{3}{2}\left(\frac{LF}{BD^2}\right)$ (17)

where σ is the flexural strength (N/mm^2), L isthe loading span in mm), F is the maximum applied load (N), B is the average width of the specimen (mm), and D is the average thickness (mm) [13].

For each of the specimen, where σ_c is the critical applied stress, f (a/w) is a function of the crack length, a_c is the critical crack length and W is the width of the specimen/component, the fracture toughness is given by (Azeko et al. 2016a):

$$K_c = F(\frac{a}{w})\sigma_c\sqrt{\pi a_c} \tag{18}$$

The values of the compressive strength of the mortar were compared to that of the European standard for the requirement of compressive strength for various curing time given in the Table 2

4 Results and Discussions

The results for the compressive strengths, flexural strengths and fracture toughness values are shown in Tables (2-5) and Figures (2-5). It was realized that, the compressive strengths for the different samples increases as the number of days increases until the maximum compressive strength is attained at day 28 (Table 3). This is possible because the cement in the composite takes at least 21 days for complete hydration. The complete hydration of cement increases the bond strength in the composite and this therefore, increases the overall compressive strengths in the composite. However, the average weights of the samples decreases as the number of days increases as illustrated in Figure 2 and Table 3. The results showed that the weight of the mortar

decreased with increasing volume percentages of PE up to 40. This is associated with the dehydration of water molecules by cement, enabling cement to be completed hydrated.

The results for the trends in compressive strengths are shown in Table 3 and Figure 3. It is seen that the compressive strength for the composite without the inclusion of polyethylene was tremendously higher than the composites with different volumes of polyethylene for the first one week. However, as the number of weeks increases to the maximum weeks of four, the difference in the compressive strengths of composite without PE inclusion and composite with PE inclusions for volume percentages from 5 % up to 15 % was comparably small. This is because; at day 28, the composite with PE inclusions had completely cured and the bond strength between the cement and the PE attained its maximum strength. Since the primary idea for the inclusion of PE in the composite is to help in bridging or shielding cracks/micro-cracks, higher bond strength co- existing between the mortar and the PE leads to overall compressive strengths in the composite.

The results for the flexural strengths and fracture toughness values for the different composite composition are presented, respectively, in Figure 4 and Figure 5. It is observed that the flexural strengths for the composite with PE inclusions from 5 % up to 20 % are higher than the mortar without PE inclusions (Figure 4). The polyethylene (PE) is responsible for such behaviour in the composite. The availability of PE in the composites facilitates the shielding of micro-cracks, resulting in the overall strength of the composite. However, the composite with PE inclusions of more than 20 % recorded lower flexural strengths as compared to the cement mortar without PE. This is attributed to the fact that more PE pellets causes agglomeration and creates a weak linkage between PE-PE particles/pellets surface interactions.

The fracture toughness values of the composite increases with increasing curing time up to the maximum of 28 days (Figure 5). Also, the fracture toughness values increases with the inclusion of PE pellets in the mortar for PE volume percentages of 5 % up to 20 % and then decreases with PE volume percentages of more than 20 % and beyond. Again, the presence of many PE pellets/particles in the composites causes agglomeration and this creates a weak interface between PE-PE particles interactions, which has an overall effect in the fracture toughness of the resulting composite.

Flexural strength measures the strength of concrete due to bending/bending moments by mostly applying a three-point loading. Cementitious materials are generally known to be strong in compression but poor in tension because the bonds formed cannot be stretched beyond their limits. The materials used to make the mortar are mostly brittle and fracture upon tensile loading. Flexural Strength of Concrete is about 10 to 20 percent of compressive strength depending on the type, size and volume of coarse aggregate used (Setién et al. 2009). The polymer when deformed elastically can return to its normal shape. Therefore, the presence of the polymer in the mortar helped to improve its ductility. Furthermore, the flexural strength and fracture toughness increased up to 20% of the polymer before it started to decrease. This is also because the high tensile strength of the polymer in Table 6 contributed to the increase in the flexural strength and fracture toughness of the mortar.

The results for the reliability analysis of the different volume percentages of PE-mortar composites are illustrated in Figures 6 and 7. It is clearly shown that the PE-mortar composites with PE volume percentages of 20 % had the highest survival probability (Figure 6). The composite with this volume percentage can withstand crack up to 7 mm, with a survival probability of 0.6. At this probability, the composite is still strong enough to carry the required load on it. Also, this composite with PE volume percentage of 20 % can survive up to a crack extension of 16 mm, before final failure occurs at exactly crack propagation of 18 mm (Figures 6 and 7). Composites with PE volume percentages of 10 % and 15 % performed fairly well as far as survival and failure of the composite is concerned as illustrated in Figures 6 and 7.

5 Conclusion

This research presented a mechanistic approach of how to recycled LDPE waste into useful materials for building applications in tropical countries. This mechanism allows us to minimize environmental degradation and also its hazardous impacts (land pollution, health risks, etc.). According to this research, the use of such waste polyethylene materials in mortar helped to lower the weight of the material by ~8 % at

5 vol. % PE; ~12 % at 10 vol. % PE, and ~29 % at 40 vol. %. This means that these different decreased percentages at various increased in the PE can be used for different applications for the manufacturing of slabs, designer column, beam, parapets, etc.

Additionally, the presence of the PE in the mortar decreased the compressive strength by 8.2 at 5 vol. % PE, 12 % at 10 vol. % PE, 15 % at 15 vol. % PE, and 48 % at 40 vol. % PE due to inadequate bonding between the cement paste and the PE. However, 5 %, 10 %, 15 % and 20 % met the maximum compressive strength requirement for concrete/mortar after 28 days. As the objective of the work was concerned, the flexural strengths, fracture toughness of the mortar increased as the volume percentage of PE increased up to values of 20 vol. %. This implies that instances where the materials needed to be strong and tough, these different percentages could help designers to make the right choice(s).

It is clearly shown that the PE-mortar composites with PE volume percentages of 20 % had the highest survival probability (Figure 6). The composite with this volume percentage can withstand crack up to 7 mm, with a survival probability of 0.6. At this probability, the composite is still strong enough to carry the required load on it. Also, this composite with PE volume percentage of 20 % can survive up to a crack extension of 16 mm, before final failure occurs at exactly crack propagation of 18 mm (Figures 6 and 7). Composites with PE volume percentages

of 10 % and 15 % performed fairly well as far as survival and failure of the composite is concerned as illustrated in Figures 6 and 7.

Data Availability Statement

The data for this research will be made available upon request.

Acknowledgement

The authors are grateful to Tamale Technical University and the University of Ghana for their financial support

References

Azeko, S. T., Arthur, E. K., Danyuo, Y., & Babagana, M. (2018). Mechanical and physical properties of laterite bricks reinforced with reprocessed polyethylene waste for building applications. Journal of Materials in Civil Engineering, 30(4), 04018039.

Azeko, S. T., Mustapha, K., Annan, E., Odusanya, O. S., & Soboyejo, W. O. (2016a). Recycling of polyethylene into strong and tough earth-based composite building materials. Journal of Materials in Civil Engineering, 28(2), 04015104.

Azeko, S. T., Mustapha, K., Annan, E., Odusanya, O. S., Soboyejo, A. B., & Soboyejo, W. O. (2016b). Statistical distributions of the strength and fracture toughness of recycled polyethylene-reinforced laterite composites. Journal of Materials in Civil Engineering, 28(3), 04015146.

Blunden H. (2016). Discourses around negative gearing of investment properties in Australia. Housing Studies, 31(3), 340-357.

Bouasker, M., Belayachi, N., Hoxha, D., & Al-Mukhtar, M. (2014). Physical characterization of natural straw fibers as aggregates for construction materials applications. Materials, 7(4), 3034-3048.

Davy B. (2009). Centenary paper: The poor and the land: Poverty, property, planning. Town Planning Review, 80(3), 227-265.

Fashina, A. A., Azeko, S. T., Asare, J., Ani, C. J., Anye, V. C., Rwenyagila, E. R., ... & Dyeris, M. A. (2017). A study on the reliability and performance of solar powered street lighting systems. Int. J. Sci. World, 7, 110-118.

Gesoğlu, M., Güneyisi, E., Khoshnaw, G., & İpek, S. (2014). Abrasion and freezing–thawing resistance of pervious concretes containing waste rubbers. Construction and Building Materials, 73, 19-24.

Michael, A. O., & Razak, A. R. (2013). The study claims arising from building collapses: case studies from Malaysia, Nigeria, Singapore and Thailand. Civil and Environmental Research, 3(11), 113-129

Mustapha, K., Annan, E., Azeko, S.T., Kana, M.G.Z. and Soboyejo, W.O. (2015). Strength and fracture toughness of earth-based natural fiber-reinforced composites. Journal of Composite Materials, p.0021998315589769.

Mustapha, K., Azeko, S. T., Annan, E., Zebaze Kana, M. G., Daniel, L., & Soboyejo, W. O. (2016). Pull-out behavior of natural fiber from earth-based matrix. Journal of Composite Materials, 50(25), 3539-3550.

Opara, P.N. (2007). Building failures and Collapses: A case study of Porthacourt, Nigeria. Journal of Technology and Education in Nigeria, 12(1), 35-39.

Setién, J., Hernández, D., & González, J. J. (2009). Characterization of ladle furnace basic slag for use as a construction material. Construction and Building Materials, 23(5), 1788-1794.

Siegel, J. A., Mirakovits, J. A., & Hudson, B. (2013). Concrete mix design, quality control and specification. CRC Press.

Soboyejo W. O. (2002). "Mechanical properties of engineered materials." Toughening mechanisms, Marcel Dekker Inc., New York, vol. 152.

Soboyejo, A.B.O. (2007). Probabilistic Methods in Engineering and Bio-systems Engineering; Probabilistic Methods in Engineering Design, access and retrieved from http://hcgl.eng.ohio-state.edu/~fabe735/.

Terzić, A., Pavlović, L., & Miličić, L. (2013). Evaluation of lignite fly ash for utilization as component in construction materials. International Journal of Coal Preparation and Utilization, 33(4), 159-180.

Tonoli, G. H. D., Joaquim, A. P., Arsène, M. A., Bilba, K., & Savastano Jr, H. (2007). Performance and durability of cement based composites reinforced with refined sisal pulp. Materials and Manufacturing Processes, 22(2), 149-156.

Yildirim, H., & Sengul, O. (2011). Modulus of elasticity of substandard and normal concrete. Construction and Building Materials, 25(4), 1645-1652.

Weibull, W. (1951) A statistical distribution function of wide applicability, Journal of applied mechanics, 293-297.

Table 1: Representation of Samples by Volume Fraction

Sample	Water(g)	Cement(kg)	Sand(kg)	Polymer(kg)
DM	225	450	1350	0
DM/0.05	225	450	1282.5	67.50
DM/0.10	225	450	1215.00	135.00
DM/0.15	225	450	1147.5	202.5
DM/0.20	225	450	1080.00	270.00
DM/0.30	225	450	945.00	405.00
DM/0.40	225	45	810.00	540.00

Note: DM/0.00=Sample with 0 % PE; DM/0.05=Sample with 5 % PE; DM/0.0=Sample with 10 % PE; DM/0.15= Sample with 15 % PE; DM/0.20=Sample with 20 % PE; DM/0.30=Sample with 30 % PE. DM/0.40=Sample with 40 % PE

Table 2: European Standard for Compressive Strength (EN97 -1)

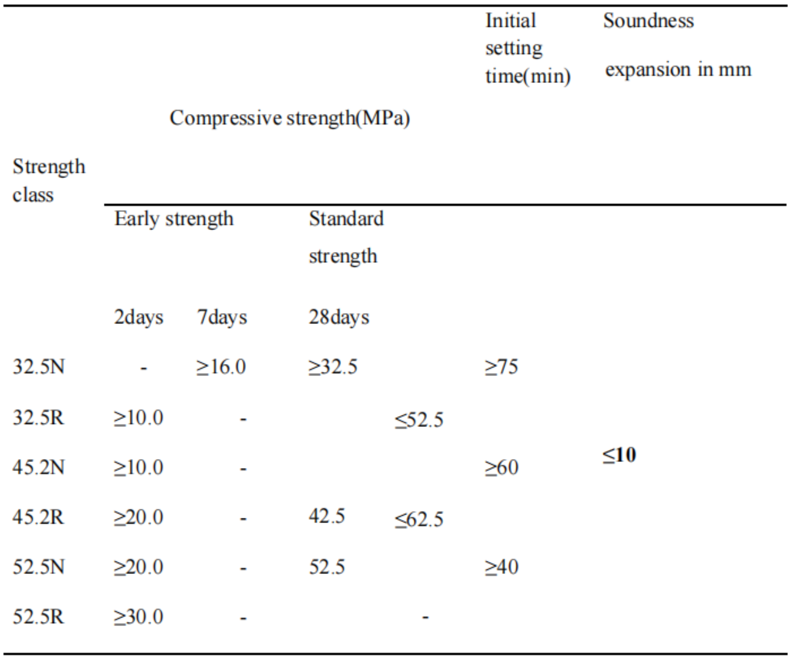

Strength class	Compressive strength(MPa)				Initial setting time(min)	Soundness expansion in mm
	Early strength		Standard strength			
	2days	7days	28days			
32.5N	-	≥16.0	≥32.5		≥75	
32.5R	≥10.0	-		≤52.5		
45.2N	≥10.0	-			≥60	**≤10**
45.2R	≥20.0	-	42.5	≤62.5		
52.5N	≥20.0	-	52.5		≥40	
52.5R	≥30.0	-		-		

Note: DM/0.00=Sample with 0 % PE; DM/0.05=Sample with 5 % PE; DM/0.0=Sample with 10 % PE; DM/0.15= Sample with 15 % PE; DM/0.20=Sample with 20 % PE; DM/0.30=Sample with 30 % PE. DM/0.40=Sample with 40 % PE

Table 3: Average Weights and Compressive Strengths for Sample Tested

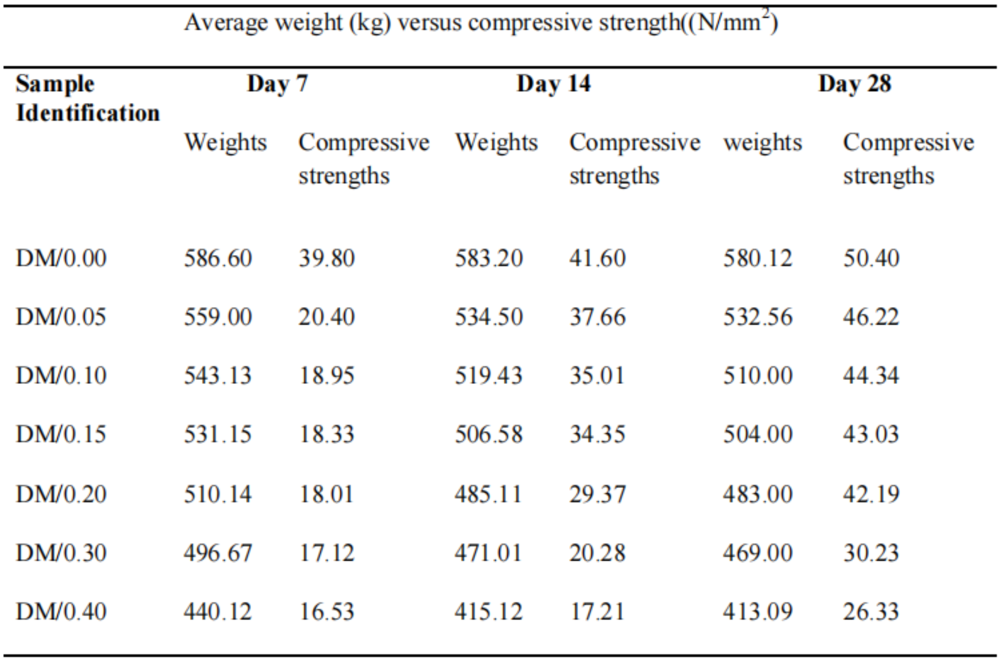

Average weight (kg) versus compressive strength((N/mm^2)

Sample Identification	**Day 7**		**Day 14**		**Day 28**	
	Weights	Compressive strengths	Weights	Compressive strengths	weights	Compressive strengths
DM/0.00	586.60	39.80	583.20	41.60	580.12	50.40
DM/0.05	559.00	20.40	534.50	37.66	532.56	46.22
DM/0.10	543.13	18.95	519.43	35.01	510.00	44.34
DM/0.15	531.15	18.33	506.58	34.35	504.00	43.03
DM/0.20	510.14	18.01	485.11	29.37	483.00	42.19
DM/0.30	496.67	17.12	471.01	20.28	469.00	30.23
DM/0.40	440.12	16.53	415.12	17.21	413.09	26.33

Note: DM/0.00=Sample with 0 % PE; DM/0.05=Sample with 5 % PE; DM/0.0=Sample with 10 % PE; DM/0.15= Sample with 15 % PE; DM/0.20=Sample with 20 % PE; DM/0.30=Sample with 30 % PE. DM/0.40=Sample with 40 % PE

Table 4: Values of Maximum Compressive Load at Fracture

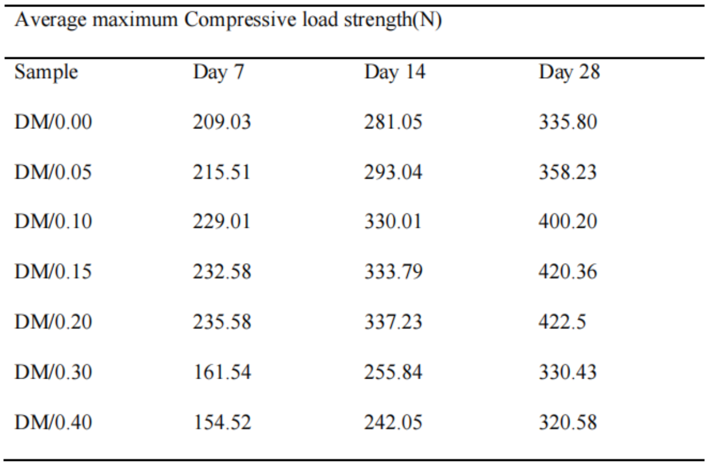

Average maximum Compressive load strength(N)

Sample	Day 7	Day 14	Day 28
DM/0.00	209.03	281.05	335.80
DM/0.05	215.51	293.04	358.23
DM/0.10	229.01	330.01	400.20
DM/0.15	232.58	333.79	420.36
DM/0.20	235.58	337.23	422.5
DM/0.30	161.54	255.84	330.43
DM/0.40	154.52	242.05	320.58

Note: DM/0.00=Sample with 0 % PE; DM/0.05=Sample with 5 % PE; DM/0.0=Sample with 10 % PE; DM/0.15= Sample with 15 % PE; DM/0.20=Sample with 20 % PE; DM/0.30=Sample with 30 % PE. DM/0.40=Sample with 40 % PE

Table 5: Average Flexural Strengths and Fracture Toughness Values

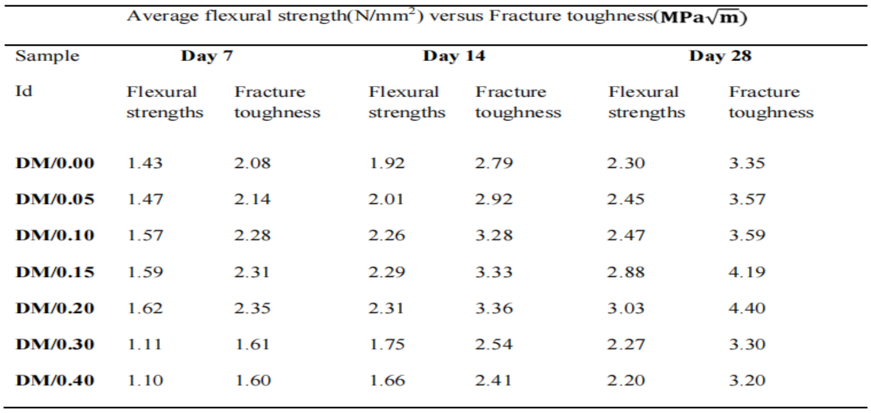

Average flexural strength(N/mm^2) versus Fracture toughness(**MPa$\sqrt{m}$**)

Sample	**Day 7**		**Day 14**		**Day 28**	
Id	Flexural strengths	Fracture toughness	Flexural strengths	Fracture toughness	Flexural strengths	Fracture toughness
DM/0.00	1.43	2.08	1.92	2.79	2.30	3.35
DM/0.05	1.47	2.14	2.01	2.92	2.45	3.57
DM/0.10	1.57	2.28	2.26	3.28	2.47	3.59
DM/0.15	1.59	2.31	2.29	3.33	2.88	4.19
DM/0.20	1.62	2.35	2.31	3.36	3.03	4.40
DM/0.30	1.11	1.61	1.75	2.54	2.27	3.30
DM/0.40	1.10	1.60	1.66	2.41	2.20	3.20

Note: DM/0.00=Sample with 0 % PE; DM/0.05=Sample with 5 % PE; DM/0.0=Sample with 10 % PE; DM/0.15= Sample with 15 % PE; DM/0.20=Sample with 20 % PE; DM/0.30=Sample with 30 % PE. DM/0.40=Sample with 40 % PE

Table 6: Major Properties of Low Density Polyethylene

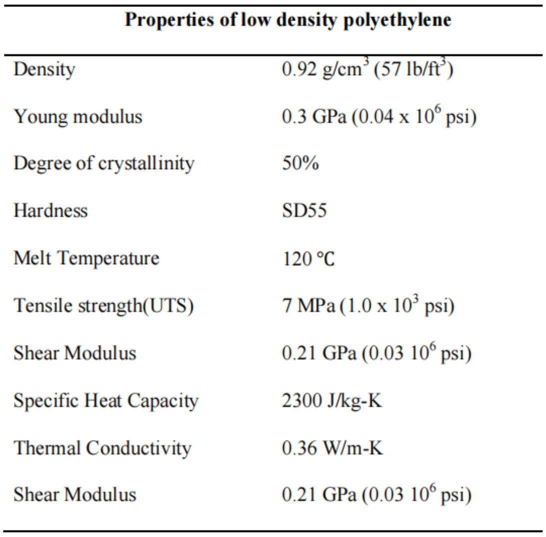

Properties of low density polyethylene	
Density	0.92 g/cm^3 (57 lb/ft^3)
Young modulus	0.3 GPa (0.04 x 10^6 psi)
Degree of crystallinity	50%
Hardness	SD55
Melt Temperature	120 ℃
Tensile strength(UTS)	7 MPa (1.0 x 10^3 psi)
Shear Modulus	0.21 GPa (0.03 10^6 psi)
Specific Heat Capacity	2300 J/kg-K
Thermal Conductivity	0.36 W/m-K
Shear Modulus	0.21 GPa (0.03 10^6 psi)

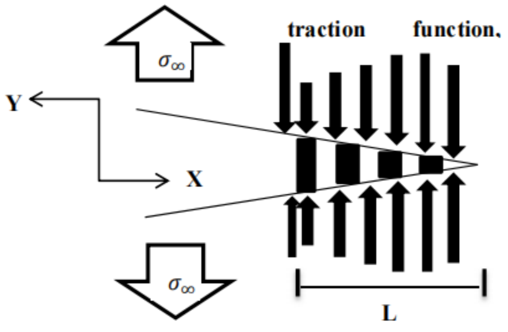

Figure 1: Schematic representation of a large-scale bridging model (Adapted from Azeko et al., 2015)

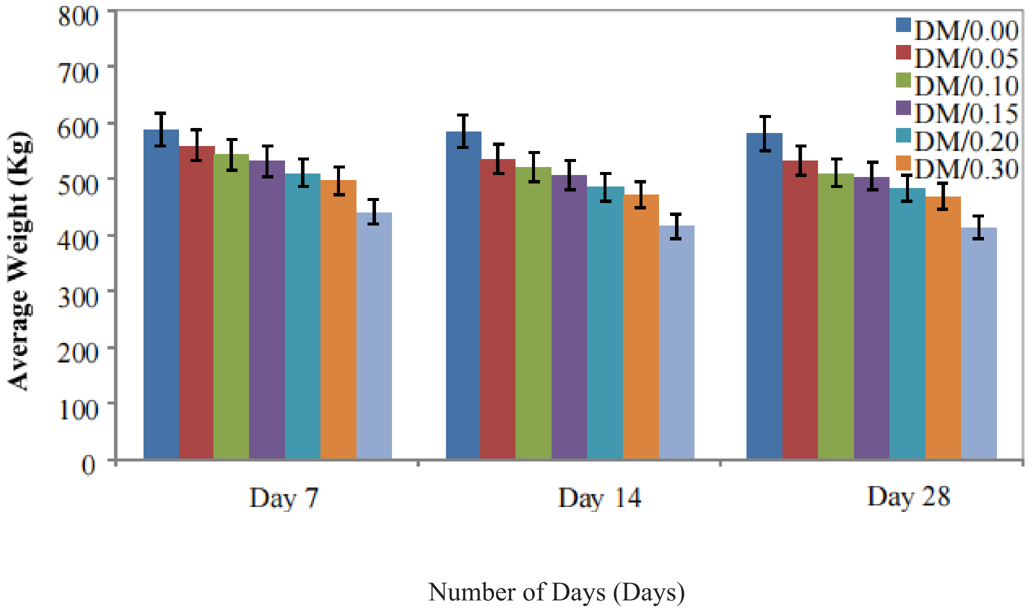

Figure 2: Graph Showing Change in Weight of Samples Note: DM/0.00=Sample with 0 % PE; DM/0.05=Sample with 5 % PE; DM/0.0=Sample with 10 % PE; DM/0.15= Sample with 15 % PE; DM/0.20=Sample with 20 %PE; DM/0.30=Sample with 30 % PE. DM/0.40=Sample with 40 % PE

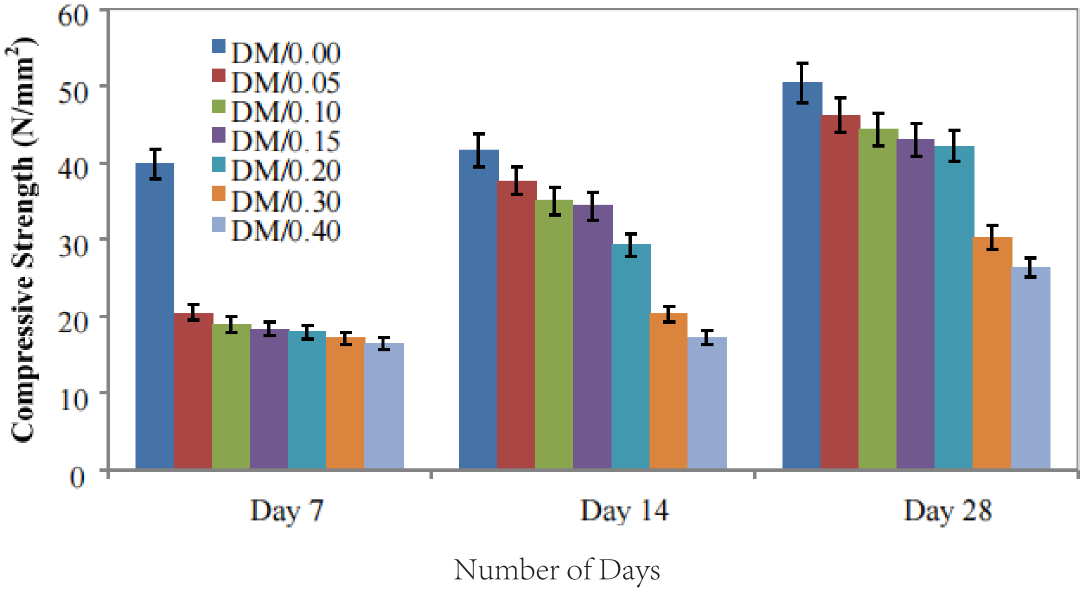

Figure 3: Trend in Compressive Strengths for Different Composite Composition Note: DM/0.00=Sample with 0 % PE; DM/0.05=Sample with 5 % PE; DM/0.0=Sample with 10 % PE; DM/0.15= Sample with 15 % PE; DM/0.20=Sample with 20 % PE; DM/0.30=Sample with 30 % PE. DM/0.40=Sample with 40 % PE

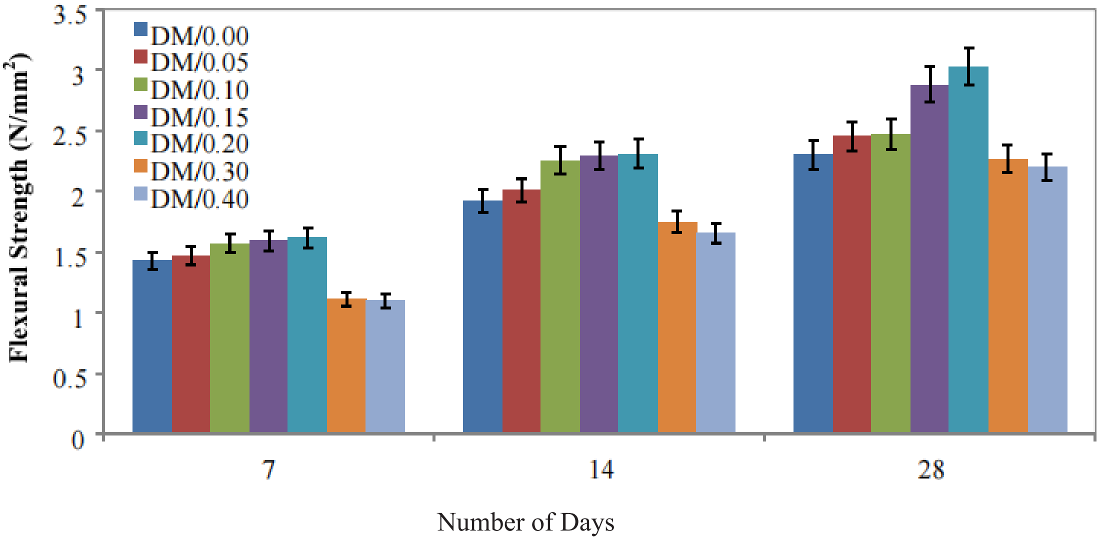

Figure 4: Flexural Strength of Composite Note: DM/0.00=Sample with 0 % PE; DM/0.05=Sample with 5 % PE; DM/0.0=Sample with 10 % PE; DM/0.15= Sample with 15 % PE; DM/0.20=Sample with 20 % PE; DM/0.30=Sample with 30 % PE. DM/0.40=Sample with 40 % PE

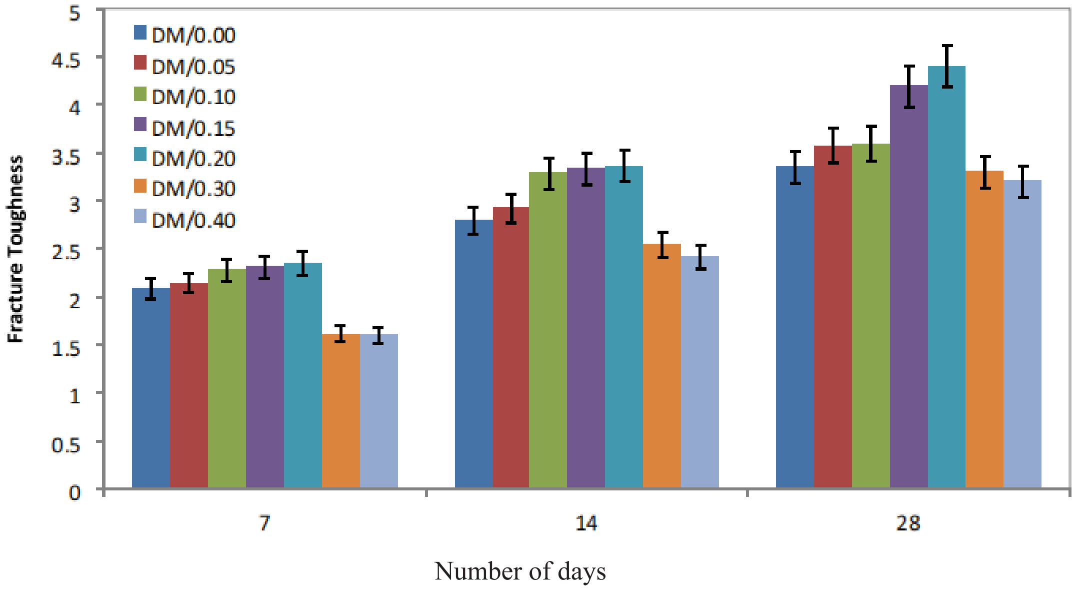

Figure 5: Trend of Fracture Toughness Note: DM/0.00=Sample with 0 % PE; DM/0.05=Sample with 5 % PE; DM/0.0=Sample with 10 % PE; DM/0.15= Sample with 15 % PE; DM/0.20=Sample with 20 % PE; DM/0.30=Sample with 30 % PE. DM/0.40=Sample with 40 % PE

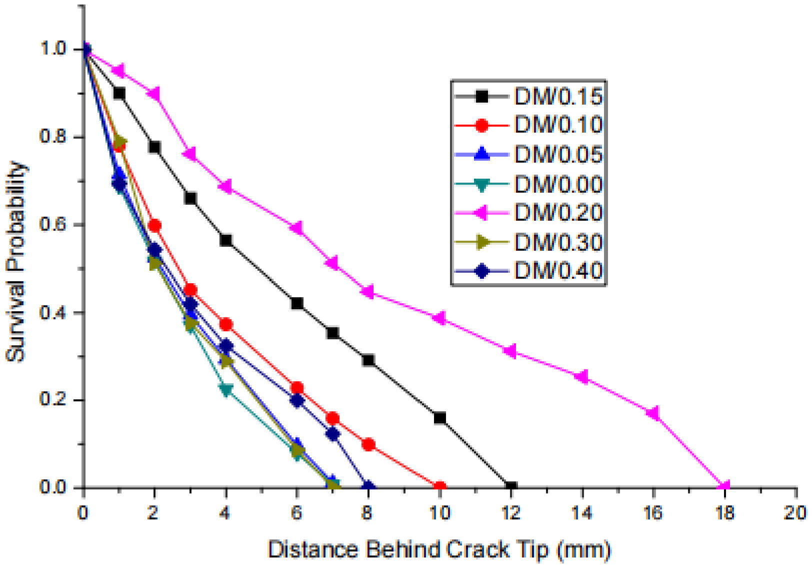

Figure 6: Survival Probability of Cement Mortar at Different Volume Percentages of PE

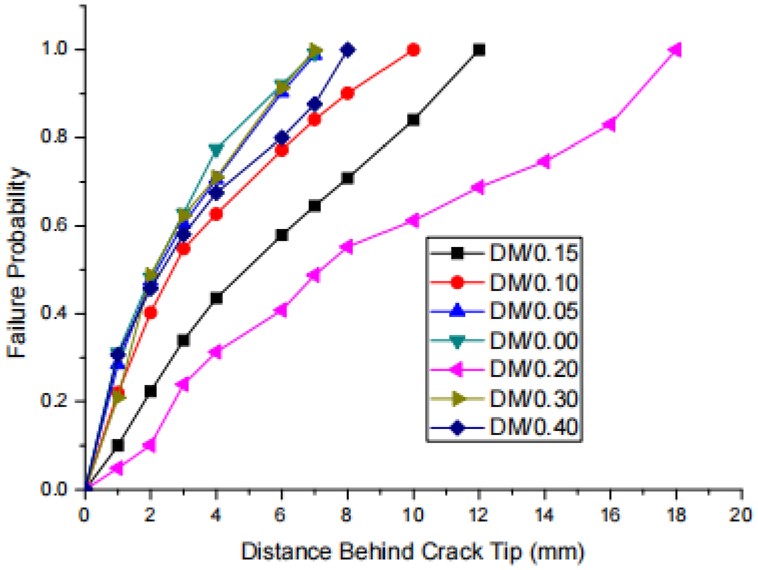

Figure 7: Failure Probability of Cement Mortar at Different Volume Percentages of PE

Note: DM/0.00=Sample with 0 % PE; DM/0.05=Sample with 5 % PE; DM/0.0=Sample with 10 % PE; DM/0.15= Sample with 15 % PE; DM/0.20=Sample with 20 % PE; DM/0.30=Sample with 30 % PE. DM/0.40=Sample with 40 % PE

Prediction Of 28 Days Compressive Strength of High Slag Concrete by Establishing Accelerated Oven Curing Regimes for Rapid Quality Control

Sudin Mohan[1,*], Mohammad Ajma[2], Michal P. Drewniok[3]
[1] Qatar Beton LLC, Doha, Qatar
[2] Doha Technical Laboratories, Mesaieed, Qatar
[3] School of Civil Engineering, University of Leeds, Leeds, UK
***Corresponding author,E-mail: sudin.m@hotmail.com**

Abstract

High Slag Concrete (HSC) offers substantial benefits in terms of durability and reduced carbon footprint, but its late strength gain delays accurate 28-day strength prediction from early strength. This study aims to develop accelerated oven curing regimes to predict 28-day compressive strength of HSC accurately. The research focuses on the fundamental question of whether the application of accelerated curing at specific temperatures would help estimate High Slag Concrete's long-term strength. To achieve this, a series of concrete specimens were subjected to accelerated oven curing at 50°C and 70°C. The compressive strength development was observed and correlated with standard curing conditions. Additionally, the hydration kinetics of the cementitious paste under these elevated temperatures were examined by using the Isothermal calorimetry method. This research will produce a predictive model correlating accelerated curing data with 28-day strength. The findings ofthis study will provide a reliable method for estimating the strength of High Slag Concrete at an early age, enabling more efficient construction planning.

Keywords: Calcium Silicate Hydrate Gel (C-S-H). Calcium Hydroxide (Ca $(OH)_2$). Calcium Alumina (Aft). Monosulphur Calcium Sulphoaluminate Hydrate (AFm). Delayed Ettringite Formation (DEF)

1. Introduction

There was a time when Portland cement (OPC) was considered the sole binding material in concrete. The Portland cement exhibits higher carbon emissions in traditional concrete and it became a persistent challenge before engineers and architects, therefore the concrete technologists , researchers, contractors etc. were looking for alternative materials to replace Portland cement and addition without losing the properties of cement. Supplementary cementitious materials in concrete like Pulverized Fly Ash (PFA), Ground Granulated Blast Furnace Slag (GGBFS), Silica Fume (SF), etc. were introduced and widely used from the mid of 20th Century in the construction industry for a variety of reasons including cost-effectiveness, enhanced durability properties, and its lower carbon dioxide emissions.

GGBFS is a by-product of iron production in blast furnaces and is similar to cement which has hydraulic properties(1). Compared to OPC, GGBFS has lower embodied carbon, approx. 1/10 compared to of 79.6 Kg CO_2e/tonne (2). Concrete with cement as a binder, is a fundamental building material used globally in the construction industry, therefore replacing cement with GGBFS is considered to be one of the strategies to decarbonise cement and concrete. It is possible to reach higher replacement rate (36%-80% (3)) at the same time improving ability to resist aggressive agents from penetrating into concrete(4).

In the precast industry, it is extremely difficult to achieve very early age strength especially within 24 hours from pouring for a high GGBFS concrete mix (5). The mold turnover is the main profit factor for precast concrete industry; therefore, it is mandatory to facilitate accelerated curing method in order to achieve the desired compressive strength for de-shuttering and lifting the precast elements. The higher the curing temperature, the faster the heat of hydration of the concrete (6), which is sufficient enough to produce a significant increase in the early age strength of slag cement concrete (7).

Compressive strength is one of the most critical mechanical properties that determine the load-carrying capacity and durability of concrete (8,9) . The strength of concrete is assessed based on 28 days results. The reason to consider the 28 days compressive strength as a parameter is based on the maturity of the concrete. The strength development of concrete depends on both time and temperature. The concrete strength is a function of the summation of product of time and temperature. This is called maturity of concrete.

$$\textbf{Maturity} = \Sigma\ \textbf{(time x temperature)}$$

The temperature is taken from an origin lying between -12 and -10°C because hydration of the concrete stops when the temperature of the concrete reaches above -12°C. However, -11°C is usually taken as a datum line for calculating maturity. The curing temperature of concrete specimen is 20°C±2 (10). For instance, A fully matured concrete cured at 18oC for 28 days will be 19,488oC h, however in standard calculations, the maturity of the fully cured concrete is taken as 19,800oC h, this discrepancy should be attributed to the datum value used for the calculation. Hence, compressive strength at 28 days is considered in the industry as a standard to determine the mechanical property of the concrete (11). As a rapid quality control procedure Its crucial for concrete Quality Control Engineer, to predict desired strength at early age. According to the maturity model using OPC, cube strength results should achieve 46% of characteristic compressive strength in 3 days and 70% in 7 days (12). This assures that the cube will achieve desired compressive strength in 28 days. Whereas in the case of mixes with higher percentage of GGBFS etc., the slower the early strength gain compared to OPC due to reduced availability of CaO in (5). Nevertheless, slag cements exhibit more strength development at later stages(13). The reduced availability of CaO in GGBFS is a key factor for slowing down the hydration process(5) By increasing the temperature during the curing time, we can increase the early age strength, so with increasing the GGBFS content and decreasing the embodied carbon, we might achieve satisfactory early age strength. Nevertheless, there are no models predicting long term strength for concretes with high GGBFS exposed to high temperature curing. Knowing the relationship between early age and 28 days compressive strength for concretes with high OPC replacement with GGBFS cured in high temperatures allow precast concrete producers to optimise their production with minimising associated embodied carbon.

2. Literature Review:

Mixes that contain GGBFS, particularly in low ambient temperature conditions, demand an extended period of curing in order to achieve sufficient strength development (14). Regourd states that the determined activation energy for slag cements exhibits a higher value compared to the activation energy of their corresponding OPC, specifically 50 and 46 J.mol-1 respectively (15). Therefore, thermal treatment is advantageous for slag cement as it serves as an efficient source of activation energy for the hydration process of slag, thus it can be regarded as a latent cementitious material as specified above.

When GGBFS is mixed with OPC, the suspension of slag is activated by the elevated pH of the solution, which is attributed to the presence of calcium hydroxide and alkali ions in the pore solution. Both the clinker and the slag undergo reactions simultaneously, resulting in the formation of calcium silicate hydrate (C-S- H), which contributes to the development of strength. The hydration process of GGBFS generally occurs more slowly compared to Portland cement. Furthermore, during the initial stages of hydration, slag can partially function as an inert filler. This filler effect enhances the nucleation and growth of C-S-H by increasing the effective water-to-cement ratio and providing additional nucleation sites (16).

Enhancing the basicity of slag results in increased hydration of the slag over a specific time period. However, higher replacement levels result in decreased slag hydration, partly due to the reduced availability of portlandite caused by the lower cement content. For comparison, over 80% of the cement in each system had hydrated after 7 days(17).

The degree of C_3S hydration increases with the addition of slag after 1 and 3 days; however, over a longer period, it remains comparable to that without slag addition. This phenomenon is thought to result from the crystallization of calcium silicate hydrate (C-S-H) on the slag particles (Fig 1). Additionally, the reduction in calcium ion concentration in the liquid phase plays a prominent role, especially in the case of very finely ground slag.(17)

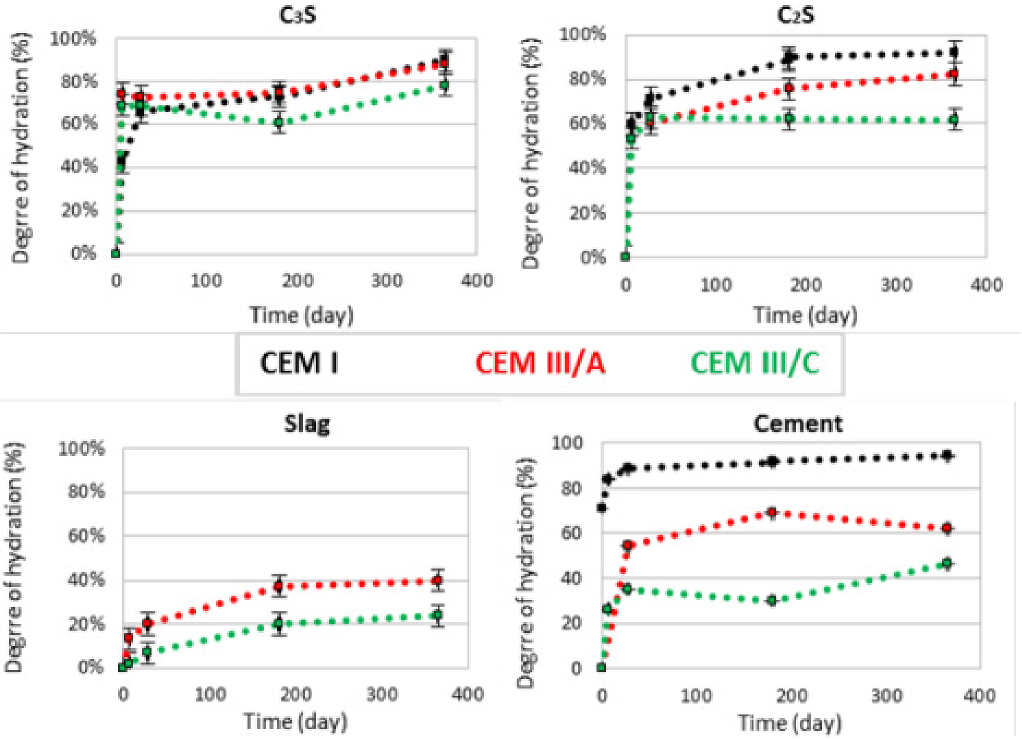

Fig 1. Example of graph showing degree of hydration (%) with respect to time of C3S, C2S, Slag and Cement for CEM I, CEM III/A, CEM III/C Cement. [Adapted from (18)]

The influence of slag on the hydration of C_3A and C_4AF is minimal, as the concentrations of Ca^{2+} , Al^{3+}, and SO_4^{2-} ions in the liquid phase are not significantly altered by the presence of slag. However, since calcium aluminate hydrates and ettringite are well-crystallized and tend to form a porous rather than a compact microstructure, it can be inferred that the hydration rate will be somewhat reduced. Conversely, some calcium hydroxide and SO_4^{2-} ions are adsorbed on the slag glass surface and incorporated into the pozzolanic reaction, which may accelerate the reaction of aluminates (18).

There is a strong correlation between the degree of slag hydration and cement strength. However, as noted by Fierens, varying strengths can be observed at the same hydration degree of different slags, indicating that other factors, such as the microstructure of hydrates and the conditions of their crystallization, also influence strength development (19).

2.1 Accelerated Curing

Accelerated curing can be conducted in various methods namely Warm Water method, Autogenous curing method, Boiling water method (20)etc. The accelerated curing techniques used for this experiment is Oven Curing method which is explained below.

Oven curing method is preferred due to its easiness in performing the accelerated test as no sophisticated setup is needed because every lab will be having a thermostatically controlled oven which fair enough for conducting accelerated test by oven curing. Moreover, it is convenient for high slag concrete [(HSC) due to its efficiency in providing actual control of curing parameters. This can be achieved by meticulously regulating temperature, a critical factor influencing the hydration of GGBFS, oven curing facilitates faster strength development without compromising the hardened concrete properties(21).

Furthermore, oven curing ensures uniform environmental conditions, minimising the variations in curing outcomes and enhancing the consistency of strength prediction. This method effectively protects concrete from external influences, ensuring unswerving quality and performance. The accelerated strength gain facilitated by oven curing is advantageous for construction projects demanding pressing timelines(22).

TNW Akroyd has conducted an exceptional study on oven curing method. He performed the oven curing 30 minutes after mixing the cubes and it was covered with base plate once the cube is placed inside the oven, temperature is brought to 85°C within 1 hour, and maintained the same temperature for a period of 5 hours. After 5 hours, the cubes are removed from the oven, stripped and allowed to cool for 30 minutes. Then it is transferred for compressive testing. Akroyd had concluded that the compressive strength test results for cubes cured normally for a period of 7 or 28 days may be predicted by accelerating the curing of the cubes and testing them 29 hours after casting (23).

2.2 Effects of Accelerated Curing on Concrete

This section examines the complex mechanisms by which accelerated curing processes influences the fundamental characteristics of concrete. Through a comprehensive analysis of these factors, this study aims to explain the potential advantages and disadvantages of accelerated curing for high-slag concrete, providing valuable insights for optimizing construction practices and achieving desired performance outcomes.

2.2.1 Microstructure

During the accelerated curing process the elevated temperature and humidity conditions contributes to shorten the induction period of cement hydration(24) . There is no change in the main products of hydration like Calcium Silicate Hydrate Gel (C-S-H), Calcium Hydroxide ($Ca(OH)_2$),Calcium Alumina (AFt), and Monosulphur Calcium Sulphoaluminate Hydrate (AFm) (25). Accelerated curing techniques change the morphology, density, atomic ratio, and chain length of C-S-H gels. Under rapid increase in curing temperature changes the bulk density of the ionic structure. The curing temperature affects the atomic distribution and changes the atomic proportions (26).

2.2.2 Delayed Ettringite Formation

Ettringite is a mineral composed of hydrous calcium aluminate sulphate, which undergoes formation within concrete during the process of curing under ambient conditions. However, in situations where concrete is exposed to high temperature curing, such as in accelerated curing or in the case of mass concrete, the excess heat produced during the process of cement hydration cannot be easily dissipated. As a result, ettringite formation can be delayed. When the concrete is set, it may lead to expansion and results in internal cracking this phenomenon is called Delayed Ettringite Formation (DEF) (27). Nevertheless, prolonged periods of elevated curing result in significantly decreased expansions, which align with documented chemical alterations that may involve the formation of ettringite following heat treatment (28).

2.2.3 Compressive Strength

This parameter requires further elaboration as it is the pivotal property being analysed in this paper. The compressive strength of concrete refers to the ratio of the maximum uniaxial load that can be sustained by the concrete at a specific rate, to the cross-sectional area of a specimen(29). Some of factors effecting the compressive strength of a concrete specimen are noted below (30).

- Porosity

The relationship between water cement ratio and porosity is a significant factor influencing the compressive strength because it affects the porosity of both the cement mortar matrix and the interfacial transition zone between the matrix and the coarse aggregate(31)

- Water Cement Ratio

Water cement ratio has direct relation on strength of concrete due to its natural behaviour of awakening of the matrix when increasing the water cement ratio due to increase in porosity of mix whereas it behaves vice versa when water cement ratio is lowered.

- Degree of Compaction

The strength of concrete is significantly affected by the increased energy applied during compaction. A portion of this strength enhancement may be attributed to unhydrated cement particles being encapsulated by thinner layers of hydrated cement. Additionally, it is plausible that high-pressure-compacted concrete derives its strength from a combination of particulate interlocking, sintering processes, and the hydration of cement.(31)

- Temperature

The influence of temperature on concrete strength depends on time – temperature history of casting and curing which means the three possibilities concrete cast and cured at same temperature, concrete cast at different temperatures but cured at a normal temperature and concrete cast at normal temperature but cured at different temperatures.(31)

It has been claimed (32) that the addition of gypsum to the mix could significantly lessen the adverse effect on strength at later ages after initial high temperature curing. Normally gypsum dosage is around 3-5% (42). This is most likely due to the gypsum interfering with the hydration phases (C_3A and C_4AF) that readily form in the presence of heat. As a result, the later hydration of slower-acting phases (C_2S and C_3S) does not disturb these phases, reducing microstructural damage and enhancing long-term strength.

Many researches have conducted research on 28 days compressive strength of concrete estimation based on early age strength. Nurse (1949) introduced steam curing, observing inconsistency due to cement composition and hydration rates. Akroyd and Smith-Gander (1956) developed the boiling method, with their modified approach (24-hour normal curing + 33-hour boiling) which closely aligned with 28-day strengths, eliminating the need for correlation graphs. Ordman and Bondre (1958) highlighted the influence of oven temperature inconsistencies, causing significant under-predictions in high-strength concrete. Neville (1957) demonstrated that smaller cubes tend to over-predict strength, particularly at high compressive levels. Emtroy (1958) presented the Cement and Concrete Association (C.C.A.) curve, providing a standardized and reliable framework for early strength predictions, especially for strengths below 28 MPa. In that Prof. Kings method of accelerated oven curing (Fig.2) is considered to be more accurate and easier for adoption (11,23). For instance, accelerated oven curing strength of 42MPa has been increased to more than 65MPa at 28 days, when it is cured under normal conditions (33). Prof. Kings cured the cubes at 93°C temperature for a period of 5 hours, and total time spend for the accelerated curing was 7 hours only. Moreover, the aforementioned research was carried out on 100% OPC mix cubes. Whereas over here we have performed the accelerated oven curing on high slag concrete and the duration of curing time is more than 24 hours.

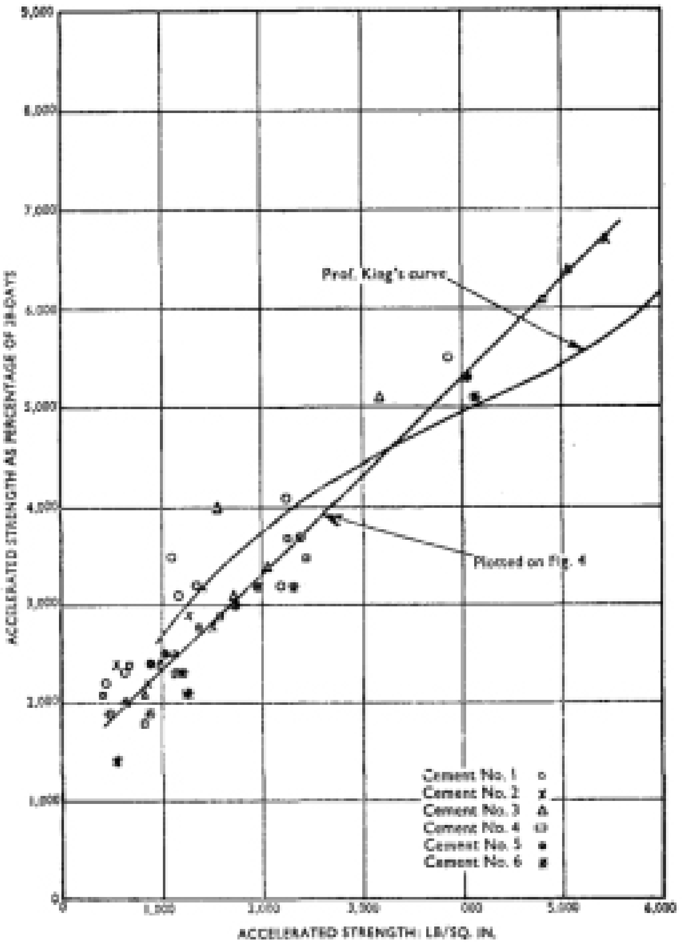

Fig.2 Prof King's prediction curve for accelerated strength as percentage of 28 days with respect to the accelerated strength [Adapted from (23)].

As previously stated, there exists a range of methods for forecasting the strength of concrete by employing diverse accelerated curing protocols. However, when it comes to concrete with a higher percentage of GGBFS composition, there is a need for further investigation into the effectiveness of accelerated curing using a thermostatically controlled drying oven. The concrete's early strength can be significantly influenced by the increased content of GGBFS. Consequently, it is necessary to thoroughly investigate the correlation between the early strength achieved through accelerated oven curing at various temperatures.

The majority of international standards pertaining to conventional accelerated curing methods have been withdrawn or replaced by other standards, resulting in a lack of a standardised protocol for conducting these tests. Ensuring the precision of forecasts derived from accelerated curing is of utmost importance in order to ascertain the dependability and feasibility of quality control protocols. This can be accomplished by juxtaposing these predictions against the concrete's real-world performance over extended periods of service life.

The potential limitations of current predictive models for estimating the 28-day compressive strength in high slag concrete under accelerated curing regimes may pertain to their accuracy and scope. There is a lack of research in the field of developing and validating reliable predictive model that consider the unique hydration characteristics of slag and its interactions with accelerated oven curing method. Knowing this relationship allows precast concrete producers to optimise their production with minimising associated embodied carbon

3. Materials and Methods

In this section we have meticulously analysed the properties of all constituent materials i.e., OPC, GGBFS, coarse aggregate and fine aggregate, admixture and water in order to assure that constituent materials conform to BS EN 206(34) . The testing of constituent materials performed based on international standard (listed in next sections) . The Quality Control testing and properties of constituent materials are explained below in detail.

3.1. Cement

Cements are classified into number of types based on their application, environment, availability, etc. The most common types of cement used in the Middle East are (I) Ordinary Portland Cement (OPC) (ii) Sulphate Resistance Cement (SRC). For this research the OPC was adopted due to its availability and consistency in Qatar, where the research took place. The chemical composition of OPC is analysed in an accredited third-party laboratory and it complies with BS EN 197-1 (35). The OPC (CEM I) used for this study is 42.5R grade. The chemical composition is given below in Table 1.

Table 1: Chemical Composition of CEM I (OPC) & GGBFS

Chemical Components	**CEM I Test** Results (%)	**BS EN 197-1 Limits** (%)	**GGBFS test** Results (%)	**BS EN 15167- 1 Limits** (%)
Magnesium Oxide (MgO)	3.2		4.9	Max.18.0
Aluminium Oxide (Al2O3)	3.6		13.5	
Silicon Dioxide (SiO2)	20.85		34.21	
Sodium Oxide (Na2O)	0.18		0.16	
Potassium Oxide (K2O)	0.4		0.4	
Calcium Oxide (CaO)	63.03		42.90	
Loss of Ignition	2.6	Max 5.0	0.9	Max 3.0
Ferric Oxide (Fe2O3)	1.8		0.9	
Insoluble Residue (IR)	0.5	Max 5.0	0.5	Max 1.5
Chlorine (Cl)	0.004	Max.0.1	0.004	Max.0.1
Sulphur Trioxide (SO3)	2.2	Max.3.5	0.5	Max.2.5
CaO/SiO2 Ratio	3.02	Min.2.0		
Titanium Oxide (TiO2)			0.19	

Table 2. Clinker Compounds of CEM I (OPC)

Clinker Compounds	CEM I Test Results (%)
Alite(C3S)	65.1
Belite(C2S)	10.7
Aluminate(C3A)	6.5
Ferrite(C4AF)	5.47

The clinker compounds were calculated as per ASTM C 150 (ref) and displayed in Table 2. Furthermore, C_3A content in this cement is 6.5% which makes this cement as moderate sulphate resistance cement even though it is marketed as OPC. The reduction of C_3A content is being pursued in Qatar as a result of the elevated levels of sulphate found in the soil.

There are three main parameters which are considered by manufacturers for assessing the quality of cement are listed below

LSF(%)= $CaO/(2.8SiO_2+1.2Al_2O_3+0.65Fe_2O_3)$

SR (%)=$SiO_2/(Al_2O_3+Fe_2O_3)$

AR(%)=$Al_2O_3/(Fe_2O_3)$

The first one is lime saturation factor (LSF) and it is determined by the ratio of lime to silica, alumina , and Iron Oxide and governs the relative proportions of C_3S and C_2S. Typical values for LSF is between 92%-99%(36) .

The second parameter is Silica Ratio (SR) which is otherwise called silica modulus. A high silica ratio means that more calcium silicates are present in the clinker and less aluminate and ferrite. Whereas the final parameter Alumina Ratio (AR) determines the potential relative proportions of aluminate and ferrite phase in the clinker.AR is usually between 1 and 3 (6). The aforementioned parameters for the cement used for this research is tabulated in Table 3.

Table 3. Cement Parameters

Lime Saturation Factor (LSF) (%)	**93**
Silica Ratio (SR) (%)	**3.86**
Alumina Ratio (AR) (%)	**2**

Winter found that in order to achieve enhanced early strength of cement, it is necessary for the values of SR (Silica Ratio) and LSF (Lime Saturation Factor) to be elevated (6). Nevertheless, there are certain disadvantages associated with the use of high LSF (lime saturation factor) and SR (silica ratio) mixes in kilns. These mixes pose significant challenges in terms of achieving the desired reactions, as they are more resistant to combustion and hard to combine. The observed phenomenon is categorized by elevated levels of carbon dioxide (CO_2) emissions, which can be associated to the augmented calcium oxide (CaO) concentration in the cement as well as an enlarged demand for fuel.

3.2 Ground Granulated Blast Furnace Slag (GGBFS)

The physical and chemical properties of GGBFS used is meticulously analysed by an accredited third-party laboratory. The measured basicity ratios for GGBFS reactivity are tabulated in Table 4.

Table 4. GGBFS Basicity Ratios

Chemical Components	**Test Results (%)**	**Limits (39) (%)**
P1= CaO/SiO_2	1.25	**>1.0**
P2= $(CaO+MgO)/SiO_2$	1.4	**>1.0**
P3= $(CaO+MgO)/(SiO_2+Al_2O_3)$	1	**1.0-1.3**
P4= $(CaO+0.56Al_2O_3+1.4MgO)/SiO_2$	1.67	**> 1.65**
P5= $CaO+MgO+Al_2O_3 / SiO_2$	1.79	**>1.0**

3.3 Mix Proportions

A single grade of mix with three different cementitious combinations is considered for this study. The primary objective of adding different GGBFS proportions was to comprehensively investigate the influence of a wide range of GGBFS additions on concrete properties. All the mixes are designed to be C50 grade. The different cementitious combination of the mixes used for this study is given below

I. C50-OPC 100%

II. C50-OPC+50%GGBFS

III. C50-OPC+70% GGBFS

The mix designs are designed in SSD (Saturated Surface Dry) condition for each cementitious combination. Mix designs are displayed in Table 5 with the yield calculations to ensure that concrete is designed for 1m³ . Herein, air content in the mix is calculated according to ACI 211.1 (37) which is 2% when the maximum aggregate size is 20mm. The yield of the mix may be slightly kept higher however in reality the air content would be less than the designed value hence yield would be around 1.02 m³.

Table 5. Mix designs

Mix Grade	**Mix** Name	**OPC** (Kg/m³)	**GGBFS** (Kg/m³)	**Water** (Kg/m³)	**10/20mm** (Kg/m³)	**4/10mm** (Kg/m³)	**0/4mm** (Kg/m³)	**HP 540 A** (Kg/m³)	**Air** (%)	**W/C** Ratio	**Theoretical Density** (Kg/m³)
C50 OPC	Mix A	410	-	144	778	382	800	4±1.5	2%	0.35	2510
C50-OPC+50% GGBFS	Mix B	210	210	147	771	385	771	4±1.5	2%	0.35	2490
C50-OPC+70% GGBFS	Mix C	129	301	151	759	380	759	4±1.5	2%	0.35	2480

The quantity of admixture in the latter mixes are subject to have a tolerance of ±1.5 kg/m³ due to ambient conditions and presence of moisture in the fine aggregate.

3.4 Mixing Procedure

The cube specimens were made in accordance with the BS EN 12390-2 (10). Consequently, the demolding of the cubes was carried out within this specific timeframe. The cubes were stored within the laboratory for a duration of 22 hours subsequent to their casting, after which they were deemed suitable for transportation to a third-party laboratory for the purpose of conducting tests. During the transportation process, gunny bags were utilized to cover the concrete cubes in order to mitigate moisture loss. The Fig 3 depicts Activity Vs Time to understand the timeline of sampling until testing.

The 27 cubes were subjected to standard water curing regime specified by BS EN 12390-2(10). The temperature of the water used for curing in the tank was adjusted to 20°C. Within the set of 27 cubes, there are 9 cubes designated for each of the three age groups: 7 days, 14 days, and 28 days respectively. These cubes are specifically allocated for the purpose of conducting compressive strength tests in accordance with BS EN 12390-3(38). The schematic flow of complete trial mix procedure is depicted below.

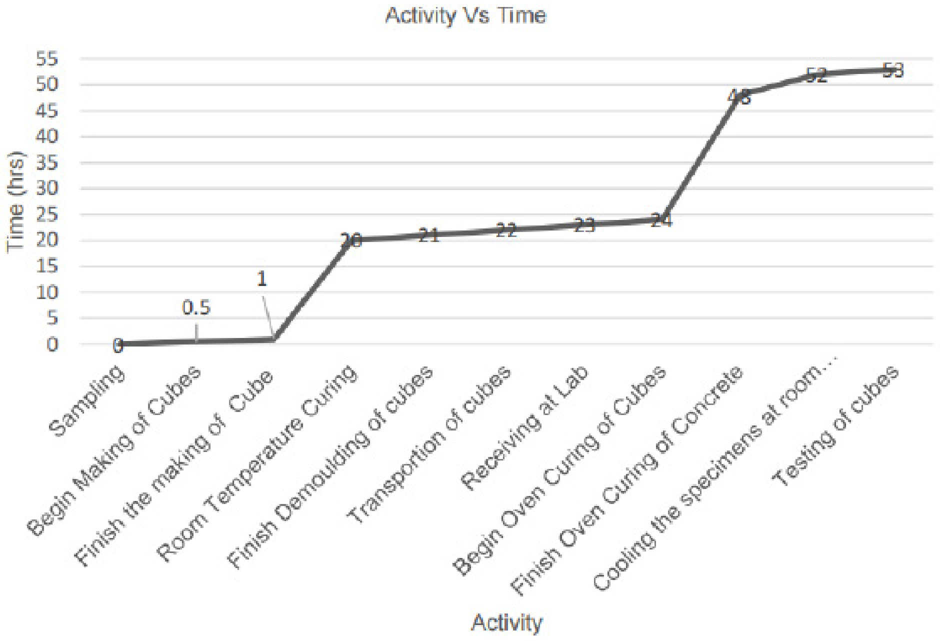

Fig.3: Schematic Flow of Trial Mix from Beginning to End

3.5 Isothermal calorimetry

The isothermal calorimetry test was conducted to study the hydration of cementitious the relationship between accelerated oven cured strength and concrete subjected to water curing at different ages has been well studied in the project. Calorimetry test was performed on accelerated oven cured mixes to monitor the hydration kinetics. The Isothermal calorimeter has to be placed in an environment with a constant temperature, typically a high-precision thermostat, in order to accurately measure heat. It is crucial to verify the accuracy of the thermostat's temperature setting. The calorimetry tests have got several applications like determination of heat of hydration, estimating the activation energy, cement admixture interactions, etc.(39).

3.6 Accelerated Oven Curing Procedure

The remaining 18 cubes were subjected to oven curing in two distinct thermostatically controlled electric drying ovens, with each oven accommodating 9 cubes. The drying oven was calibrated and can conduct a heat up to a range from 20°C to 250°C.

The ovens were set to different target temperatures, 50°C and 70°C, and the oven curing was restricted to 24±0.5 hours. In the experiment involving specimens with a target curing temperature of 50°C, the cubes were initially cured at a temperature of 30°C for a duration of 2 hours. Subsequently, the curing temperature was raised to 50°C for the remaining duration of the oven curing process. Whereas in the case of 70°C oven curing setup, the specimens were initially cured at a temperature of 30ºC for a duration of 2 hours. Subsequently, the temperature was raised to 50ºC and maintained for 1 hour. Finally, the specimens were subjected to the desired curing temperature of 70ºC for the remaining curing period, which lasted for 24±0.5 hours. The temperature time flow for 50ºC was depicted below in Fig.4. The time-temperature relation was similar to the 70ºC Curing regime except temperature progression style as stated in previously.

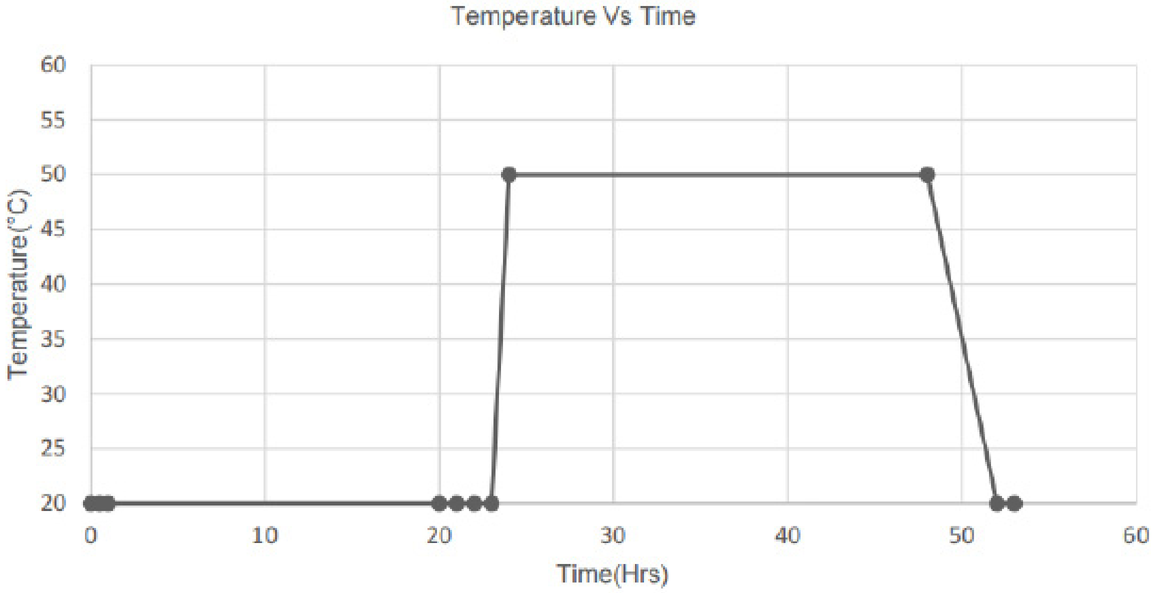

Fig.4. Time- Temperature Flow of Experiment for 50°C

Following the removal of the cubes from the oven, a designated cooling period of approximately 4 to 5 hours was observed, and the cubes were subjected to compressive testing of concrete as per BS EN 12390- 3 (38). The results of compressive strength of cubes are reported separately for cubes cured at different accelerated oven curing regimes that is 50°C and 70°C.

4. Results

The three mixes with fourth generation high range PC admixture with a solid content more than 35 is used for high workability for pumping. Initially, elevated pumping pressures are necessary to overcome the frictional resistance between the concrete and the pump tube. Once this initial resistance is mitigated and a smooth interface is established, the required pumping pressure can be reduced. A sustained decrease in pumping pressure relative to the initial value signifies satisfactory flowability characteristics of the High-Performance Concrete (HPC) mix containing the slag. Hence the target slump of 200±40 mm for better workability due to high GGBFS replacement and maximum target temperature is 35°C (40). The higher slump was proposed the cube specimens were made in accordance with the BS EN 12390-2 (10). It was observed that the concrete had achieved final setting within a period of 17-20 hours after casting. Subsequently the aforementioned curing regimes of the specimens, calorimetry and compressive strength test were conducted. The results have been elaborated below.

4.1 Conduction Calorimetry

The heat flow of the OPC + GGBFS mixes are presented below. For 50°C, the highest first peak was for OPC, lower for 50% GGBFS and the lowest 70% GGBFS cement replacement. It was noticeable, that for the highest cement replacement, the first peak was delayed. For 50% OPC replacement delay was not noticed (Fig.5).

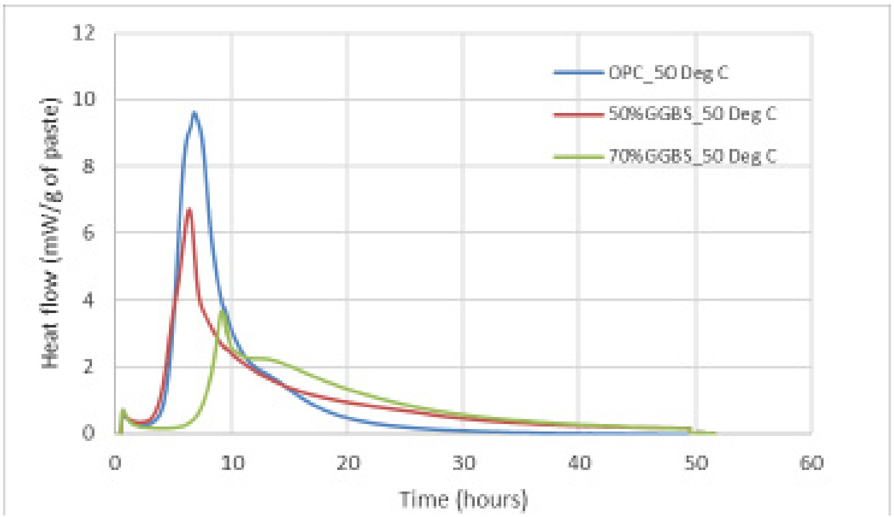

Fig.5. Calorimetry Graph at 50°C

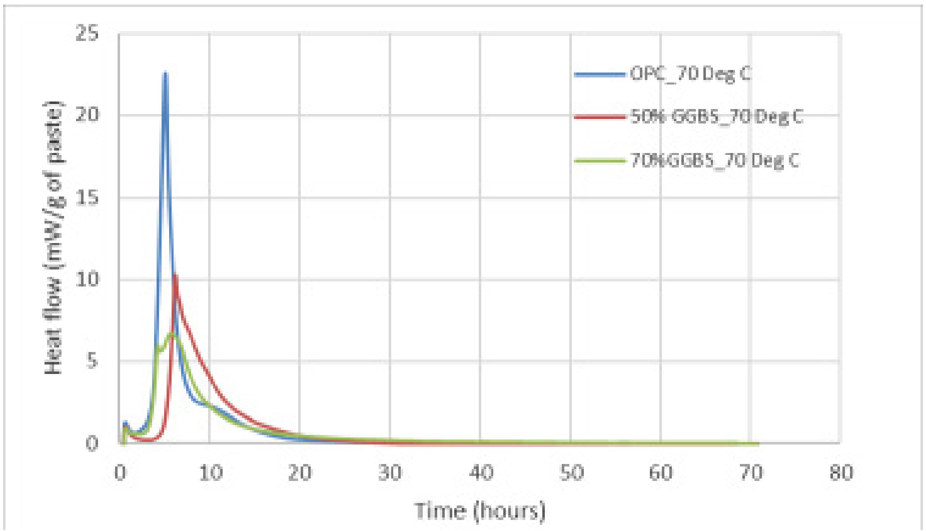

Fig.6. Calorimetry Graph at 70°C

For 70°C, the highest first peak was for OPC, lower for 50% GGBFS and the lowest 70% GGBFS cement replacement. For both 50% and 70% OPC replacement with GGBFS the first peak was slightly delayed compared to 100% OPC (Fig.6).

4.2 Compressive Strength Results

The main aim of this study was to find the relation between accelerated oven cured specimens and water cured specimens for establishing a prediction model. In order to establish a prediction model, monitoring of compressive strength of specimens were inexorable.

The compressive strength of all cube specimens which has undergone the accelerated oven curing regimes and cubes cured under water curing regime as per BS EN 12390-2 (10) were consolidated and tabulated in Annex B and their respective few test reports are attached in Annex A. The cubes cured under water curing has been tested for different ages that is 7 days,14 days and 28 days.

A comparison has been made between the compressive strength of average accelerated oven cured specimens at 23 hours from casting and 28 days water cured specimens (See Fig.7and Fig.8). This was done by creating two bar graphs to analyse the trend of strength gain for each mix at two different curing temperatures. The two bar graphs are depicted below. All mixes, no matter on OPC replacement, achieved 68MPa+-8 after 28 days of curing in ambient temperature (See Fig.7and Fig.8). The highest compressive strength for concrete cubes cured in 50°C was for the highest OPC replacement with GGBFS. Concretes with OPC replacement with GGBFS had slightly higher compressive strength compared to OPC when cured in 50°C (Fig.7). The same trend was for curing in 70°C, however there was no difference in the compressive strength for both 50 and 70% cement replacement. The difference between strength at accelerated curing and curing in ambient condition was higher for curing in 50°C and smaller for curing in 70°C, and was noticed as in Table 6.

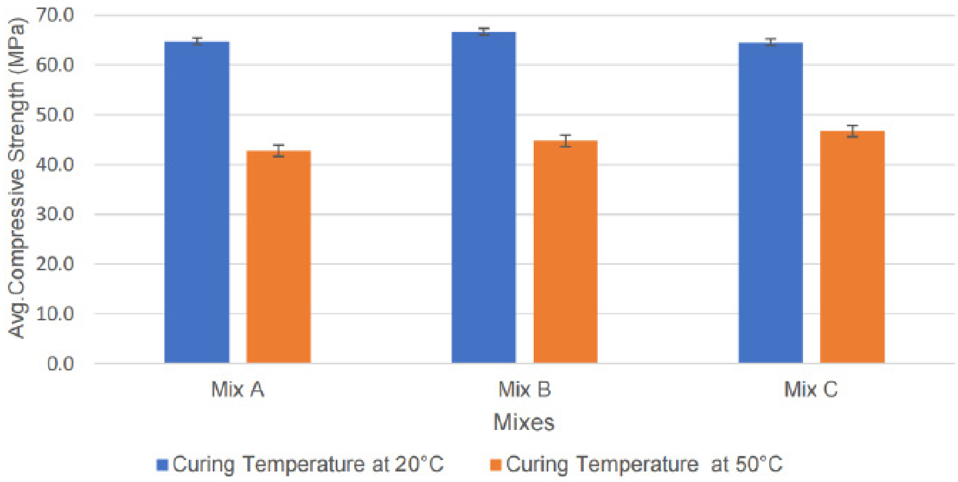

Fig.7. Comparison between 28 days Compressive Strength Vs Accelerated Oven cured Strength at 50°C

(Mix A - C50 OPC, Mix B - C50-OPC+50%GGBFS, Mix C - C50-OPC+70%GGBFS)

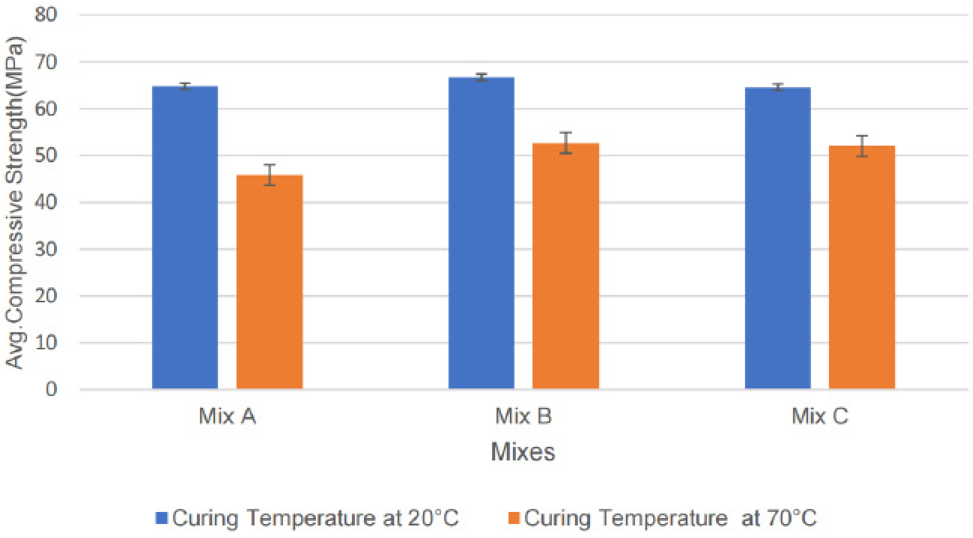

Fig.8. Comparison between 28 days Compressive Strength Vs Accelerated Oven cured Strength at 70°C

(Mix A - C50 OPC, Mix B - C50-OPC+50%GGBFS, Mix C - C50-OPC+70%GGBFS)

5.Discussion

The discussion of our results has been divided in two main sections. In the first part we emphasize on the hydration kinetics in different curing regimes is discussed based on the Isothermal Calorimetry, while the second part focuses on prediction of actual compressive strength from accelerated cured concrete strength results.

a. The Isothermal calorimetry was conducted on all mixes at two distinct temperatures namely 50 degrees and 70 degrees. It was noticed that the heat flow rate is higher in full OPC mix and as the slag content of the mix is getting higher the heat flow is also decreasing. It is clearly depicted on Figure 3 and 4. That is the main reason in mass concrete in order to reduce the core temperature of the structural element with the higher cement replacement with SCM's are recommended. The GGBFS hydrates at a slower rate than OPC which produces a lower temperature rise. (41)

b. After the initial reaction, there is an induction period which is otherwise called dormant period. The gypsum in cement is used to prevent flash set, it is usually added 3-5% with respect to seasonal changes and retarders are used to prolong the setting time. Hence the induction period of GGBFS mixes is higher than the OPC mixes. The induction period would be also higher in mixes containing retarders.

Acceleratory period where you can notice a spike indicating C3S and C2S hydration. Here comes the deceleratory period where hydration slows down, in our case its happening after 10 hours in GGBFS mix at 50 degrees However, in elevated temperature the hydration slows down for around six hours for GGBFS mixes. In the case of OPC mixes deceleration is almost similar, even though in high temperature sudden deceleration is observed. The deceleration period in cement hydration is a complex process influenced by mineral composition, temperature, and its water-cement ratio. C3S hydrates rapidly initially, leading to acceleration, but slows down as water decreases and products accumulate. C2S hydrates more slowly and contributes to later-age strength. Elevated temperature accelerates initial C3S hydration but can also decrease product solubility, leading to pronounced deceleration. Lower temperatures slow down both acceleration and deceleration. GGBFS can delay initial hydration and accelerate C2S hydration at elevated temperatures. OPC, primarily C3S and C2S, experiences rapid initial hydration followed by deceleration. Elevated temperatures can cause sudden deceleration due to increased product solubility. (42)

In the next phase, gypsum started to deplete and forms monosulphate. The Ettringite (Aft) is the one which converts to monosulphate (43) . This phase is called sulphate depletion phase.

c. The prediction graph is constructed using the compressive strength test data mentioned earlier in order to estimate the 28-day compressive strength of Mix A, B, and C. This estimation is based on the compressive strength results obtained from accelerated oven cured samples that were subjected to two different curing temperatures. The developed prediction model is established as the main goal of this study, and it is noticed that an average strength difference between accelerated oven cured specimens cured at 70 degrees and cubes tested at 28 days is around 21% for Mix B whereas for Mix C it is 19.53%. This number is quite higher in Mix A which is 35%.

The prediction graph is established and displayed below can be used for predicting the 28 days compressive strength of concrete from accelerated oven cured compressive strength results. In the prediction graph, the target strength is calculated as 59.8 MPa (44). The average Strength gain in 28 days is analysed from accelerated oven cured specimens compressive strength is tabulated in Table 6. The trend of this strength is clearly visible in Fig.9.

Table 6. Strength Gain Analysis

Mixes	% of Average Strength gain in 28 days from 50°C Cured Specimen	% of Average Strength gain in 28 days from 70°C Cured Specimen
C50-OPC	33.96	29.47
C50-OPC+50%GGBFS	32.75	21.01
C50-OPC+70% GGBFS	27.56	19.53

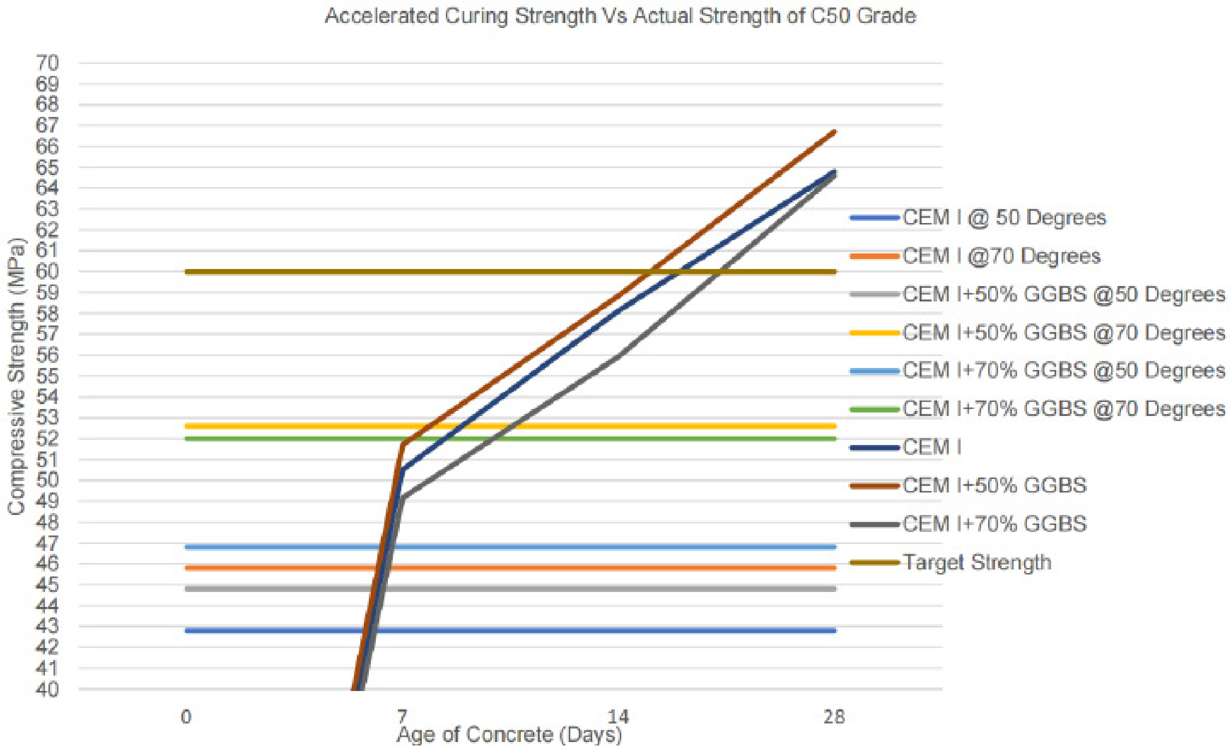

Fig.9. Compressive Strength Prediction Graph

5. Limitation of the analysis

The scope of this study was limited to a single grade with two different composition of GGBFS under 2 distinct temperatures only. In order to validate the developed model, future research should investigate the accelerated oven curing at 70°C for all grades of concrete with GGBFS compositions ranging from 35% to 70%.

6. Conclusion

This study is set out to predict the 28 days compressive strength of high slag concrete by establishing the accelerated curing regimes. The findings of this investigation are delineated in the subsequent sections.

- For analysed temperatures and levels of OPC replacement with GGBFS, prediction graph shows the evident correlation between the accelerated oven cured compressive strength and the 28 days compressive strength. By examining the accelerated strength achieved at two distinct temperatures, it is possible to anticipate the compressive strength of concrete at 28 days.
- This study has identified that curing temperature of 70 °C is closer to the 28 days compressive strength.

In other words, the percentage of average strength gained in 28 days from 70 °C cured specimens across all mix types amounts to merely 23.33%. Whereas average strength gained in 28 days from 50ºC cured specimens are 31.42%.

- The mix of OPC+70%GGBFS tends to achieve greater strength gain in 70 °C curing temperature and average strength gained in 28 days from 70ºC is comparatively lower that is 19.53%. Hence Oven curing temperature of 70 °C can be considered as regarded as the closest accelerated curing temperature for high slag concrete.
- This study observes that induction period for Mix C is higher than that of other mixes. However, in acceleratory period higher heat releasing is observed on Mix A which is 9.8mW/g for specimens cured at 50 degrees and 23.2mW/g for specimens cured at 70°C.

Future research should investigate the accelerated oven curing at 70 °C for all grades of concrete with GGBFS compositions ranging from 35% to 70%. A thorough examination of the microstructure of concrete samples cured in an oven at elevated temperatures is required to ensure that curing at high temperatures has no negative effects on the microstructure of cementitious paste.

Acknowledgements

The authors wish to acknowledge with gratitude to Mr. Imran Khan Bhati from Qatar Beton Readymix for providing with an ample quantity of concrete for the research.

Data Availability: The data collected and analysed in this study are available from the corresponding author on reasonable request.

Declarations

Conflict of interest: The authors have no competing interests to declare that are relevant to the content of this article.

References

Matthes W, Vollpracht A, Villagrán Y, Kamali-Bernard S, Hooton D, Gruyaert E, et al. Ground Granulated Blast-Furnace Slag. In 2018. p. 1–53.

Embodied CO 2 e of UK cement, additions and cementitious material [Internet]. 2019. Available from: https://www.hanson.co.uk/en/system/files_force/assets/document/53/9b/environmental- product-declaration-hanson-

BRE. Concrete in aggressive ground. Special Digest 1. 2005.

Cement_Type_Early_Age_Properties_23_Jun_11.

Korde C, Cruickshank M, West RP. Activation of slag: a comparative study of cement, lime, calcium sulfate, GGBS fineness and temperature. Magazine of Concrete Research. 2021 Jan;73(1):15–31.

Winter N. Understanding Cement. Suffolk: WHD Microanalysis Consultants Ltd.; 2009.

Zulu BA, Miyazawa S, Nito N. Properties of blast-furnace slag cement concrete subjected to accelerated curing. Journal of Infrastructures. 2019. 69 p.

Jha AK, Adhikari S, Thapa S, Kumar A, Kumar A, Mishra S. Evaluation of Factors Affecting Compressive Strength of Concrete using Machine Learning. In: 2020 Advanced Computing and Communication Technologies for High Performance Applications (ACCTHPA). IEEE; 2020. p. 70–4.

British Standards Institute. BS 8500-1:2023: Concrete. Complementary British Standard to BS EN 206: Method of specifying and guidance for the specifier. 2023.

British Standards. BS EN 12390-2-2019.

Shetty MS, Jain AK. Concrete Technology (Theory and Practice). S. Chand Publishing.; 2019.

Rhodes JA, Carreira++ DJ, Beaudoin JJ, Brauson DE, Gamble BR, Geymayer HG, et al. Prediction of Creep, Shrinkage, and Temperature Effects in Concrete Structures. 2008.

Austin SA, Robins PJ, Issaad A. Influence of curing methods on the strength and permeability of

GGBFS concrete in a simulated arid climate. cement and concrete composites. 1992. 157–167 p.

Domone P, IIston J. Construction Materials: Their Nature and Behavior. Oxon: Spon Press; 2010.

Moranville-Regourd M. Cements Made from Blastfurnace Slag In: Lea's Chemistry of Cement and Concrete. Butterworth-Heinemann; 637–678 p.

Black L. Low clinker cement as a sustainable construction material. In: Sustainability of Construction Materials. Elsevier; 2016. p. 415–57.

Whittaker M, Zajac M, Ben Haha M, Bullerjahn F, Black L. The role of the alumina content of slag, plus the presence of additional sulfate on the hydration and microstructure of Portland cement- slag blends. Cem Concr Res. 2014 Dec;66:91–101.

Stephant S, Chomat L, Nonat A, Charpentier T. Influence of the slag content on the hydration of blended cement [Internet]. 2015. Available from: https://cea.hal.science/cea-02509185

Fierens P. The hydration and properties of slags. CANMET Special Publication; 1989. 35–45 p.

International A. Standard Test Method for Making, Accelerated Curing, and Testing Concrete Compression Test Specimens [Internet]. Available from: www.astm.org,

Wedatalla AMO, Jia Y, Ahmed AAM. Curing Effects on High-Strength Concrete Properties. Advances in Civil Engineering. 2019 Jan 6;2019(1).

STANDARD SPECIFICATIONS FOR CONCRETE STRUCTURES - 2007 'Materials and Construction'. 2010.

AKROYD TNW. THE ACCELERATED CURING OF CONCRETE TEST CUBES. Proceedings of the Institution of Civil Engineers. 1961 May;19(1):1–22.

Dorn T, Blask O, Stephan D. Acceleration of cement hydration – A review of the working mechanisms, effects on setting time, and compressive strength development of accelerating admixtures. Constr Build Mater. 2022 Mar;323:126554.

Kurdowski W. Cement and Concrete Chemistry. Dordrecht: Springer Netherlands; 2014.

Wang J, Long G, Xiang Y, Dong R, Tang Z, Xiao Q, et al. Influence of rapid curing methods on concrete microstructure and properties: A review. Case Studies in Construction Materials. 2022 Dec;17.

Delayed Ettringite Formation: In situ Concrete. Vol. BRE IP11/01. British Research Establishment; 2001.

Lawrence CD. Mortar expansions due to delayed ettringite formation. Effects of curing period and temperature. Cem Concr Res. 1995 May;25(4):903–14.

Perrie B. Strength of Hardened Concrete. In: Fulton's Concrete Technology. 9th Edition. Midrand: Cement and Concrete Institute; 2009. p. 97–110.

Neville AM, Brooks JJ. Concrete Technology. Harlow Longman Publications; 1994.

Chang PK. An approach to optimizing mix design for properties of high-performance concrete. Cem Concr Res. 2004 Apr;34(4):623–9.

Hutchison RG, Chang JT, Jennings HM, Brodwin ME. Thermal acceleration of Portland cement mortars with microwave energy. Cem Concr Res. 1991 Sep;21(5):795–9.

King JWH. An accelerated test for the seven- and twenty-eight-day compressive strengths of concrete. Journal of Applied Chemistry. 1960 Jun 4;10(6):256–62.

British Standards. BS EN 206-2013+A2-2021.

British Standards. BSEN 197-1:2011.

Newman John, Choo BS. Advanced concrete technology : constituent materials. Butterworth-Heinemann; 2003.

Dixon DE, Prestrera JR, George U Burg SR, Abdun-Nur EA, Barton Leonard W Bell SG, Blas SJ, et al. Standard Practice for Selecting Proportions for Normal, Heavyweight, and Mass Concrete (ACI 211.1-91) Chairman, Subcommittee A. 1991.

British Standards. BS EN 12390-3-2019.

Scrivener K, Snellings R, Lothenbach B, editors. A Practical Guide to Microstructural Analysis of Cementitious Materials. CRC Press; 2018.

American Concrete Institute. ACI 305.1 Specification for Hot Weather Concreting [Internet]. 2014. Available from: http://concrete.org/Publications/

CIRIA C660- Early-age Thermal Crack Control in Concrete. CIA.

Qi T, Zhou W, Liu X, Wang Q, Zhang S. Predictive hydration model of Portland cement and its main minerals based on dissolution theory and water diffusion theory. Materials. 2021 Feb 1;14(3):1– 34.

Linderoth O, Wadsö L, Jansen D. Long-term cement hydration studies with isothermal calorimetry. Cem Concr Res. 2021 Mar;141:106344.

Guide to evaluation of strength test results of concrete. American Concrete Institute; 2011. 16 p.

Capture CO_2 as an admixture to improve engineering performance of ultra-high performance concrete

Yi Han [1], Runsheng Lin [1,2], Xiao-Yong Wang [1,2,*]

[1] Department of Integrated Energy and Infra System, Kangwon National University,Chuncheon-Si, 24341, South Korea

[2] Department of Architectural Engineering, Kangwon National University, Chuncheon-Si, 24341, South Korea

*** Corresponding author, E-mail address: wxbrave@kangwon.ac.kr**

Abstract

Ultra-high-performance concrete (UHPC) exhibits high compressive strength and good durability. However, owing to the dense microstructure of UHPC, carbonation curing cannot be performed to capture and sequester carbon dioxide (CO_2). In this study, CO_2 was added to UHPC indirectly. Gaseous CO_2 was first converted into solid calcium carbonate ($CaCO_3$) using calcium hydroxide, and the converted $CaCO_3$ was then added to UHPC at 2, 4, and 6 wt.% based on the cementitious material. The performance and sustainability of UHPC with indirect CO_2 addition were investigated through macroscopic and microscopic experiments. The experimental results showed that the method used did not negatively affect the performance of UHPC. Compared with the control group, the early strength, ultrasonic velocity, and resistivity of UHPC containing solid CO_2 improved to varying degrees. Microscopic experiments, such as heat of hydration and thermogravimetric analysis (TGA), demonstrated that adding captured CO_2 accelerated the hydration rate of the paste. Finally, the CO_2 emissions were normalized according to the compressive strength and resistivity at 28 days. The results indicated that the CO_2 emissions per unit compressive strength and unit resistivity of UHPC with CO_2 were lower than those of the control group.

Keywords: Ultra-high-performance concrete; Microstructure; CO_2 absorption.

1. Introduction

Ultra-high-performance concrete (UHPC) has a low water to cement ratio and a denser microstructure than that ordinary concrete. Therefore, its compressive strength and durability are better than that of ordinary concrete [1,2]. In addition, supplementary cementitious materials (SCMs) with pozzolanic reactivity are often added to increase concrete compressive strength and durability [3] [4] [5]. The SCMs most commonly used in UHPC has silica fume, fly ash, and blast-furnace slag [6] [7].

Because SCMs are by-products produced by other industries, adding them to concrete can provide both environmental protection and economic benefits. Isaia et al. [8] investigated the physical impacts of mineral additions and the influence of pozzolan on the performance of UHPC and found that as the concentration of mineral additives in UHPC increased, the pozzolanic and physical impacts became more significant.

Ghafari et al. [9] studied the effect of adding SCMs to the self-shrinkage properties of UHPC. The results showed that the main factor affecting the property was the total porosity of the paste. In addition, studies have found that the inclusion of blast furnace slag and fly ash increased the number of pores in the paste, leading to increased autogenous shrinkage [9].

The CO2 concentration in the atmosphere has increased continuously since the 1860s [10][11][12]. Global temperatures rise owing to the continuous increase in CO2, resulting in a greenhouse effect [13][14]. The Paris Agreement was signed by 175 countries to combat the impact of climate change [10]. An increasing number of researchers are working to reduce CO2 emissions, and CO2 capture and storage technologies have emerged in the cement concrete industry [15][16][17][18][19].

Carbonation curing of cement-based materials using CO2 is one of the most commonly used methods. Carbon curing has many advantages and can improve the compressive strength and durability of concrete and prevent sulfate attack and chloride-ion penetration [20][21][22].

Based on the literature studies, the research gaps of previous works are summarized as follows: first, carbonation curing is only suitable for precast concrete components. For cast-in-place concrete components, the carbonation-curing method is no longer practical. Second, the current research on concrete carbonation curing is limited to thin concrete specimens; completely carbonizing large-volume concrete in a short time is challenging. Additionally, excessive carbon curing can destroy the main hydration product (CSH) inside the concrete, thereby reducing the strength of the concrete [23]. In addition, concretes that can be cured by carbonation have high water to cement ratios (approximately 0.5) [24] [25]. Owing to the dense microstructure of UHPC, the low porosity prevents CO2 from entering the paste interior. Therefore, UHPC cannot be carbonized and solidified.

In this study, an absorbent was used to absorb CO2 and transform gaseous CO2 into a solid. The absorbed CO2 was then added to a UHPC as an admixture. Calcium hydroxide (CH) was used to convert gaseous CO2 into solid CaCO3 (CC), which was added to UHPC at 2, 4, and 6% based on cementitious material. First, the compressive, flexural, and ultrasonic strengths and resistivity of the mortars were investigated. Second, the hydration heat of the paste was determined; its microstructure was characterized by thermogravimetric analysis (TGA), attenuated total reflectance Fourier transform infrared spectroscopy (ATR-FTIR), and X-ray diffraction (XRD). Third, the CO2 emissions per unit volume of UHPC were calculated, and normalized according to the compressive strength and resistivity at 28 days. The following points were researched and assessed based on macroscopic and microscopic experiments: (1) the effect of CC on the macroscopic properties of the mortars in the early stage was investigated based on the heat of hydration of the paste; (2) the microstructural changes of the paste in the early and late stages were studied, and the development of the strength, ultrasonic wave, and resistivity of the mortars was analyzed combined with the microscopic analysis; (3) the UHPC sustainability was analyzed based on its compressive strength and resistivity.

The novelties and significances of this study are summarized as follows: based on the transformation of gaseous CO2 into solid calcium carbonate, the proposed method can be used to produce both precast concrete and cast-in-site concrete.

Moreover, because conversed solid calcium carbonate is added into the mixture during the mixing process, the slow diffusion process of CO2 from the environment to the inside of the specimen is avoided, and the proposed method is valid for high-strength concrete with low porosity. Moreover, the life cycle analysis process considers the CO2 emission from reactants of solid calcium carbonate production.

Although abundant works have been done about blended concrete containing calcium carbonate, to the best knowledge of authors, the transformation of gaseous CO2 into solid calcium carbonate and its utilization in UHPC has not been done.

2. Experimental

2.1 Raw materials

The CH used to prepare CC was purchased from Daejung Chemical Co., Ltd. Commercially available 100% CO2 was used in this study. CC was prepared according to the method described by Qin et al. [26]. First, CH was dissolved in deionized water to obtain a CH solution. Second, CO2 was fed into the CH solution at a rate of 20 L/min until the pH of the suspension reached approximately 7, and the solute of the suspension in the container was nano-CaCO3. Third, a centrifuge was used to separate the nano-CaCO3 suspension from liquid and solid. The collected CaCO3 was dried at 200 °C for 24 h to evaporate the water. Finally, the dried CaCO3 was ground into powder using an agate mortar. Gaseous CO2 transformation into solid CaCO3 was realized through CaCO3 preparation. The prepared CaCO3 was submicron. Unlike nanomaterials, submicron CaCO3 cannot cause excessive loss of fluidity, which is convenient for engineering applications.

The microstructure of the prepared CC powders was characterized by ATR-FTIR and ultrahigh-resolution scanning electron microscopy (UHR-SEM), as shown in Figure 1. Figure 1 shows the ATR-FTIR spectrum of the CC. A pronounced CC absorption peak was found; however, the presence of CH was not detected. The CC was cubic with an average side length of approximately 300 nm, as shown in the SEM image in Figure 1b.

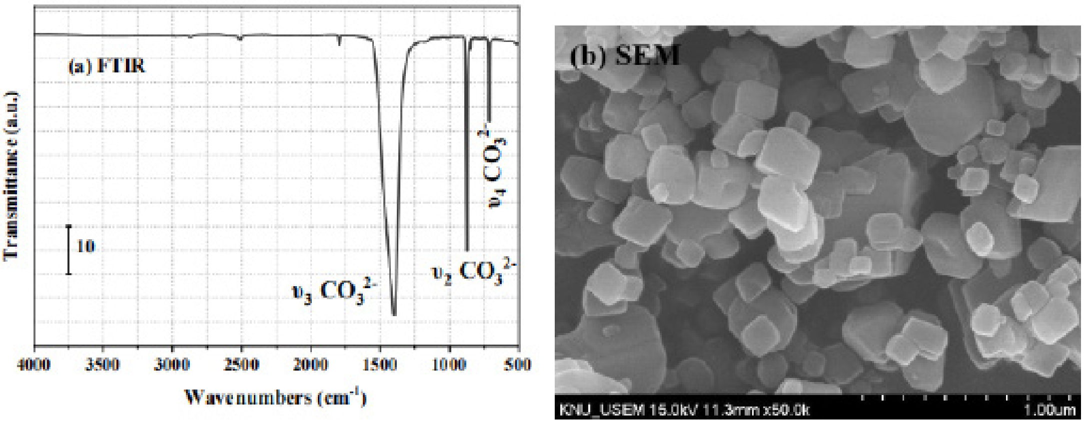

Figure 1. (a) FTIR spectra and (b) SEM of the CaCO3 powder.

The Portland cement (OPC) used in this study was a Korean Sungshin portland cement, conforming to the Korean standard KS L 5201. The silica fume (SF) was purchased from the Korean company Boram Chemical. Table 1 shows the chemical compositions of OPC, CC, and SF from X-ray fluorescence measurements. Figure 2 shows the cumulative particle size distribution curves. The median particle sizes (d50) of OPC, CC, and SF was 17.3, 2.99, and 1.23 µm, respectively.

Table 1. Chemical compositions (wt.%) of cement (OPC), silica fume (SF), and CaCO3(CC).

	OPC	SF	CC
SiO2	20.70	96.00	-
Al2O3	5.09	-	-
Fe2O3	2.56	0.39	-
CaO	63.52	0.32	55.17
MgO	2.14	1.18	-
TiO2	0.26	-	-
SO3	2.45	0.26	-
P2O5	0.19	0.17	-
K2O	0.90	0.76	-
MnO	0.07	-	-
ZnO	0.05	0.16	-
LOI[1]	2.05	0.78	44.80

[1] Loss on ignition.

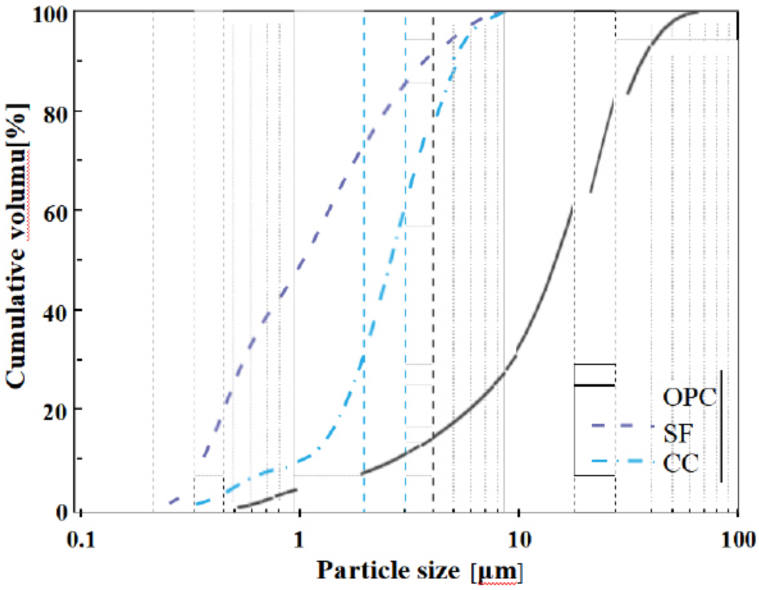

Figure 2. Cumulative volume of cement (POC), silica fume (SF), and CaCO3 (CC).

2.2 Mix proportions

The paste and mortar samples prepared for this study are listed in Table 2. Pure paste was used for the hydration heat and microscopic characterization experiments. Mortar was used for macro tests, such as strength and non-destructive testing. The water-binder ratio (w/b) of both the paste and mortar samples was 0.2, the value widely used to prepare UHPC. The binder-mortar ratio (b/s) was 1. The mixture without CC was used as the control (CC0). The prepared CC was added at 2, 4, and 6% of the cementitious material; the cement and silica fume contents were simultaneously reduced in proportion. In addition, the amount of superplasticizer (SP) was the same for all the mix ratios (2 %).

Table 2. Experimental mix proportions based on the binder (wt.%).

NO.	OPC	SF	CC	Water	SP	Sand
CC0	85	15	0	20	2	100
CC2	83.3	14.7	2	20	2	100
CC4	81.6	14.4	4	20	2	100
CC6	79.9	14.1	6	20	2	100

2.3 Test methods

Before the mortar and paste were mixed, the CC and water required for the experiment were first added to the container, mixed, and dispersed using ultrasonication waves. After the dispersion was complete, the mix was poured into the dry-mixed cement and silica fume. Finally, the mixture was mechanically stirred.

2.3.1 Heat of hydration

A TAM Air isothermal calorimeter was used to measure the hydration heat release rate at 20 °C for 72 hours. After the paste was mixed, 5 g of the paste was weighed into an ampoule bottle and immediately placed in the TAM Air isothermal calorimeter. Because the specific heat capacity of glass is similar to that of cement, glass was used as the specific heat capacity control material during the tests [27].

2.3.2 Mechanical properties

The compressive strength tests were performed according to the ASTM C349 standard [28]. The size of the cube mold used in the test was 50 × 50 × 50 mm3, and the test was conducted at curing ages of 3, 7, and 28 days. According to the ASTM C78 standard [29], a 40 × 40 × 160 mm3 cuboid sample is used to conduct a three- point bending test when the curing age is 28 days. Three samples were tested for each mixing ratio, and the results were averaged.

2.3.3 Non-destructive testing

Ultrasonic testing was performed using a portable non-destructive digital indicator produced by the Swiss company Proceq. Longitudinal P-wave velocity tests were performed according to ASTM C597 [30] at curing ages of 3, 7, and 28 days. The test sample was a cuboid with dimensions of 40 × 40 × 160 mm3. Three samples were tested for each mixing ratio, and the results were averaged.

The resistivity test was performed using a portable nondestructive resistivity tester (Proceq, Switzerland). According to the AASHTO T 358 standard [31], resistivity experiments were conducted on cylinders with dimensions of Φ100 × 200 mm at curing ages of 3, 7, and 28 days. Each sample was tested thrice, and the results were averaged.

2.3.4 Microscopic characterization

Test samples for thermogravimetric analysis (TGA), XRD, and FTIR were dehydrated by solvent exchange [32]. Manual grinding with a small amount of isopropyl alcohol was performed in an agate mortar to prevent carbonation during the grinding. After grinding, the mixture was poured into a beaker, and isopropanol that is approximately four times the mass of the mixture was added; the mixture was allowed to stand for 10 min. The suspension was then filtered and washed four times alternately with isopropanol and diethyl ether. Finally, the filtered powder was dried in a vacuum drying oven. The tests were performed the following day.

TGA was performed using an SDT Q600 TA Instruments instrument with a ramp rate of 10 °C/min to measure mass loss in the range 20–1000 °C. Anitrogen purge at a gas flow rate of 100 mL/min was used during the test. XRD was performed using an X'Pert-pro MPD diffractometer from 5 to 70° (2θ) in steps of 0.013° . ATR-FTIR experiments were performed using a Frontier spectrometer (PerkinElmer) in the scan range 500–4000 cm-1, scanning each sample 16 times.

3. Results and discussion

3.1 Heat of hydration

Figures 3a and 3b show the 7-day heats of hydration and cumulative hydration, respectively. The start time of the acceleration period occurred earlier in the pastes with CC addition than in the control group (CC0), as seen in the enlarged view in Figure 3a. The time to peak of heat flow gradually moved forward with an increased CC addition. As also seen in the enlarged view in Figure 3b, the cumulative heat release of the mixed paste with added CC was higher than that of the control group (CC0) in the early stage of hydration (before 40 h). CC accelerated the hydration rate of the paste, which was attributed to the dilution and nucleation effects of CC [33].

Because the cement content in CC4 and CC6 pastes was lower than that in CC0, the cumulative heat release of CC0 gradually exceeded that of CC2, CC4, and CC6 at approximately 36 h. This heat release difference suggested that the physical action (filling effect) produced by CC had a significant impact only in the early stages of hydration. Figure 4 shows the normalized heat of hydration and the cumulative heat based on the cement. The heat of hydration of the mixed paste with added CC was higher than that of the control group because the filling effect (dilution effect nucleation effect) produced by CC enhanced the hydration reaction of the cement [34].

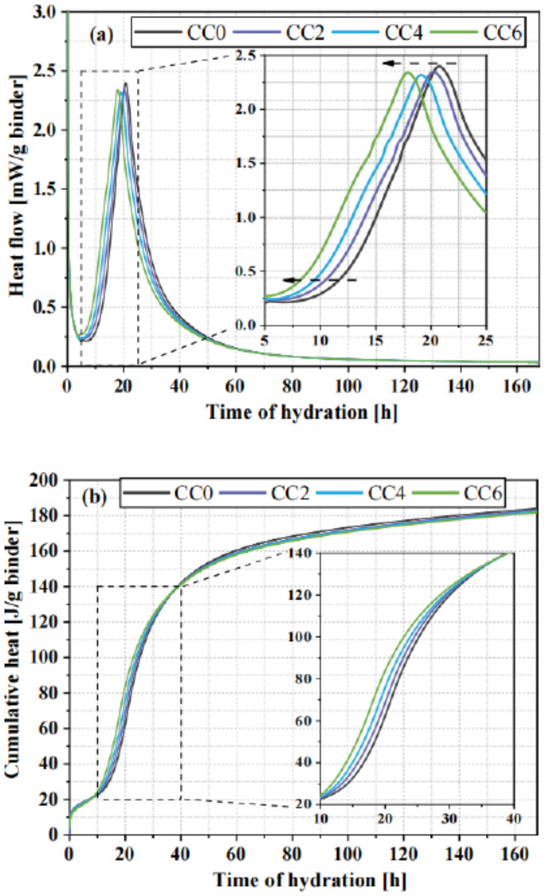

Figure 3. (a) Heat of hydration and (b) cumulative heat of pastes based on the binder.

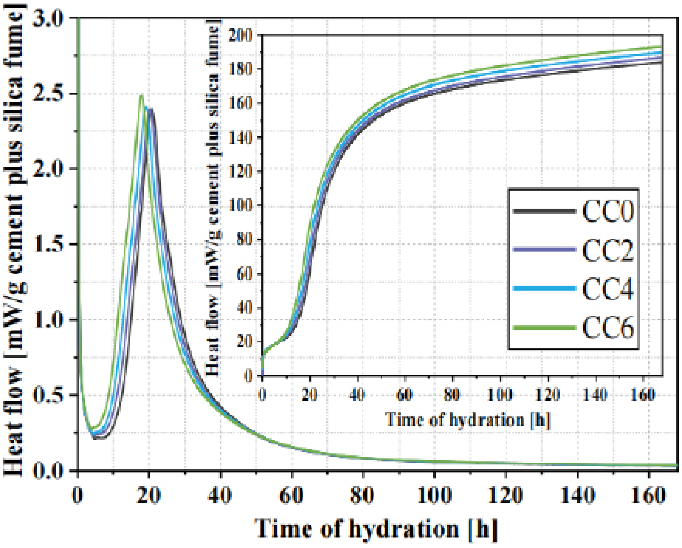

Figure 4. Normalized heat of hydration and cumulative heat based on the cement plus silica fume.

3.2 Mechanical properties

The compressive (3, 7, and 28 days) and flexural strength (28 days) test results of the mortars are shown in Figure 5a. Figure 5b shows the normalized compressive strength of the mortars with CC0 as the benchmark. From Figure 5a, the compressive strength of the mortars added with CC was higher than that of the control group CC0 when the curing age was 3 d. Adding 2 and 4% CC significantly improved the 3-day compressive strength of the mortar. The compressive strengths of CC2 and CC4 reached 71.91 and 72.71 MPa, respectively. The 3-day compressive strength of the mortars increased because of the filler and nucleation effects caused by the addition of CC [29]. The presence of CC improved particle packing and refined the internal pores of the mortar. CC provided nucleation sites for hydration products, accelerating the mortar hydration rate [35] [36]. The heat of hydration results also showed that the presence of CC accelerated the paste hydration rate. Notably, the 3-day compressive strength values of CC6 were very close to those of the control group. The physical effect produced by adding CC contributed to the development of the early compressive strength of the mortar. However, the reduction in hydration products due to the decreased cement and SF content also significantly affected the development of the compressive strength in the middle and late periods (7 days and 28 days). When the curing age reached 28 days, the compressive strength of CC2 was slightly higher than that of the control group (112.94 MPa). The compressive strengths of both CC4 and CC6 were lower than that of CC0. Similar findings have been reported previously[37] [38]. Kang et al.[39] found that the presence of LP in the paste led to capillary pores of approximately 10 nm, leading to a decreased UHPC compressive strength in the middle and late stages (28 days). With an increased curing age, the gradual weakening of the physical effect of CC may have been one of the reasons.

In addition to physical impacts, CC has chemical effects and a coupling effect with aluminum-rich SCMs [40]. However, aluminum-rich SCMs were not added in this study; thus, CC did not significantly contribute to developing the compressive strength in the middle and late stages ofthe mortar. Figure 5b further shows that when compared to the control group CC0, the normalized compressive strength percentage of the mortar supplemented with CC steadily declined with increasing curing age. With an increased CC addition, the normalized compressive strength percentage of the mortar decreased significantly.

The results for the 28-day flexural strength test of the mortar are shown in Figure 5a. The flexural strength of CC0 in the control group was the lowest at 10.12 MPa;the flexural strength of CC2 was the highest at 11.74 MPa. A correlation analysis was performed on the cumulative heat release and compressive strength for 3 and 7 days, as shown in Figure 6. An excellent linear relationship between them ($R^2 = 0.932$) was observed.

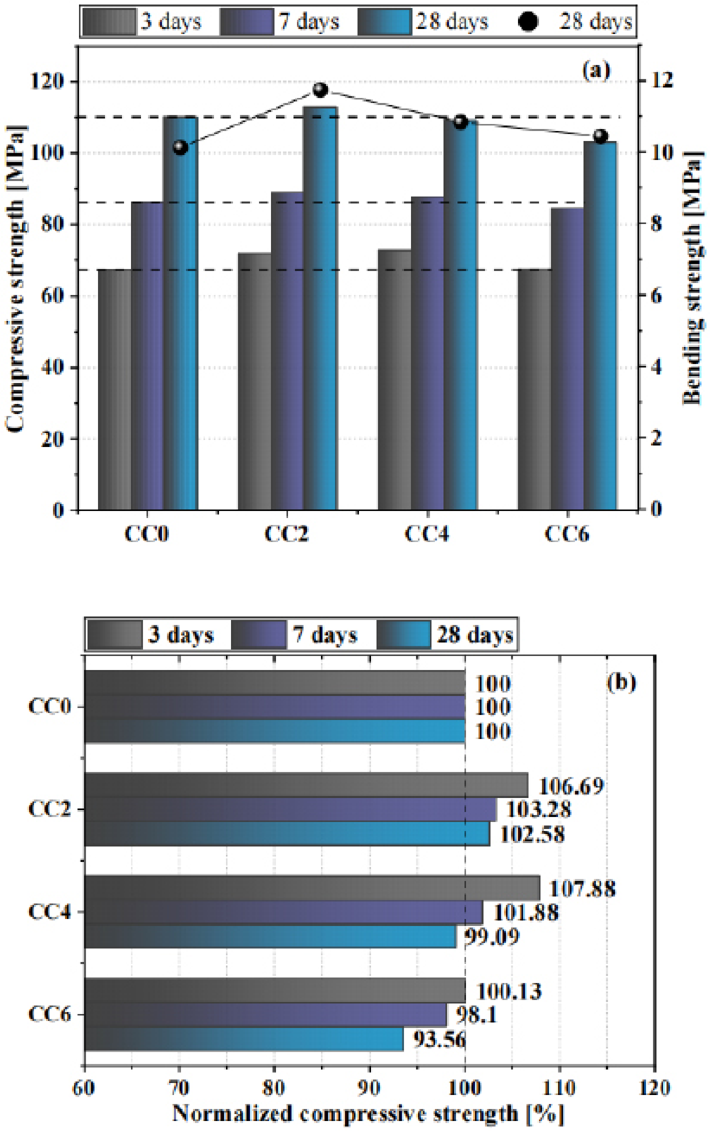

Figure 5. (a) Compressive and flexural strength; (b) normalized compressive strength of the samples.

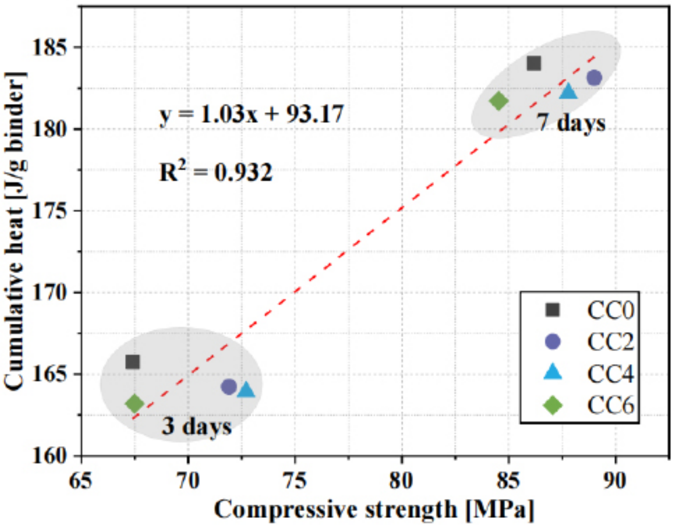

Figure 6. Compressive strength and cumulative heat relationship.

3.3 Ultrasonic pulse velocity

Figure 7 shows the ultrasonic pulse velocity (UPV) results after 3, 7, and 28 days.When the curing age was 3 days, the UPV of CC0 was 4.348 km/s, and the UPV of the mortars with added CC was higher than that of CC0. CC4 had the highest UPV (4.469 km/s). The addition of CC produced filler and dilution effects. The presence of CC improved particle packing, refined the internal pores of the mortar, and accelerated the mortar hydration rate. The resulting hydration products made the microstructure of the mortar denser [39] [41]. With an increased curing time, the UPV of the mortar also gradually increased. At 7 days, the UPV of the mortar with added CC was still higher than that of the control CC0. However, compared with the control group, the UPV of the mortars with added CC was only approximately 0.84–1.31% higher than that of CC0. When the curing age reached 28 days, the UPV of CC6 was lower than that ofCC0.

The UPV growth rate was calculated using the following formula (1):

$$Growth\ rate\ of\ UPV\,(\%) = \frac{U_T - U_{3d}}{U_{3d}} \times 100 \tag{1}$$

where UT and U_{3d} are the UPV values when the curing age is 7 or 28 days and 3 days, respectively. The results are shown in Figure 8a. With an increased CC substitution, the growth rate of UPV gradually decreased. Adding CC had a significant effect on the mortars in the early stage, accelerating the hydration rate and making the interior of the mortar dense through the hydration products produced [35]. With an increased curing time, the physical effect of CC in the early stage gradually decreased. On the contrary, the effect of decreased cement and SF content gradually became significant. In addition, a quantitative correlation analysis was performed between the growth rate of UPV and CC content, as shown in Figure 8b. An excellent linear relationship between the growth rate of UPV and CC content was observed, and the growth rate of UPV decreased with increased CC content. In addition, the coefficient of determination (0.958) between the growth rate and CC content of UPV from 3 to 28 days was higher than the coefficient of determination (0.845) between the growth rate and CC content of UPV from 3 to 7 days. The differences proved that CC had an effect on the UPV development of mortar in the early stage, with the effect gradually decreasing with increasing curing time.

Solid hydration products have a significant effect on the development of mortar UPV; the development of compressive strength is also affected by the content of the solid hydration products. Figure 9 shows the quantitative correlation analysis between the compressive strength and UPV. There was an excellent exponential relationship between compressive strength and UPV in this study (R^2 = 0.897).

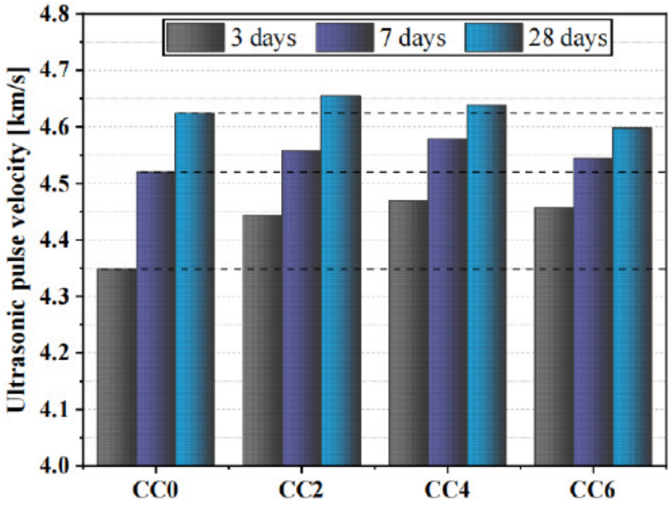

Figure 7. Ultrasonic pulse velocity results.

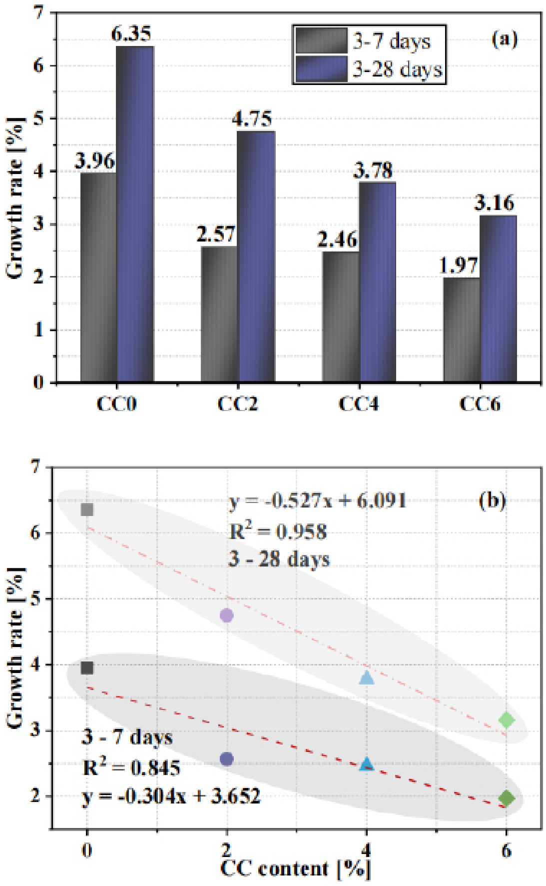

Figure 8. (a) Ultrasonic pulse velocity growth rate at 3-7 and 3-28 days; (b) the relationship between UPV growth rate and CC content.

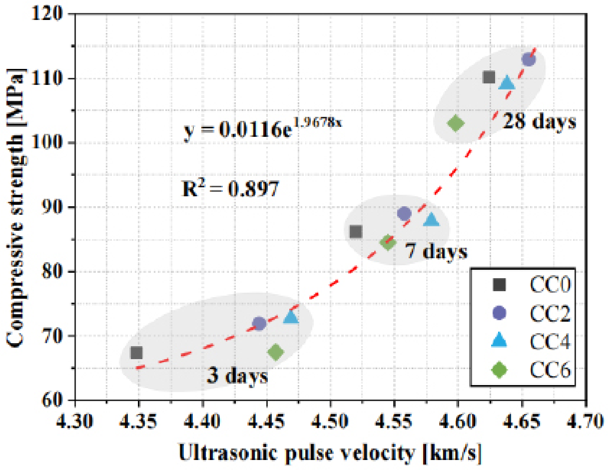

Figure 9. Relationship between ultrasonic pulse velocity and compressive strength.

3.4 Electrical resistivity

The resistivity test results at 3, 7, and 28 days in this study are shown in Figure 10a.When the curing age was 3 days, the resistivity of the mortar was between 19.5 and 26.95 kΩ·cm; the resistivity of CC0 was the smallest (19.5 kΩ·cm), and the resistivity of CC6, the most CC content, was the largest (26.95 kΩ·cm). With increased curing age, the resistivity of mortar at 28 days ranged from 389.5 to 445 kΩ·cm. Notably, the resistivity increase of all mortar samples was slight from 3 to 7 days. A significant increase in resistivity from that of 7 days curing was observed when the curing time reached 28 days. The growth rate of the resistivity was calculated using the following formula (2):

$$Growth\ rate\ of\ ER\ (\%) = \frac{R_T - R_t}{R_t} \times 100 \qquad (2)$$

where R_T is the resistivity when the curing is 7 or 28 days, and R3d is the resistivity when the curing is 3 or 7 days. The results are shown in Figure 10b. The resistivity growth rate in the middle and late periods (7-28 days) was much higher than that in the early and middle periods (3-7 days) because the pozzolanic reaction of SF produced more CSH in the middle and late stages, making the internal microstructure of the mortar denser [42]. In addition, as shown in Figure 10b, with increased CC content, both the 3–7 and 7–28 days resistivity growth rates of the mortar gradually decreased. The trend may be due to the reduced cement and SF content.

The resistivity of the CC-added mortar was normalized to that of the control group (CC0), as shown in Figure 10c. As the curing time increased, the resistivity difference between the mortars became less significant. After 3 days, the resistivity of the mortars with added CC was higher than that of CC0. The resistivity of the mortars also gradually increased with increasing CC content. The resistivity of the mortars with added CC was 21.8–38.21% higher than the control group, which was attributed to the physical action of CC (filler and dilution actions) [43]. With an increased curing time, the effect of the physical action of CC on the resistivity of the mortars gradually decreased. At 7 days, the resistivity of the mortars with added CC was 18.82–26.4% higher than that of the control CC0. When the curing age reached 28 days, the resistivity of the mortars with added CC was only 1.28–14.25% higher than that of CC0.

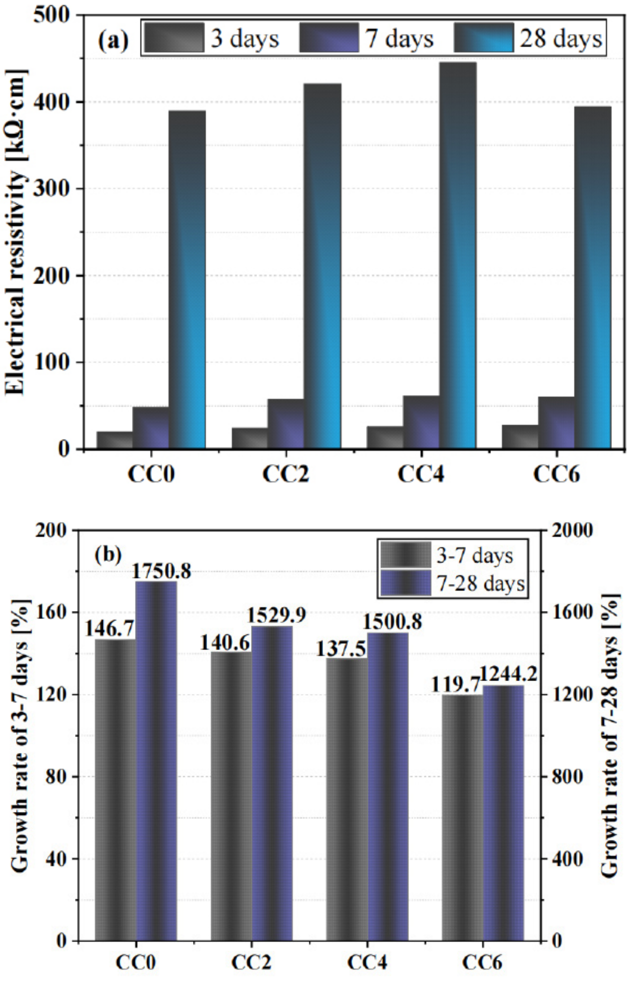

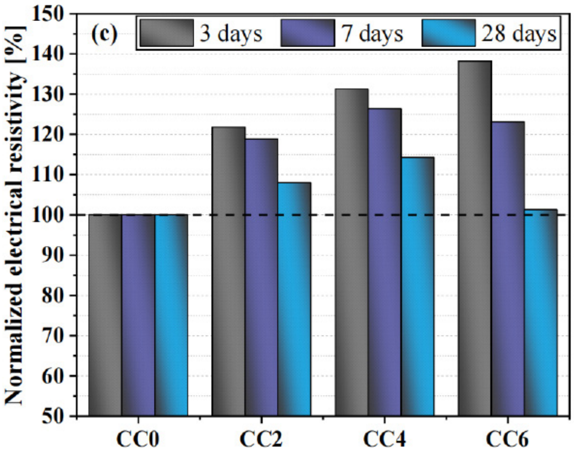

Figure 10. (a) Electrical resistivity test results; (b) electrical resistivity growth rate at 3–7 and 7–28 days; (c) electrical resistivity normalized to the resistivity of CC0.

3.5 XRD

Figures 11a and 11b show the XRD patterns measured at 3 and 28-day curing, respectively. The CH diffraction peak of the paste increased gradually with an increased amount of CC, consistent with the results of the heat of hydration experiment, in which CC accelerated the hydration rate of the paste. With an increased CC addition, the diffraction peaks of CC also increased. In addition, because the Korean cement used in this study contained 2–3% $CaCO_3$ [44], the diffraction peaks of CC was also observed in the XRD pattern of CC0. With an increased curing time, the crystalline phase in the paste changed significantly.

Compared to the XRD pattern of the paste after 3 days, the diffraction peaks (2θ = 9.1 and 15.9°) of ettringite in the paste increased significantly after 28 days. The diffraction peaks of hemicarboaluminate (Hc) and monocarboaluminate (Mc) are shown in Figure 11b. According to a previous study [45], CC was beneficial for the production of carboaluminate and ettringite, as shown in reaction (3).

$$3(3CaO.\ Al_2O_3).\ CaSO_4.12H_2O + 2CaCO_3 + 18H_2O \qquad (3)$$

$$\rightarrow (3CaO.\ Al_2O_3).\ CaCO_3.11H_2O + (3CaO.\ Al_2O_3).3CaSO_4 \cdot 32H_2O$$

Comparing Figures 11a and 11b, the intensity of the diffraction peaks caused by the C_3S and C_2S in the pastes decreased as the curing time increased. Compared with the XRD pattern of the paste after 3 days, the diffraction peaks of CH (2θ = 17 and 34°)

at 28 days were significantly reduced. The reduction may be due to some CH being consumed by the pozzolanic reaction in SF in the middle and late stages.

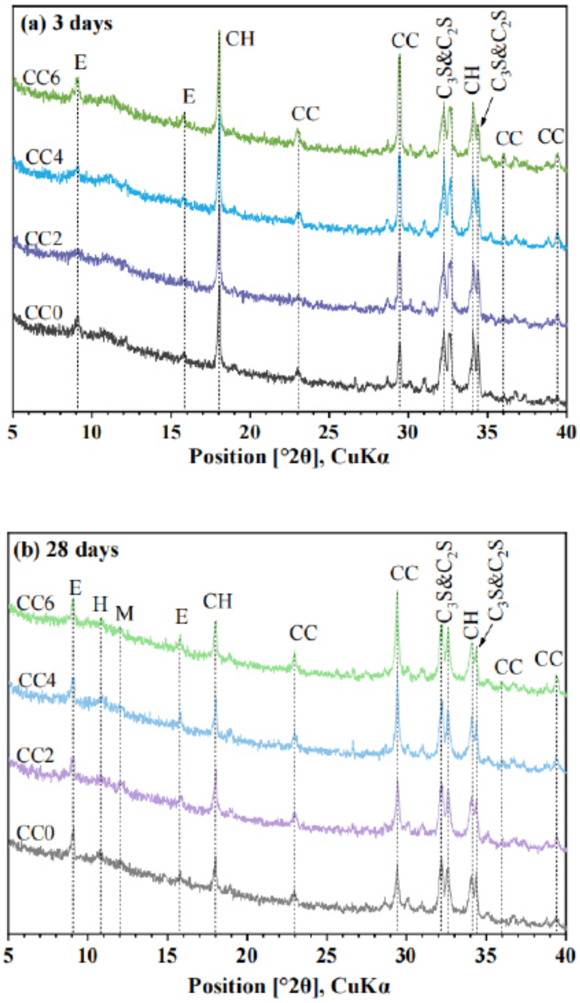

Figure 11. XRD patterns of the pastes at (a) 3 days and (b) 28 days. E = Ettringite; H = Hemicarboaluminate; M = Monocarboaluminate; CH = calcium hydroxide; CC = Calcium carbonate.

3.6 ATR-FTIR

Figures 12a and 12b show the ATR-FTIR spectra of the pastes after 3 and 28 days of curing, respectively. The absorption peak caused by the OH- (v) stretching vibration in CH appeared at 3641 cm-1 [46] [47]. The CH- absorption peak at 28 days for the paste in Figure 12b was very small compared to that in Figure 12a, consistent with the XRD results because of the pozzolanic reaction in the SF in the middle and late stages.

The broad peak at 1451 cm-1 was caused by the asymmetric stretching vibration of CO32- (v3) in CaCO3 [48]. In addition, the absorption peaks at 877 and 715 cm-1 were caused by the out-of-plane bending vibrations of CO32- (v2 and v4) and CaCO3, respectively [46] [47]. The absorption peak caused by CO32- increased with increased CC content in the paste. In addition, the absorption peaks caused by CO32- decreased with an increased curing age because part of the CC and aluminate generated Hc and Mc, which was also observed in the XRD patterns. The absorption peak at 1116 cm-1 was caused by SO42- (v3) stretching vibration [48] [49]. As shown in Figure 12a, the absorption peak of the CC-added paste was significantly larger than that of CC0. In addition, compared with that at 3 days, the SO42- absorption peak of the paste at 28 days decreased significantly with an increased curing time. The absorption peak caused by the SiO42- (v3) asymmetric stretching vibration of CSH appeared at 952 cm- 1 [46]. From Figure 12a, the absorption peak of the paste containing CC was significantly larger than that ofCC0 because the physical action early produced by the CC accelerated the hydration rate of the paste. In addition, comparing Figures 12a and 12b, it can be observed that the absorption peak at 952 cm-1 increased as the curing time increased.

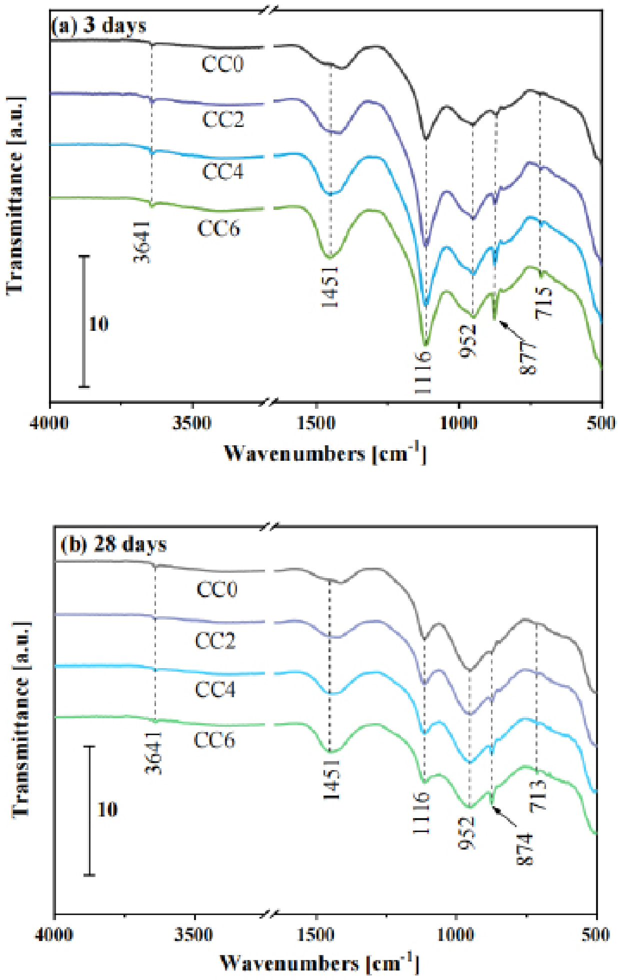

Figure 12. ATR-FTIR spectra of the pastes at (a) 3 and (b) 28 days.

3.7 TGA

Figures 13a and 13b show the results of the TG analysis of the pastes at 3 and 28 days. Three stages of weight loss was be observed: (1) hydration product (calcium silicate hydrate, AFt, and AFm) decomposition (100–200 °C)[50], (2) calcium hydroxide decomposition (400–500 °C) [50], and (3) $CaCO_3$ decomposition (600– 750 °C)[32]. During the first weight-loss stage, the hydration products formed in the paste containing CC were higher than those of the control group CC0, and the peak weight loss increased with increased CC addition, as seen in Figure 13a. In addition, in the second stage, it was found that the CH content in the paste with added CC was also higher than that of CC0, confirming that the CC had a physical effect in the early stages, which accelerated the hydration rate of the paste. When the curing time reached 28 days, the decomposition peak of the hydration products increased significantly during the first stage of weight loss. With an increased curing time, the continuous hydration of cement generated more hydration products. In addition, the pozzolanic reaction of SF consumed CH, generating a large amount of calcium silicate hydrate. In Figure 13b, the CH decomposition peak at approximately 450 °C was significantly lower than that at 3 days. In addition, the decomposition peak of the CCO paste at about 120 °C exceeded that of the paste containing CC. This was due to the reduced cement content in the CC-containing pastes. The presence of CC can accelerate the hydration rate of the paste in the early stage; however, because of the extremely low reactivity of CC, a large number of hydration products cannot be generated in the middle and later stages of hydration.

The chemically bound water content was calculated according to the method described by De Weerdt [51], as shown in Equation (4):

$$W_b = \frac{W_{40} - W_{550}}{W_{550}} \times 100\% \tag{4}$$

The results are shown in Table 3. At 3 days, the chemically bound water content in the paste increased with the CC content. Initially, CC accelerated the hydration rate of the paste; thus, the hydration products also increased. At day 28, the chemically bound water of CC0 increased significantly compared to that at day 3. With an increased curing time, the cement continued to undergo a hydration reaction, and SF also experienced a pozzolanic reaction; thus, the hydration products increased significantly. In the middle and late stages, the physical effect of the CC gradually decreased, and the influence of decreased cement content in the paste gradually increased. A quantitative correlation analysis between compressive strength and chemically bound water (Wb) was also performed, as shown in Figure 14. An excellent linear relationship was observed between them (R2 = 0.933).

Table 3. Chemically bound water content in the pastes (%).

Curing time	CC0	CC2	CC4	CC6
3 days	11.84	12.26	12.29	12.82
28 days	15.85	16.08	14.81	14.50

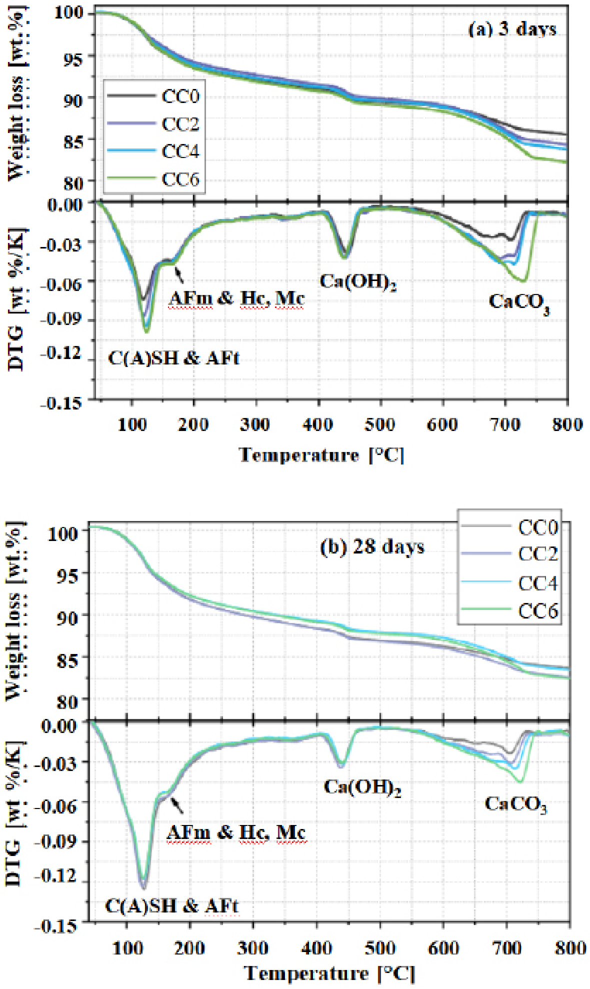

Figure 13. TGA and DTG curves for the pastes at (a) 3 and (b) 28 days.

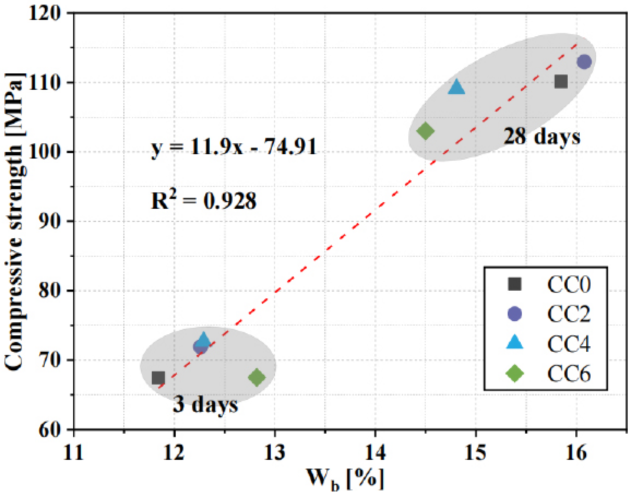

Figure 14. Relationship between Wb and compressive strength.

3.8 Sustainability

The CO2 emission for the production of calcium carbonate is determined as follows. The CO2 emission per kilogram of CH is 0.528 kgCO2/kg [52]. When CH was used to prepare CC in this study, the chemical reaction formula (5) was as follows:

$$Ca(OH)2 + CO2 \rightarrow CaCO3 + H2\ O \quad (5)$$

One kilogram of CC consumes 0.74 kg CH and 0.44 kg CO2 ; thus, the CO2 emission factor ofCC is 0.74×0.528 — 0.44= - 0.04928*kg·CO2/kg* .

CO2 emissions are currently a topic of concern, and the addition of SF and CC in concrete has a positive effect in reducing CO2 emissions. Therefore, the CO2 emission reduction capacity of UHPC was calculated. The CO2 emissions per cubic meter of concrete were calculated according to the method described by Zhang et al. [53], as shown in formulas (6) and (7):

$$\sum_{i=1}^{n} \frac{M_i}{\rho_i} = 1 \quad (6)$$

$$CO_{2/m^3} = \sum_{i=1}^{n} \left(M_i \times CO_{2(i)} \right) \quad (7)$$

where ρ_i represents the specific gravity of the raw materials; M_i is the mass of raw materials (kg/m3), as shown in Table 4; $CO_{2/\,m3}$ represents the CO_2 emissions per cubic concrete; $CO2_{(i)}$ represents the CO_2 emissions per kilogram of raw material, as shown in Table 5.

Table 4. The mass of the different components and CO2 emissions of mortars.

NO.	Mass of raw materials (kg/m^3)						CO2 emissions (kg·CO2/m^3)
	OPC	SF	CC	Water	SP	Sand	
CC0	910.57	160.69	0.00	214.25	21.43	1071.26	790.90
CC2	891.67	157.35	21.41	214.09	21.41	1070.44	773.49
CC4	872.80	154.02	42.78	213.92	21.39	1069.61	756.10
CC6	853.96	150.70	64.13	213.76	21.38	1068.79	738.74

Table 5. CO2 emission factors for raw materials[54] [55].

	OPC	SF	CC	SP	Water	Sand
CO2 emission factor (kg. CO2/kg)	0.863	0.014	-0.04928	0.0016	0.000196	0.0026

The calculation results of $CO_{2/m3}$ are shown in Table 4. The CO2 emissions decreased with the addition of CC. This is predictable because the substitution of CC reduces the use of other raw materials, and the CO2 emissions per unit of CC are negative.

The CO2 emissions of the mortars were compared with the compressive strength and resistivity (durability performance) at 28 days to better understand the long-term performance of the concrete. The CO2 emissions per unit compressive strength and resistivity were computed using Equations (7) and (8), respectively.

$$CO_{2-c} = \frac{CO_{2/m^3}}{F_{c-28}} \tag{7}$$

$$CO_{2-e} = \frac{CO_{2/m^3}}{F_{e-28}} \tag{8}$$

The calculation results of CO2-c (CO2 emission per unit compressive strength, kg·CO2/MPa) and CO2-e (CO2 emission per unit resistivity, kg·CO2/kΩ·cm) are shown in Figure 15. The CO2-c and the CO2-e of the mortar with CC were both smaller than those of CC0. The CO2-c of CC2 was the smallest at 6.85 kg·CO2/MPa. Because the addition of CC diminished the later compressive strength of the mortar, the CO2-c of CC4 was equivalent to that of CC0. Compared to the control group, the CO2-e of the mortar supplemented with the different CC additions reduced by 9.36, 16.26, and 7.88%, respectively. CC4 exhibited the lowest value at only 1.70 kg·CO2/kΩ·cm.

Based on the results, the addition of CC to the mixture had dilution and nucleation effects, accelerating the hydration reaction rate and contributing to the early compressive strength development. However, with an increased curing time, the physical effect of CC gradually decreased. Simultaneously, the effect of reducing the cement and silica fume content gradually increased (decreased hydration products).

The decrease in hydration products decreased the compressive strength and resistivity of the mixtures with high CC content when the curing age reached the middle and late stages. However, adding CC reduced the CO2 emissions of the mixture, and a high amount of CC affected the later development of the compressive strength and resistivity of the mixture. Therefore, when the compressive strength and resistivity were considered simultaneously, adding CC within 4% was the most cost-effective. It can also ensure that the mechanical properties and durability of the mixture are maintained while minimizing CO2 emissions.

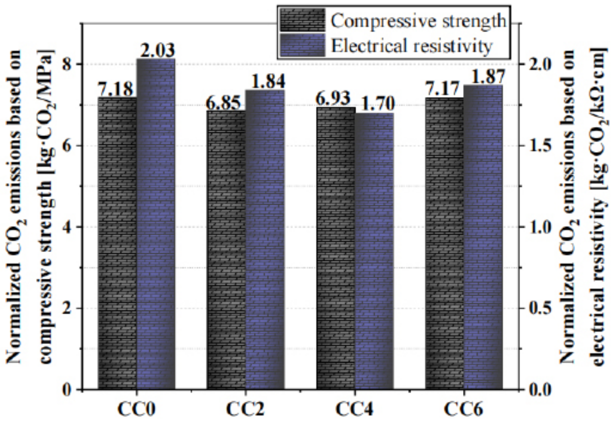

Figure 15. CO2 emissions per unit of electrical resistivity and compressive strength.

4. Conclusion

This study investigated the addition of CO2 to UHPC using an indirect addition method. Gaseous CO2 was first converted into solid CaCO3 and then added to the UHPC. The performance and sustainability of UHPC were investigated experimentally. The mortars were tested for their compressive strength, flexural strength, ultrasonic strength, and resistivity. The heat of hydration and microstructures of the pastes were also characterized. The following conclusions were drawn from the test results.

(1) The hydration heat and strength test results showed that adding CO2 converted into a solid (calcium carbonate) accelerated the early hydration rate of UHPC, contributing to improved early compressive strength. After normalizing the compressive strength based on the control group, it was found that the percentage of compressive strength of the UHPC sequestered with CO2 gradually decreased with increased curing age.

(2) UPV experiments showed that the physical effect of adding CO2 (CC) converted into a solid gradually decreased during the early stage. With an increased curing time, the UPV growth rate decreased with an increased CC content. Moreover, an excellent exponential relationship between UPV and compressive strength (R2 = 0.897) was observed.

(3) The surface resistivity tests showed that the resistivity growth rate (1244.2– 1750.8%) of UHPC in the middle and late stages (from 7 to 28 days) was much higher than that in the early and middle stages (from 3 to 7 days) (119.7–146.7%); however, the resistivity difference between the mortars became less significant as the curing time increased. Adding CC converted into a solid-state significantly affected the early resistivity. However, in the middle and late stages, cement hydration and the pozzolanic reaction of SF had a more significant impact on the resistivity of the mortar.

(4) The XRD and FTIR test results showed that the pozzolanic reaction of SF had a gradually significant effect on the paste in the middle and late stages. In addition, at 28 days, the presence of Hc and Mc was observed in the XRD pattern owing to the chemical reaction of CC with the aluminum phase in the cement.

(5) The results of the TGA experiments showed that the decomposition peak of CSH increased with an increased CC content at 3 days. This indicated that CC accelerated the hydration rate of the paste. In addition, an excellent linear relationship between chemically bound water and compressive strength (R2 = 0.933) was observed.

(6) Compared with the control group, the CO2 emissions per unit compressive strength and per unit resistivity of the mortar added with CC decreased to varying degrees, suggesting indirect capture and storage of CO2 in UHPC was feasible. In addition, when the compressive strength and resistivity were considered simultaneously, the addition of CC within 4% was the most cost- effective. The mechanical properties and durability of the mixture were maintained while minimizing the CO2 emissions.

Acknowledgement

This study was supported by the National Research Foundation of Korea (grant number NRF-2020R1A2C4002093).

Author contributions

Yi-Han: Conceptualization, Methodology, Investigation, Data curation, Writing - review & editing.

Run-Sheng Lin: Investigation, Writing - review & editing.

Xiao-Yong Wang: Conceptualization, Supervision, Validation, Resources, Project administration, Funding acquisition, Writing - review & editing.

Conflict of interest

The authors state no conflict of interest.

References

He Z H, Shen M L, Shi J Y, Yalcinkaya C, Du S G,Yuan Q. Recycling coral waste into eco-friendly UHPC: Mechanical strength, microstructure, and environmental benefits. Sci Total Environ. 2022; 836: 155424. dio: 10.1016/j.scitotenv.2022.155424.

Huang H, Gao X,Khayat K H. Contribution of fiber orientation to enhancing dynamic properties of UHPC under impact loading. Cement and Concrete Composites. 2021; 121: 104108. dio: 10.1016/j.cemconcomp.2021.104108.

Ren M, Wen X, Gao X,Liu Y. Thermal and mechanical properties of ultra-high performance concrete incorporated with microencapsulated phase change material. Construction and Building Materials. 2021; 273: 121714. dio: 10.1016/j.conbuildmat.2020.121714.

Mo Z, Gao X,Su A. Mechanical performances and microstructures of metakaolin contained UHPC matrix under steam curing conditions. Construction and Building Materials. 2021; 268: 121112. doi:10.1016/j.conbuildmat.2020.121112.

Harrison E, Berenjian A,Seifan M. Recycling of waste glass as aggregate in cement-based materials. Environmental Science and Ecotechnology. 2020; 4:dio: 10.1016/j.ese.2020.100064.

Bajaber M A,Hakeem I Y. UHPC evolution, development, and utilization in construction: a review. Journal of Materials Research and Technology. 2021;
10: 1058-1074. dio: 10.1016/j.jmrt.2020.12.051.

Zhang G Y, Ahn Y H, Lin R S,Wang X Y. Effect of Waste Ceramic Powder on Properties of Alkali-Activated Blast Furnace Slag Paste and Mortar. Polymers (Basel). 2021; 13: 13162817. dio: 10.3390/polym13162817.

Isaia G C, GASTALDInI A L G, Moraes R J C,composites c. Physical and pozzolanic action of mineral additions on the mechanical strength of high- performance concrete. 2003; 25: 69-76.

Ghafari E, Ghahari S A, Costa H, Júlio E, Portugal A,Durães L. Effect of supplementary cementitious materials on autogenous shrinkage of ultra-high performance concrete. Construction and Building Materials. 2016; 127: 43- 48. dio: 10.1016/j.conbuildmat.2016.09.123.

Liu Z,Meng W. Fundamental understanding of carbonation curing and durability of carbonation-cured cement-based composites: A review. Journal of CO2 Utilization. 2021; 44: 101428. dio: 10.1016/j.jcou.2020.101428.

Liu B, Qin J, Shi J, Jiang J, Wu X,He Z. New perspectives on utilization of CO2 sequestration technologies in cement-based materials. Construction and Building Materials. 2021; 272: 121660. dio:10.1016/j.conbuildmat.2020.121660.

He J, Li Z, Zhang X, Wang H, Dong W, Du E, et al. Towards carbon neutrality: A study on China's long-term low-carbon transition pathways and strategies. Environmental Science and Ecotechnology. 2022; 9: 100134. dio: 10.1016/j.ese.2021.100134.

Duan L, Hu W, Deng D, Fang W, Xiong M, Lu P, et al. Impacts of reducing air pollutants and CO2 emissions in urban road transport through 2035 in Chongqing, China. Environmental Science and Ecotechnology. 2021; 8: 100125. dio: 10.1016/j.ese.2021.100125.

Tian S, Wang S, Bai X, Luo G, Li Q, Yang Y, et al. Global patterns and changes of carbon emissions from land use during 1992–2015. Environmental Science and Ecotechnology. 2021; 7: 100108. dio: 10.1016/j.ese.2021.100108.

Di Maria A, Snellings R, Alaerts L, Quaghebeur M,Van Acker K. Environmental assessment of CO2 mineralisation for sustainable construction materials. International Journal of Greenhouse Gas Control. 2020; 93:
102882. dio: 10.1016/j.ijggc.2019.102882.

Hepburn C, Adlen E, Beddington J, Carter E A, Fuss S, Mac Dowell N, et al. The technological and economic prospects for CO2 utilization and removal. Nature. 2019; 575: 87-97. dio: 10.1038/s41586-019-1681-6.

Norhasyima R S,Mahlia T M I. Advances in CO°C utilization technology: A patent landscape review. Journal of CO2 Utilization. 2018; 26: 323-335. dio: 10.1016/j.jcou.2018.05.022.

Raza A, Gholami R, Rezaee R, Rasouli V,Rabiei M. Significant aspects of carbon capture and storage – A review. Petroleum. 2019; 5: 335-340. dio: 10.1016/j.petlm.2018.12.007.

Lee H-S, Lim S-M,Wang X-Y. Optimal Mixture Design of Low-CO2 High- Volume Slag Concrete Considering Climate Change and CO2 Uptake. International Journal of Concrete Structures and Materials. 2019; 13. dio: 10.1186/s40069-019-0359-7.

Rostami V, Shao Y,Boyd A J J J o M i C E. Carbonation curing versus steam curing for precast concrete production. 2012; 24: 1221-1229.

Ashraf W. Carbonation of cement-based materials: Challenges and opportunities. Construction and Building Materials. 2016; 120: 558-570. dio: 10.1016/j.conbuildmat.2016.05.080.

Chen T,Gao X. Effect of carbonation curing regime on strength and microstructure of Portland cement paste. Journal of CO2 Utilization. 2019;34: 74-86. dio: 10.1016/j.jcou.2019.05.034.

Qian X, Wang J, Fang Y,Wang L. Carbon dioxide as an admixture for better performance of OPC-based concrete. Journal of CO2 Utilization. 2018; 25: 31-38. dio: 10.1016/j.jcou.2018.03.007.

Saillio M, Baroghel-Bouny V, Pradelle S, Bertin M, Vincent J,d'Espinose de Lacaillerie J-B. Effect of supplementary cementitious materials on carbonation of cement pastes. Cement and Concrete Research. 2021; 142: 106358. dio: 10.1016/j.cemconres.2021.106358.

Justnes H, Skocek J, Østnor T A, Engelsen C J,Skjølsvold O. Microstructural changes of hydrated cement blended with fly ash upon carbonation. Cement and Concrete Research. 2020; 137: 106192. dio: 10.1016/j.cemconres.2020.106192.

Qin L, Gao X,Li Q. Upcycling carbon dioxide to improve mechanical strength of Portland cement. Journal of Cleaner Production. 2018; 196: 726-738. dio: 10.1016/j.jclepro.2018.06.120.

Han Y, Lin R,Wang X-Y. Performance of sustainable concrete made from waste oyster shell powder and blast furnace slag. Journal of Building Engineering. 2022; 47: 103918. dio: 10.1016/j.jobe.2021.103918.

ASTM C349, Standard Test Method for Compressive Strength of Hydraulic- Cement Mortars (Using Portions of Prisms Broken in Flexure), ASTM International, West Conshohocken, PA, 2018.

ASTM C78, Standard test method for flexural strength of concrete (using simple beamwith third-point loading), ASTM International, West Conshohocken, PA, 2018.

ASTM C597-16, Standard Test Method for Pulse Velocity through Concrete, ASTM International, West Conshohocken, PA, 2016.

AASHTO T 358, Standard Method of Test for Surface Resistivity Indication of Concrete's Ability to Resist Chloride Ion Penetration, American Association of State Highway and Transportation Officials, Washington, DC, 2015.

Lin R-S, Han Y,Wang X-Y. Macro–meso–micro experimental studies of calcined clay limestone cement (LC3) paste subjected to elevated temperature.

Cement and Concrete Composites. 2021; 116: 103871. dio: 10.1016/j.cemconcomp.2020.103871.

Han Y, Lin R,Wang X-Y. Performance and sustainability of quaternary composite paste comprising limestone, calcined Hwangtoh clay, and granulated blast furnace slag. Journal of Building Engineering. 2021; 43:

102655. dio: 10.1016/j.jobe.2021.102655.

Berodier E,Scrivener K J J o t A C S. Understanding the Filler Effect on the Nucleation and Growth ofC°CS°CH. 2014; 97: 3764-3773.

Lothenbach B, Le Saout G, Gallucci E,Scrivener K. Influence of limestone on the hydration of Portland cements. Cement and Concrete Research. 2008; 38: 848-860. dio: 10.1016/j.cemconres.2008.01.002.

Ge Z, Tawfek A M, Zhang H, Yang Y, Yuan H, Sun R, et al. Influence of an extrusion approach on the fiber orientation and mechanical properties of engineering cementitious composite. Construction and Building Materials. 2021; 306: 124876. dio: 10.1016/j.conbuildmat.2021.124876.

Bonavetti V, Donza H, Menendez G, Cabrera O, Irassar E J C,Research C. Limestone filler cement in low w/c concrete: A rational use of energy. 2003;33: 865-871.

Vuk T, Tinta V, Gabrovšek R, Kaučič V J C,Research c. The effects of limestone addition, clinker type and fineness on properties of Portland cement. 2001; 31: 135-139.

Kang S-H, Jeong Y, Tan K H,Moon J. The use of limestone to replace physical filler of quartz powder in UHPFRC. Cement and Concrete Composites. 2018;94: 238-247. dio: 10.1016/j.cemconcomp.2018.09.013.

Dhandapani Y, Santhanam M, Kaladharan G,Ramanathan S. Towards ternary binders involving limestone additions — A review. Cement and Concrete Research. 2021; 143: 106396. dio: 10.1016/j.cemconres.2021.106396.

Zhang H, Xu Y, Gan Y, Chang Z, Schlangen E,Šavija B. Combined experimental and numerical study of uniaxial compression failure of hardened cement paste at micrometre length scale. Cement and Concrete Research. 2019; 126: 105925. dio: 10.1016/j.cemconres.2019.105925.

Ghoddousi P,Adelzade Saadabadi L. Study on hydration products by electrical resistivity for self-compacting concrete with silica fume and metakaolin. Construction and Building Materials. 2017; 154: 219-228. dio: 10.1016/j.conbuildmat.2017.07.178.

Meddah M S, Lmbachiya M C,Dhir R K. Potential use of binary and composite limestone cements in concrete production. Construction and Building Materials. 2014; 58: 193-205. dio: 10.1016/j.conbuildmat.2013.12.012.

Lee H-S,Wang X-Y. Hydration Model and Evaluation of the Properties of Calcined Hwangtoh Binary Blends. International Journal of Concrete Structures and Materials. 2021; 15. dio: 10.1186/s40069-020-00438-5.

Bentz D P. Modeling the influence of limestone filler on cement hydration using CEMHYD3D. Cement and Concrete Composites. 2006; 28: 124-129. dio: 10.1016/j.cemconcomp.2005.10.006.

Ylmén R, Jäglid U, Steenari B-M,Panas I. Early hydration and setting of Portland cement monitored by IR, SEM and Vicat techniques. Cement and Concrete Research. 2009; 39: 433-439. dio:10.1016/j.cemconres.2009.01.017.

Mollah M Y, Kesmez M,Cocke D L. An X-ray diffraction (XRD) and Fourier transform infrared spectroscopic (FT-IR) investigation of the long-term effect on the solidification/stabilization (S/S) of arsenic(V) in Portland cement type-V. Sci Total Environ.2004; 325:255-262. dio: 10.1016/j.scitotenv.2003.09.012.

Trezza M, Lavat A J C,Research C. Analysis of the system 3CaO · Al2O3– CaSO4 · 2H2O–CaCO3–H2O by FT-IR spectroscopy. 2001; 31: 869-872.

Lin R-S, Lee H-S, Han Y,Wang X-Y. Experimental studies on hydration– strength–durability of limestone-cement-calcined Hwangtoh clay ternary composite. Construction and Building Materials. 2021; 269: 121290. dio: 10.1016/j.conbuildmat.2020.121290.

Li Q, Su A,Gao X. Preparation of durable magnesium oxysulfate cement with the incorporation of mineral admixtures and sequestration of carbon dioxide. Sci Total Environ. 2021; 809: 152127. dio: 10.1016/j.scitotenv.2021.152127.

De Weerdt K, Haha M B, Le Saout G, Kjellsen K O, Justnes H, Lothenbach B J C, et al. Hydration mechanisms of ternary Portland cements containing limestone powder and fly ash. 2011; 41: 279-291.

Korea environment industry & technology institute, LCI DB emission factor. http://www.epd.or.kr/eng/lci/lciCo200.do, 2022 (accessed 10 March 2022).

Zhang Y, Zhang J, Luo W, Wang J, Shi J, Zhuang H, et al. Effect of compressive strength and chloride diffusion on life cycle CO2 assessment of concrete containing supplementary cementitious materials. Journal of Cleaner Production. 2019; 218: 450-458. dio: 10.1016/j.jclepro.2019.01.335.

Campos H F, Klein N S, Marques Filho J,Bianchini M. Low-cement high- strength concrete with partial replacement of Portland cement with stone powder and silica fume designed by particle packing optimization. Journal of Cleaner Production. 2020; 261: 121228. dio: 10.1016/j.jclepro.2020.121228.

Yang K-H, Jung Y-B, Cho M-S,Tae S-H. Effect of supplementary cementitious materials on reduction of CO2 emissions from concrete. Journal of Cleaner Production. 2015; 103: 774-783. dio: 10.1016/j.jclepro.2014.03.018.

Environmental and Costs Analysis of Concrete and Ultra-high Performance (UHPC) Bridge Decks Subjected to Local Climate Effects

Jin Fan[1], Wei Huang[2] , Hao Wang[3], Matthew P. Adams[4], Matthew J. Bandelt[5,*]

[1] Department of Civil and Environmental Engineering, University of California, Davis, Davis, CA, 95616 USA; John A. Reif, Jr., Department of Civil and Environmental Engineering, New Jersey Institute of Technology, Newark, NJ, 07102, USA, jdfan@ucdavis .edu

[2] Department of Civil and Environmental Engineering, Rutgers, The State University of New Jersey, Piscataway, 08854, USA, wh288@scarletmail .rutgers .edu

[3] Department of Civil and Environmental Engineering, Rutgers, The State University of New Jersey, Piscataway, 08854, USA, hw261@soe .rutgers .edu

[4] John A. Reif, Jr., Department of Civil and Environmental Engineering, New Jersey Institute of Technology, Newark, NJ, 07102, USA, matthew.p .adams@njit .edu

[5] John A. Reif, Jr., Department of Civil and Environmental Engineering, New Jersey Institute of Technology, Newark, NJ, 07102, USA, bandelt@njit .edu

Abstract

Ultra-high-performance concrete (UHPC) exhibits high compressive strength and good durability. However, owing to the dense microstructure of UHPC, carbonation curing cannot be performed to capture and sequester carbon dioxide (CO_2). In this study, CO_2 was added to UHPC indirectly. Gaseous CO_2 was first converted into solid calcium carbonate ($CaCO_3$) using calcium hydroxide, and the converted $CaCO_3$ was then added to UHPC at 2, 4, and 6 wt.% based on the cementitious material. The performance and sustainability of UHPC with indirect CO_2 addition were investigated through macroscopic and microscopic experiments. The experimental results showed that the method used did not negatively affect the performance of UHPC. Compared with the control group, the early strength, ultrasonic velocity, and resistivity of UHPC containing solid CO_2 improved to varying degrees. Microscopic experiments, such as heat of hydration and thermogravimetric analysis (TGA), demonstrated that adding captured CO_2 accelerated the hydration rate of the paste. Finally, the CO_2 emissions were normalized according to the compressive strength and resistivity at 28 days. The results indicated that the CO_2 emissions per unit compressive strength and unit resistivity of UHPC with CO_2 were lower than those of the control group.

Keywords: Ultra-high-performance concrete; Microstructure; CO_2 absorption.

1. Introduction and Background

Production of portland cement, the main contributor of CO_2 emissions from concrete produc- tion, currently exceeds 4 billion tons annually [1]. Consequently, concrete, the most widely used construction material, accounts for approximately 8% of global anthropogenic CO_2 emissions [2, 3]. In the midst of the growing climate crisis, the demand for construction materials is expected to grow due to trends in development, urbanization, and population growth [4]. With concrete consumption expected to grow, it is imperative to adapt the construction sector to prevent additional emissions.

In addition to climate challenges, maintenance and rehabilitation of critical infrastructure, such as highway bridges, present ongoing challenges for bridge owners and transportation agencies. These structures are subjected to constant traffic loads; and bridge decks, which are most commonly made of concrete, are subjected to harsh environmental conditions leading to deterioration over time [5]. To address these challenges, there is growing interest in exploring non-conventional building materials that can promote an environmentally sustainable and socially resilient built environment [6, 7].

Ultra-high performance concrete (UHPC) is one such revolutionary material that has demon- strated improved performance and longevity [8, 9, 5]. Compared to conventional concrete, UHPC exhibits superior resistance to cracking [10, 11] and harmful material ingress [12, 13], and is able to achieve significantly higher mechanical strength [14, 15] due to its dense microstructure and the incorporation of steel fibers [16, 17]. Although UHPC's mechanical [18, 19, 20, 21, 22] and dura- bility performance [23, 24, 25, 26] have been extensively studied, its environmental impacts have received limited attention. At the material level, UHPC has higher environmental impacts than concrete due to the higher volume of portland cement and steel fibers [27]. However, due to UHPC's high mechanical strength, UHPC structures can reduce material volume and thus reduce carbon emissions by up to 36.6%, as demonstrated by Joe and Moustafa [28]. Similarly, Sameer et al. [29] indicated that UHPC bridge design could lower the carbon footprint of the bridge by 14% compared to reinforced concrete bridges. In contradiction, studies by Stengel and Schießl [30] and M´arquez et al. [31] showed that the adoption of UHPC material did not produce a more environmentally friendly bridge construction, despite a significant reduction in the volume of materials. Meanwhile, beyond the construction stage, UHPC structures could have lower carbon emissions compared to conventional concrete structures when considering the use and maintenance stage. For example, Dong [32] found that a UHPC girder had lower carbon emission compared to a concrete girder due to less frequent maintenance requirements over the same lifespan.

Among the limited studies that considered the maintenance stages of a structure's life cycle, even fewer have integrated life-cycle prediction analysis. This analysis is critical for determining life spans and thus accurately quantifying life cycle carbon emissions. The study by Fan et al.[33] predicted the lifespans of a set of UHPC beams through multi-physics modeling and found that UHPC's high mechanical strength and excellent durability performance resulted in 48% lower carbon emissions compared to conventional concrete beams when considering maintenance stages. However, the demolition stage and the allocation of waste materials to landfills also need to be quantified. Furthermore, none of those studies, except Stengel and Schießl [30] considered categories of environmental impacts other than carbon emission, such as air pollutants. The inconsistent quantification of carbon emissions from the construction stage, the lack of service life predictions, the limited investigation of cradle-to-grave life cycle analysis, and the insufficient quantification of environmental impacts suggest that a comprehensive study of whole-stage life cycle analysis, based on physics-informed models, is needed to better achieve sustainable and resilient design goals when adopting UHPC materials. In addition to carbon emissions, other environmental impacts such as air pollutants must also be considered to avoid additional health risks to the local community. Finally, life cycle costs must be investigated to address the economic concerns of UHPC structures. The external societal costs of climate damage, quantified by the social costs of carbon (SCC), remain unexplored for UHPC materials.

This study aims to quantify and compare the long-term serviceability characteristics, environmental impacts, and costs of a reinforced normal-strength concrete bridge deck and a redesigned, smaller-sized reinforced UHPC bridge deck. A time-dependent multi-physics modeling framework was employed [34] which integrates realistic regional environmental factors such as the periodic applications of de-icing salts and fluctuating temperatures to simulate the performance of the bridge decks over their service life. Chloride profiles and structural deterioration after corrosion are used to assess the service life performance of reinforced UHPC and reinforced concrete bridge decks. The environmental impacts from cradle to grave, including greenhouse gas (GHG) emissions, air pollutants of nitrogen oxides (NO_X), sulfur oxides (SO_X), volatile organic compounds (VOCs), particular matter less than 10 µm (PM_{10}) and particulate matter less than 2.5 µm ($PM_{2.5}$), and carbon monoxide (CO) were quantified. The life cycle costs, including SCC, of the reinforced concrete and reinforced UHPC bridge decks were compared.

2. Background of Reinforced Concrete Bridge Deck Deterioration

In cold regions, such as the case selected in this study, de-icing materials are regularly applied to melt snow on roads and bridges. Corrosion of reinforcement steel can initiate and propagate due to accumulation of de-icing materials, and eventually deteriorate reinforced concrete infrastructures, especially in bridge decks in locations with high traffic loading. It is noted that there are many deterioration mechanisms that can shorten the service life of reinforced concrete structures, only corrosion (the most common one) was considered. The fundamental background of corrosion is briefly introduced in the following subsections.

2.1. Chloride Transport

Chloride transport in sound cementitious materials is a diffusion process governed by Fick's second law [35]:

$$\frac{\partial C_{\mathrm{Cl}}}{\partial t} = D_{\mathrm{Cl}} \left(\frac{\partial^2 C_{\mathrm{Cl}}}{\partial x^2} + \frac{\partial^2 C_{\mathrm{Cl}}}{\partial y^2} \right) \tag{1}$$

where C_{Cl} (% mass of cementitious materials) is the chloride concentration in concrete, D_{Cl} (m^2/s) indicates the chloride diffusion coefficient, and t (seconds) is the diffusion time.

A common method used to account for the effect of cracking on chloride transport in cementitious materials is the smeared cracking modeling technique. In such models, discrete crack geometry is not explicitly modeled. Instead, higher chloride diffusion coefficients are integrated in the cracked zones. The nonlinear relationships between crack width and the reference chloride diffusion coefficients of concrete and UHPC materials have been empirically described in the literature by the following equations, respectively [36, 13]:

$$D_{\mathrm{ref\_C}} = \begin{cases} 2 \times 10^{-11} w - 4 \times 10^{-10}, 30\mu m \leq w \leq 80\mu m \\ 14 \times 10^{-10}, w > 80\mu m \end{cases} \tag{2}$$

$$D_{\mathrm{ref\_UHPC}} = \begin{cases} 4 \times 10^{-12} w - 3 \times 10^{-11}, 10\mu m \leq w \leq 80\mu m \\ 3 \times 10^{-10}, w > 80\mu m \end{cases} \tag{3}$$

where w is crack width (µm). The chloride diffusion coefficient under the influence of temperature fluctuation is:

$$DCl = Dref \cdot f(T) \tag{4}$$

f(T) is described as follows [37]:

$$f(T) = \exp\left[\frac{U}{R} \left(\frac{1}{T_{\mathrm{ref}}} - \frac{1}{T} \right) \right] \tag{5}$$

where U is the activation energy (44.6 KJ/mol), R is the gas constant (8.3 J/mol), Tref is the reference temperature (293.2 K) of the measured diffusion coefficient, and *T* is the concrete/UHPC temperature [37]. The impact of cracking on oxygen penetration in concrete/UHPC is described as [38]:

$$D_{\mathrm{O_2}}^{\mathrm{crack}} = \begin{cases} D_{\mathrm{O_2}}^{\mathrm{sound}}, w \leq w_{cr} \\ D_{\mathrm{O_2}}^{\mathrm{sound}} \times (w/w_{cr})^3, w > w_{cr} \end{cases} \tag{6}$$

where D* jc3 * hps13 \o\al\s\up 3crO* jc3 * hps13 \o\al\s\up 3a2$^{\mathrm{ck}}$ and D* jc3 * hps13 \o\al\s\up 3soO* jc3 * hps13 \o\al\s\up 3u2$^{\mathrm{nd}}$ are the oxygen diffusion coefficients in cracked and sound areas, respectively.

w_{cr} is the critical crack width for the study and is assumed as 0.1 mm [39, 40, 38].

2.2. Corrosion Initiation

Cementitious materials, including concrete and UHPC, serve as barriers against de-icing materials that can cause corrosion in steel reinforcement. Corrosion occurs gradually over time once the concentration of such materials reaches a threshold level, known as the critical chloride content $\mathrm{Cl}_{\mathrm{crit}}$ [41, 42].

2.3. Corrosion Propagation

Corrosion is an electrochemical process, in which the electrons are freed from the steel and then react with water and oxygen. The electrochemical potential ϕ (mV) distribution and electrical charge flow i (A/m^2) are governed by Laplace's equation and Ohm's law, respectively [43, 44, 45]:

$$\nabla \cdot \left(\frac{1}{\rho} \nabla \phi \right) = 0 \tag{7}$$

$$i = -\frac{1}{\rho} \nabla \phi \tag{8}$$

The numerical polarization equation for the anodic reaction is [45]: [45]:

$$i_{\mathrm{Fe}} = i_{\mathrm{Fe}}^0 \exp \left(2.303 \frac{\phi - \phi_{\mathrm{Fe}}^0}{\beta_{\mathrm{Fe}}} \right) \tag{9}$$

The polarization equation of cathodic reaction is [45]:

$$i_{\mathrm{O_2}} = \frac{i_{\mathrm{O_2}}^0 \exp \left(2.303 \frac{\phi - \phi_{\mathrm{O_2}}^0}{\beta_{\mathrm{O_2}}} \right)}{1 + \frac{i_{\mathrm{O_2}}^0}{i_{\mathrm{L}}} \exp \left(2.303 \frac{\phi - \phi_{\mathrm{O_2}}^0}{\beta_{\mathrm{O_2}}} \right)} \tag{10}$$

i_{Fe}^0 and $i_{\mathrm{O_2}}^0$ represent the anodic and cathodic exchange current density, respectively. ϕ_{Fe}^0 and $\phi_{\mathrm{O_2}}^0$ are the anodic and cathodic equilibrium potentials, respectively. β_{Fe} is the anodic Tafel constant, and $\beta_{\mathrm{O_2}}$ denotes the cathodic Tafel constant. i_L refers to the limiting current density [46, 47].

3. Service Life Modeling

3.1. Service Life Modeling Procedure

A time-dependent multi-physics modeling approach, building on the authors' previous work [34], was used in this study to predict the service life performance of the reinforced concrete and rein- forced UHPC bridge decks. The de-icing material penetration, corrosion propagation, and structural response were connected through multiple modeling platforms and time steps. First, the initial struc- tural response under traffic loading was simulated using DIANA Version 10.5 [48]. The transport properties of concrete and UHPC were then updated and incorporated into the chloride penetration analysis using the software package COMSOL Multiphysics Version 5.4 [49]. Next, the corrosion propagation simulation calculated rust expansion thickness, which was applied as an additional displacement load alongside traffic loading in the structural analysis. This iterative process was repeated for subsequent time steps. The reader is referred to Fan et al. [34] for further background on the modeling approach.

At each time step, the corroded area of the steel reinforcement and the cracking status of the concrete and UHPC were updated. The time intervals for the reinforced concrete and reinforced UHPC bridge deck were set to four months and five years, respectively. The larger time step for the reinforced UHPC specimen was adopted to maintain the balance between computing efficiency and modeling accuracy.

3.2. Bridge Deck Descriptions and Boundary Conditions

Figure 1(a) shows a representative cross-section design of a reinforced concrete bridge deck. The thickness of the reinforced concrete bridge deck was 250 mm. The top and bottom concrete cover was 63 mm and 25 mm, respectively. The reinforcement bar diameter was 19mm. The span length was 3300 mm and only half of the span was simulated due to the symmetrical geometry.

Sustained traffic load was simplified as displacements applied at midspan. The reinforced UHPC bridge deck was redesigned with a reduced depth of 125 mm, which resulted in a load capacity (145.1 kN) equivalent to that of the reinforced concrete bridge deck (142 .3 kN). Additionally, the cover depth of the reinforced UHPC bridge deck was reduced to 25 mm. According to ACI 224 R, the allowable crack width for the tensile face of a reinforced concrete structure exposed to de-icing chemicals is 0.18 mm [50]. Thus, load within the service load range that resulted in a crack width of 0.18 mm was chosen as the initial condition for the reinforced concrete bridge deck, which was 41 kN. For the reinforced UHPC bridge deck, the initial crack width at the same loading level (41 kN) was 0.017 mm, which was one order of magnitude smaller than that of the reinforced concrete bridge deck.

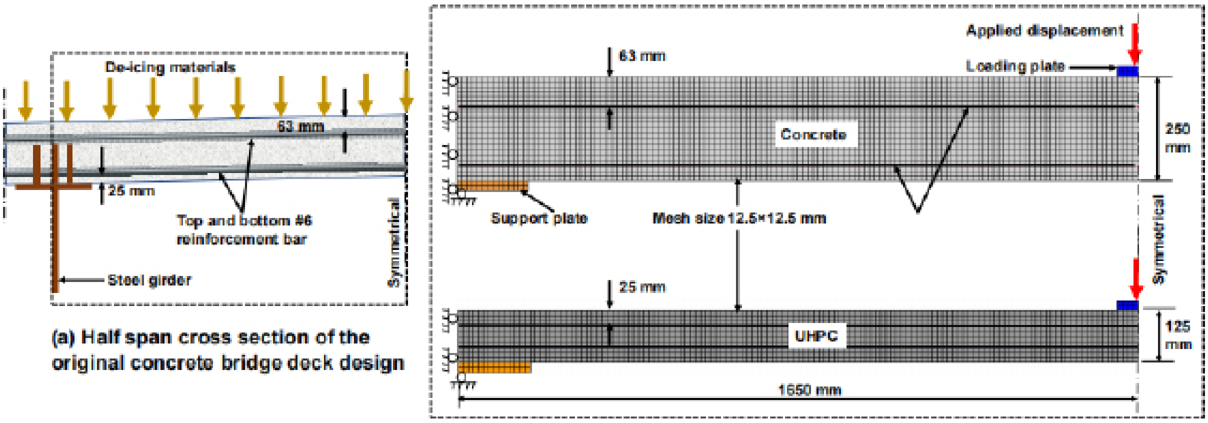

(a) Half span cross section of the original concrete bridge deck design

(b) Finite element modeling set up

Figure 1: Concrete bridge deck and the finite element modeling (FEM) set up.

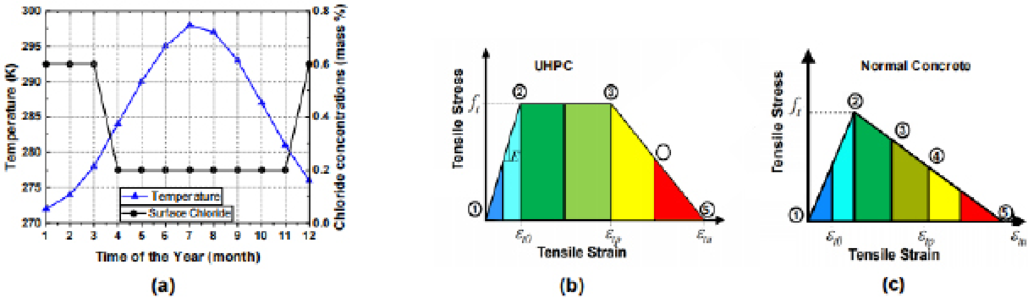

(a)

(b)

(c)

Figure 2: (a), Surface chloride conditions and temperature fluctuation; reference stress strain contour of (b) UHPC, and (c) concrete.

For bridges located in cold regions, de-icing materials used during the snowing seasons are the major source of chloride ions. In this study, a steady and high concentration of chloride ions (0.6% of concrete/UHPC mass) was assumed to be applied at the top surface of the bridge deck for four months during the snow season. A lower residual surface chloride concentration of 0.2% of concrete/UHPC mass was assumed for the remainder of the year after the snow season [51]. Oxygen was assumed to be available at both the top and bottom sides. The seasonal variations in surface chloride content and local temperature fluctuations within the studied region are graphically presented in Figure 2(a) [51, 52].

3.3. Structural Response Modeling

Figure 1(b) shows the structural response modeling set up in DIANA Version 10.5 [48]. As shown in Figure 1(b), the left corner and left side deformation were restrained. A prescribed incremental displacement of 0.25 mm was applied at midspan to simulate the traffic loading. A total strainbased fixed-crack model with a shear retention factor of 0.01 was adopted to simulate the concrete and UHPC materials [53]. The mesh size of both concrete and UHPC was 7 mm × 7 mm. The reinforcement bar was simulated as truss elements with the same mesh size. A line search algorithm and a secant Newton-Raphson scheme were selected for numerical convergence. The convergence criteria for energy, displacement, and force norms were 0.01%, 0.1% and 1%, respectively [11].

The mixture design of the concrete and UHPC bridge are shown in Table 1, the steel fiber volume of UHPC was 2%. The mechanical properties of normal strength concrete and UHPC were obtained from Shao and Billington [20] and are summarized in Table 2. Normal strength concrete had a tensile strength of 3.1 MPa with a tensile fracture energy of 0.144 MPa-mm, and a compressive strength of 41.9 MPa with a compressive fracture energy of 35.7 MPa-mm [20]. UHPC, on the other hand, had a tensile strength of 10.5 MPa and a tensile fracture energy of 11.2 MPa-mm, as well as a compressive strength of 185.8 MPa with a compressive fracture energy of 180.0 MPa-mm [20]. The reinforcing bar used in the study had a yielding strength of 455 MPa and an ultimate strength of 675 MPa [54].

Table 1: Mixture design and transport distances of raw materials to mixture plant (A2)

Materials	Unit	Concrete	UHPC	Unit	Rail	Truck	Ship
Glass Power	kg/m^2	0	26	ton-km	6	139	7
Silica Fume	kg/m^2	0	29	ton-km	6	139	7
Portland Cement	kg/m^2	106	89	ton-km	6	139	7
Fine Aggregate	kg/m^2	214	0	ton-km	21	54	14
Coarse Aggregate	kg/m^2	190	0	ton-km	26	39	11
Water	kg/m^2	57	14	ton-km	0	0	0
Silica Sand	kg/m^2	0	128	ton-km	26	39	11
Steel Bar	kg/m^2	42	27	ton-km	0	300	0
Steel Fiber	kg/m^2	0	20	ton-km	0	300	0
Steel Girder	kg/m^2	133	117	ton-km	0	300	0
Superplasticizer	kg/m^2	0	8	ton-km	0	300	0

3.4. Diffusion and Corrosion Modeling

Diffusion and corrosion modeling was completed in COMSOL Multiphysics Version 5.4 [49]. The impact of temperature on chloride transport was considered using the Equation (4). The oxygen ingress was considered to take place through both the top and bottom surfaces of the bridge deck in the computational model. On the other hand, chloride ion penetration was assumed to occur exclusively from the top surface, where de-icing material was applied.

Table 2: Mechanical properties of concrete, UHPC and steel

Mechanical properties	Notation	Unit	Concrete	UHPC	Steel
Tensile strength	f_t	MPa	3.1	10.5	-
Strain at crack initiation	ε_{t0}	%	0.01	0.019	-
Strain at onset of softening	ε_{tp}	%	0.01	0.2	-
Compressive strength	f'_c	MPa	41.9	185.8	-
Modulus of elasticity	E	GPa	31.2	53.5	200
Tensile fracture energy	G_f	MPa-mm	0.144	11.2	-
Compressive fracture energy	G_c	MPa-mm	35.7	180.0	-
Yield strength	f_y	MPa	-		455
Ultimate strength	f_u	MPa	-		675
Poisson's ratio	ν	mm/mm	0.2	0.18	0.30

The reference chloride transport coefficients for concrete and UHPC were reported as D_{ref_c} = 1.3 × 10^{-11} m^2/s and D_{ref_UHPC} = 4.5 × 10^{-13} m^2/s, respectively [55]. The oxygen transport coefficients for concrete and UHPC were reported as $D_{O2\_\_c}$ = 3.02 × 10^{-9} m^2/s and D_{O2_UHPC} = 4.2×10^{-10} m^2/s, respectively [55]. The electrical resistivity of concrete, ρ_c, was 159 Ω · m, while the electrical resistivity of UHPC (ρ_{UHPC}) at the same level of saturation was 23067 Ω·m due to the dense material property [55,56]. The anodic Tafel slopes, β_{Fe_c} = 65 mV/dec and β_{Fe_UHPC} = 61 mV/dec, as well as cathodic Tafel slopes β_{O2_c} = —138.6 mV/dec and β_{O2_UHPC}= —130.9 mV/dec) were adopted from the literature [55]. The anodic equilibrium potential was set as ϕ* jc3 * hps13 \o\al\s\up 30Fe = —600 mV, while the cathodic equilibrium potential was set as ϕ* jc3 * hps13 \o\al\s\up 30O_2 = 200 mV. The anodic and cathodic exchange current densities were i* jc3 * hps13 \o\al\s\up 30Fe = 2.75 × 10^{-4}A/m^2 and ϕ* jc3 * hps13 \o\al\s\up 30O_2 = 6 × 10^{-6} A/m^2, respectively [55]. In this study, a constant Cl_{crit} equal to 0.06% of concrete/UHPC mass is assumed [57, 58]. Surface oxygen concentration O_{2surf} = 0.268 mol/m^3 [39], chloride diffusion activation energy U = 44.6 KJ/mol, gas constant R = 8.3 J/mol, and reference temperature T_{ref} = 293.2 K. Detailed descriptions of the input parameters can be found in the authors' previous work [34].

After obtaining corrosion current density from corrosion modeling, the cross section loss and rust expansion was calculated [45, 59, 34] :

$$\sigma(t)=\frac{\int_0^t i_{\mathrm{corr}}(t)dt\cdot M_{\mathrm{s}}}{Z_{\mathrm{Fe}}\cdot F\cdot\rho_{\mathrm{s}}} \tag{11}$$

where t is the corrosion time (seconds), M_s = 55.85 g/mol is the atomic mass of iron, Z_{Fe} = 2 is the valency of the anodic reaction, and ρ_s = 7800 kg/m^3 is the steel density.

The formation of corrosion products (rust) can occupy a greater volume than the original steel.

As a result, after part of the corrosion products fill the steel concrete interface, further accumulation of these products at the steel concrete interface can generate internal pressure on the steel and concrete. The thickness of the rust layer expansion can then be calculated using the following equation:

$$u(t) = (n — 1)\sigma(t) \tag{12}$$

where n is the volume expansion ratio of rust to steel and is assumed to be 3 in this study [60, 39, 42, 34]. Rust deformation was neglected in this analysis [61].

4. Environmental Impacts Analysis and Life-cycle Costs

4.1. Environmental Impact Analysis Scope

An attributional life cycle assessment (ALCA)—focusing on the directly attributable environmental impacts over the product's full life cycle, was applied to the cradle-to-grave approach., in which emissions were assessed from raw material acquisition (sourcing, processing), construction (batching, pumping, curing), maintenance, and end-of-life through the grave (demolition, disposal of waste material). Transport-associated impacts were also considered.

A declared unit of 1 m^2 of reinforced concrete/UHPC were considered to determine life cycle inventories (LCI). In this study, carbon dioxide (CO_2), methane (CH_4), and nitrous oxide (N_2O) and their impacts were consolidated into CO2-equivalent ($CO_{2\text{-}eq}$) emissions to analyze GHG emissions, based on the 100-year global warming potentials [62]. The air pollutant emissions of nitrogen oxides (NO_X), sulfur oxides (SO_X), volatile organic compounds (VOC_s), carbon monoxide (CO), particular matter less than 10 µm (PM_{10}), and particulate matter less than 2.5 µm ($PM_{2.5}$) were also quantified.

4.2. Environmental Impact Inputs and Assumptions

Emission factors of the life cycle stages are shown in Table 3. The emission factors of the raw materials (A1) were adopted from an open source tool, OpenConcrete, by Kim et al. [63]. Emission factors of steel girder and superplasticizer were adopted from Ecoinvent 3 database version 3 (a commonly used LCI database). Producing steel fiber and steel bar requires additional processing compared to that of a steel girder, therefore higher emission factors were assumed for steel fiber and steel bar. A2 is the raw material transport stage, the associated emission factors were based on US national average transport distances of rail, truck, and ship, according to Nahlik et al. [64]. The transport distances and modes of regular concrete constituents, steel, and admixture are shown in Table 1. The transport distances of glass powder, silica fume, PC, and aggregates were adopted from Marceau et al. [65]. Steel materials and superplasticizer were assumed to be transported with a distance of 300 km. For batching one cubic meter of UHPC, 0.35 liter of oil and 7.1 kWh of electricity were used while bathing the same amount of concrete consumed 0.35 liter of oil and 4.4 kWh of electricity [29]. The emission factors of electricity is based on New Jersey electricity grid of US. Mixed concrete and UHPC were assumed to be transported (A4) 300 km to the construction site by truck within New Jersey. According to Sameer et al. [29], pumping of one cubic meter of concrete or UHPC consumed 2.7 kWh. Demolition of one cubic meter of concrete consumed 0.76 liter of oil and 18.3 kWh of electricity while demolition of the same amount of UHPC consumed 2 liters of oil and 36.5 kWh of electricity. Transport distance of the demolished waste to the landfill site (C2) was assumed to be 100 km. For the declared unit of 1 m^2 bridge deck, the volume of concrete and UHPC were 0.25 m^3 and 0.125 m^3, respectively.

Table 3: Life cycle stages and emissions data

Life cycle stages	**Materials/Processes**	**Unit**	**kg GHG**	**kg** CO_2	**kg** CH_4	**kg** N_2O	**kg** NO_X	**kg** SO_X	**kg** PM_{10}	**kg** $PM_{2.5}$	**kg** VOC	**kg** CO
A1	Glass Powder	per kg	5.53E-02	5.51E-02	2.52E-06	4.55E-07	4.18E-05	5.79E-05	2.11E-05	1.31E-05	1.90E-06	5.15E-05
A1	Silica Fume	per kg	0.00E+00	0.00E+00	0.00E+00	0.00E+00	0.00E+00	0.00E+00	9.30E-06	9.30E-06	0.00E+00	0.00E+00
A1	PC	per kg	9.50E-01	9.47E-01	4.02E-05	6.44E-06	3.37E-04	2.65E-03	4.46E-04	3.69E-04	1.03E-05	6.16E-04
A1	Fine Aggregate	per kg	2.07E-03	2.06E-03	9.00E-08	1.70E-08	1.56E-06	2.17E-06	1.17E-04	1.17E-04	7.10E-08	1.93E-06
A1	Coarse Aggregate	per kg	3.16E-03	3.15E-03	1.40E-07	2.60E-08	2.39E-06	3.31E-06	1.19E-04	1.18E-04	1.08E-07	2.95E-06
A1	Water	per kg	0.00E+00	0.00E+00	0.00E+00	0.00E+00	0.00E+00	0.00E+00	0.00E+00	0.00E+00	0.00E+00	0.00E+00
A1	Silica Sand	per kg	5.53E-02	5.51E-02	2.52E-06	4.55E-07	4.18E-05	5.79E-05	2.11E-05	1.31E-05	1.90E-06	5.15E-05
A1	Steel Bar	per kg	1.81E+00	1.81E+00	1.05E-02	3.23E-05	4.73E-03	4.49E-03	2.73E-03	2.66E-03	1.46E-02	2.39E-02
A1	Steel Fiber	per kg	1.81E+00	1.81E+00	1.05E-02	3.23E-05	4.73E-03	4.49E-03	2.73E-03	2.66E-03	1.46E-02	2.39E-02
A1	Steel Girder	per kg	9.06E-01	9.06E-01	5.25E-03	1.62E-05	2.37E-03	2.24E-03	1.37E-03	1.33E-03	7.32E-03	1.20E-02
A1	Superplasticizer	per kg	4.64E-01	4.64E-01	3.27E-05	1.69E-05	1.48E-03	2.75E-03	1.69E-04	8.35E-05	4.15E-05	8.81E-04
A2	Transport, rail	per ton-km	1.40E-02	1.40E-02	0.00E+00	0.00E+00	1.10E-04	3.96E-05	8.50E-07	2.89E-06	9.33E-06	3.88E-05
A2	Transport, truck	per ton-km	8.65E-02	8.65E-02	0.00E+00	0.00E+00	5.05E-04	5.20E-07	1.91E-05	1.50E-05	2.83E-05	9.23E-05
A2	Transport, ship	per ton-km	1.80E-03	1.80E-03	0.00E+00	0.00E+00	5.80E-05	1.27E-05	9.33E-06	2.53E-06	1.93E-06	3.75E-06
A3	Batching Concrete	per m^3	2.41E+00	2.40E+00	9.98E-05	1.81E-05	1.59E-03	1.62E-03	2.81E-04	6.97E-05	5.10E-05	1.36E-03
A3	Batching UHPC	per m^3	3.27E+00	3.25E+00	1.39E-04	2.51E-05	2.24E-03	2.52E-03	4.43E-04	1.08E-04	8.03E-05	2.16E-03
A4	Transport, truck	per ton-km	8.65E-02	8.65E-02	0.00E+00	0.00E+00	5.05E-04	5.20E-07	1.91E-05	1.50E-05	2.83E-05	9.23E-05
A5	Pumping (electricity)	per MJ	8.92E-02	8.89E-02	4.06E-06	7.33E-07	6.75E-05	9.35E-05	1.69E-05	4.02E-06	3.06E-06	8.31E-05
A5	Curing (oil)	per MJ	7.22E-02	7.20E-02	2.56E-06	4.69E-07	3.77E-05	9.82E-06	7.81E-07	4.12E-07	1.61E-07	2.87E-06
C1	Demolition (oil)	per MJ	7.22E-02	7.20E-02	2.56E-06	4.69E-07	3.77E-05	9.82E-06	7.81E-07	4.12E-07	1.61E-07	2.87E-06
C2	Transport (truck)	per ton-km	8.65E-02	8.65E-02	0.00E+00	0.00E+00	5.05E-04	5.20E-07	1.91E-05	1.50E-05	2.83E-05	9.23E-05
C3	Crushing Concrete	per m^3	3.78E+00	3.76E+00	1.50E-04	2.73E-05	2.35E-03	2.00E-03	3.32E-04	8.56E-05	6.07E-05	1.60E-03
C3	Crushing UHPC	per m^3	7.55E+00	7.53E+00	3.00E-04	5.47E-05	4.71E-03	4.00E-03	6.65E-04	1.71E-04	1.21E-04	3.21E-03

4.3. Social Impacts Analysis

In this study, SCC is evaluated as a theoretical measure that accounts for the multifaceted im- pacts of climate change. These include changes in agricultural productivity, health-related effects, property damage caused by flooding and extreme weather events, disruptions to energy infrastruc- ture, heightened risks of conflict, climate-induced migration, and the economic value of ecosystem services [66]. The SCC and GHG emissions of concrete and UHPC bridge decks are applied to explore how incorporating externalized costs into market pricing might influence the relative differ- ences between these mixtures. The externalized climate costs vary depending on the specific type of greenhouse gas (e.g., CO_2, CH_4, N_2O) and the timing of emission changes. In this analysis, the social costs of CO_2, CH_4, and N_2O are assumed to be \$116, \$3, 800, and \$45, 000, respectively, using a 2.5% discount rate [66].

4.4. Life-cycle Costs Analysis Methodology

Life cycle cost assessment (LCCA) is an effective method to evaluate the accumulated cost of managing a facility or processing a project with flexibility and comprehensiveness. The LCCA can be used to assess all significant and relevant costs over the service life cycle of a bridge deck, helping to optimize bridge deck designs that will implement the project objective at the lowest budget while with satisfied service level and performance.

The total cost of a bridge deck during its service life is mainly constituted of those from stages and activities such as initial construction, routing inspection, maintenance, demolition and recycling, which can be expressed as [67]:

$$LCC_{\mathrm{NPV}} = C_{\mathrm{ic}} + \sum_{i=1}^{n_{\mathrm{ri}}} \frac{C_{\mathrm{ri}}}{(1+r)^{t_i}} + \sum_{k=1}^{n_{\mathrm{mt}}} \frac{C_{\mathrm{mt}}}{(1+r)^{t_k}} + \frac{C_{\mathrm{d}}}{(1+r)^{\mathrm{T}}} - \frac{R_{\mathrm{v}}}{(1+r)^{\mathrm{T}}} \tag{13}$$

where LCC_{NPV} is the total cost represented by Net Present Value (NPV); r is the monetary discount rate; C_{ic}, C_{ri}, C_{mt}, C_d and R_v are costs of different activities: initial construction, routine inspection, maintenance, demolition and residual value, respectively; n_{ri} and n_{mt} are number of corresponding activities during the investigated period; T is the investigated service life.

4.5. Life-cycle Costs Inputs and Assumptions

The life cycle costs of the concrete and UHPC bridge decks were analyzed based on the results of the time-dependent multi-physics modeling. The investigated life period is 100 years consider- ing the accumulated costs from initial construction, routing inspection, minor maintenance, major maintenance, and deck overlay. The costs from end of life such as demolition and recycling are not considered for a comparative analysis of the two types of bridge decks. The assessed dimension of the bridge deck follows the dimensional set up of FEM model, in which the thickness of concrete and UHPC decks are 250 mm and 125 mm, respectively, with both 1 lane width (3.7 m travel lane) and 1 mile length (1.6 km). It is assumed that the same traffic conditions are applied on these two bridges and the costs from traffic delay due to road closure for maintenance are not considered.

The initial construction and replacement costs of the concrete bridge deck are set as \$1 , 000/m^2 [68]. The unit costs of major and minor maintenance are set as \$500 and \$20 per square meter, respectively [68]. The routine inspection consists of observations and measurements needed to de- termine the physical and functional condition of the bridge. Minor maintenance is considered as preventive action before major maintenance (repair)[32, 33].The unit cost of inspection is set as \$2/m^2 [68].

As for the bridge deck made with UHPC, related literature indicated that the material cost of UHPC is about 4 times of conventional concrete [32,69,33], and the thickness of UHPC deck can be much thinner owing to the advantages of high strength and reliable durability of UHPC [70], which is in accordance with the dimension set up in this study. Therefore, the normalized unit initial cost of UHPC bridge deck can be set as \$2, 000/m^2, which is 2 times than that of RC bridge deck considering the thinner thickness of UHPC. The costs of minor maintenance and routine inspection for UHPC bridge deck are assumed to be the same as those of RC bridge deck.

5. Results

This section presents the results of chloride content distribution and bridge deck deterioration, with a focus on comparing the findings between the reinforced concrete bridge deck and the reinforced UHPC bridge deck. The investigation includes the service life span, considering factors such as reinforcing bar cross-section loss, damage ratings of the cementitious materials, and the progression of cracking over time due to chloride exposure. Additionally, environmental impacts and life cycle costs, including social costs, were calculated based on the anticipated service life span. Figure 2(b) and (c) illustrates the reference contours of principal tensile strains for UHPC and concrete, serving as a measure of the level of cracking in the respective materials.

5.1. Chloride Profiles

Figure 3 (a)-(d) shows the comparative results of chloride distribution and cracking level following 30 years of chloride exposure under sustained traffic loading for both the reinforced concrete and reinforced UHPC bridge decks. As depicted in Figure 3, it is evident that the reinforced concrete bridge deck experienced significantly faster chloride ingress compared to the reinforced UHPC bridge deck under the same initial load condition. Additionally, the corrosion level in the reinforced concrete bridge deck reached 100% for the top reinforcing bar, whereas the reinforced UHPC bridge deck exhibited only 13.3% of the top reinforcing bar corrosion, despite having a concrete cover that was 2.52 times thicker than that of UHPC. The simulation results also indicate that corrosion initiation in the reinforcing bars of the reinforced concrete bridge deck occurred after one year, whereas in the reinforced UHPC bridge deck, it was 25 years. This notable difference can be attributed to the combined effect of slow chloride transportation and enhanced cracking resistance provided by UHPC beams. The simulation results, particularly in terms of chloride profiles, further verify the exceptional corrosion resistance of UHPC material.

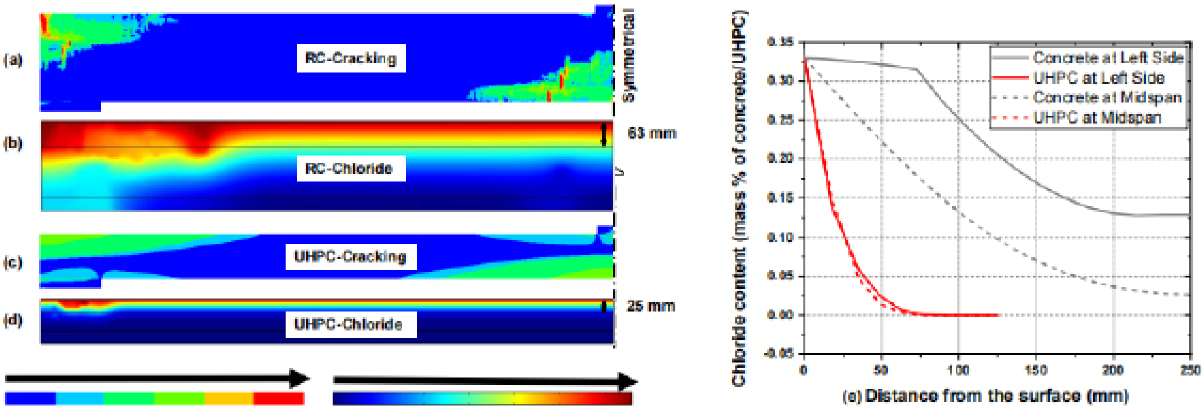

Figure 3: Damage patterns, chloride contours, and chloride profile.

Figure 3(e) provides additional insights into the chloride profiles at different depths of the bridge decks, specifically at the left side and midspan. It is observed that cracks predominantly occurred at the left side of the top surface when the traffic load was applied at midspan. Consequently, larger crack widths and a higher number of cracks were present on the left side of the top surface, where chloride was applied, leading to accelerated chloride transport on the left side of the reinforced concrete bridge deck. As a result, chloride concentrations were significantly higher on the left side of the concrete bridge deck. However, minimal variations in chloride profiles were observed across different horizontal locations of the reinforced UHPC bridge deck. This can be attributed to the multiple fine cracks along the horizontal direction, as shown in Figure 3(d). These findings emphasize the importance of crack distribution and width in determining the extent of chloride transport, highlighting the superior crack resistance and corrosion protection capabilities of UHPC compared to traditional reinforced concrete structures.

5.2. Bridge Decks Deterioration

5.2.1. Steel cross-section loss

The corrosion-induced deterioration of the steel reinforcement bars in infrastructure is a critical concern, and assessing the extent of cross-section loss provides valuable insights into the long-term durability of bridge decks. After 30 years of exposure to chloride, the steel reinforcement bars in the reinforced concrete bridge deck exhibited a significant cross-section loss of 12%. This substantial degradation highlights the vulnerability of traditional reinforced concrete structures to corrosion- related damage over extended periods. In contrast, the reinforced UHPC bridge deck demonstrated exceptional resistance to corrosion-induced deterioration. Even after an extended exposure period of 140 years, the steel reinforcement bars in the UHPC deck experienced a comparatively mini- mal cross-section loss of only 5.3%. The differences in cross-sectional loss between the reinforced UHPC bridge deck and the reinforced concrete bridge deck can be attributed to the notable differ- ence in corrosion propagation rates. This outstanding performance underscores the effectiveness of UHPC in mitigating chloride penetration and protecting the embedded steel from corrosion-induced degradation over the prolonged service life.

5.2.2. Concrete and UHPC damage ratings

The material deterioration of concrete and UHPC can be measured using a rating measurement based on the extent of the damaged area [71]:

$$R = A \times 100 + B \times 70 + C \times 40 + D \times 0 \tag{14}$$

A, B , C, and D represent the percentage area of the materials classified as being in sound, fair, poor, and severe damage conditions, respectively. An A rating of 0 indicates worst condition, while a rating of 100 indicates best condition. The damage level of the concrete and UHPC materials can be determined by referring to the reference principal strain contours of the finite elements, as illustrated in Figure 2(b) and (c). For instance, when the principal tensile strain fell within the range of 1 to 2, the concrete and UHPC were considered to be in a sound condition as the materials were still within the elastic range. In the range of 2 to 3, micro-cracking in UHPC began to develop, which was classified as a fair condition. The poor condition and severe damage in UHPC were assumed when the principal tensile strain ranged from 3 to 4 and from 4 to 5, respectively. Conversely, normal strength concrete was assumed to exhibit fair damage in the range of 2 to 3, while the ranges of 3 to 4 and 4 to 5 were associated with poor and severe damage, respectively.

The reinforced concrete bridge deck exhibited a deterioration rating of 79.1% after 30 years of chloride exposure, whereas the reinforced UHPC bridge deck demonstrated a significantly higher rating of 92.8% after 140 years of chloride exposure. The higher damage resistance of UHPC can be attributed to the synergistic effect of the dense material properties and the inherent cracking resistance of UHPC.

5.2.3. Cracking development

To assess the extent of cracking in the bridge decks, the crack density was determined by calcu- lating the ratio of the total cracked area to the measured area. Over time, the cracks in both bridge decks exhibited an increase in length and width, influenced by factors such as traffic load and the expansion of corrosion products following chloride exposure. Figure 4 illustrates the crack density and number of cracks in the bridge decks. The cracking density was calculated as the total length of cracks over the measured area [72]. To measure the crack density, a smaller crack width of 0 .01 mm was chosen for the reinforced UHPC bridge deck, while a width of 0 .05 mm was selected for the rein- forced concrete bridge deck, considering the microcracking characteristics of UHPC. The selection of different crack widths in the modeling process was based on the ability of the computational model to capture the distinct crack behavior of UHPC and normal strength concrete materials. UHPC is known for its unique microstructure and enhanced ductility, which can result in smaller crack widths compared to normal strength concrete. In the modeling of UHPC, a smaller crack width of 0.01 mm was chosen to accurately represent the microcracking characteristics and improved crack resistance of this material. On the other hand, normal strength concrete typically exhibits larger crack widths under similar loading conditions. In the modeling of normal strength concrete, a crack width of 0.05 mm was selected to represent the typical behavior of this material.

As shown in Figure 4, both the reinforced concrete and the reinforced UHPC bridge decks exhibited 13 cracks after 30 years of chloride exposure. However, the cracking density of the reinforced UHPC bridge deck was 43.3% lower than the reinforced concrete bridge deck after 30 years of chloride exposure. This was attributed to the smaller crack depth in UHPC materials. The reinforced UHPC bridge deck reached the same level of cracking density after 140 years of chloride exposure.

These findings establish the significant advantage of using UHPC in bridge deck construction, particularly in chloride-rich environments. The exceptional durability exhibited by the reinforced UHPC bridge deck highlights its potential for long-lasting, sustainable infrastructure solutions. The superior corrosion resistance of UHPC offers the potential for reduced maintenance requirements and life-cycle costs, ensuring the longevity and structural integrity of bridge decks in challenging environmental conditions.

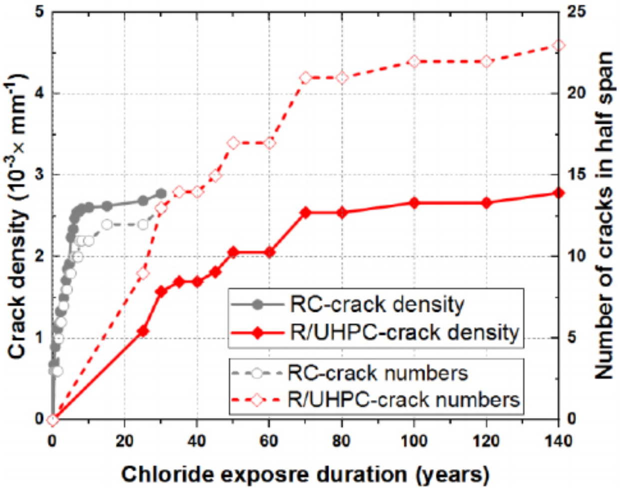

Figure 4: Number of cracks and cracking density over chloride exposure time.

5.3. Initial GHG Emissions and Air Pollutants

Figure 5 illustrates the average GHG emissions and air pollutants associated with the concrete and UHPC bridge decks per m^2, covering the A1 to A5 life cycle stages. These stages include emissions from raw material acquisition, transportation, batching, pumping, and curing. The GHG emissions per m^2 of concrete and UHPC bridge deck were 345 kg and 326 kg CO_{2-eq}, respectively. Despite UHPC generally having higher GHG emissions during construction, due to its greater cement content and the addition of steel fibers [73], the GHG emissions for the UHPC bridge deck, based on the declared functional unit (1 m^2 bridge deck), were 6% lower than those of the concrete bridge deck. This reduction is attributed to the reduced volume of material required per m^2: only 0.125 m^3 of UHPC is needed compared to 0.25 m^3 of concrete.

As shown in Figure 5, a similar trend is observed for air pollutants. NO_X and SO_X, which contribute to acid rain and smog formation, from UHPC bridge deck were 8% and 4% lower than that of the concrete bridge deck, respectively. The combined results of $PM_{2.5}$ and PM_{10}, which are associated with respiratory and cardiovascular health risks, was 16% lower for the UHPC bridge deck. VOC and CO emissions, both contributors to air quality degradation, were both 3% lower for the UHPC bridge deck compared to the concrete bridge deck. These reductions demonstrate the environmental efficiency of UHPC, where its superior mechanical properties enable lower material use, offsetting the higher emissions of its components and resulting in a net improvement in sustainability.

5.4. Life Cycle GHG Emissions

Based on previous deterioration simulation results 5.2, the deck overlay and deck replacement are applied after 15 years and 60 years of service, respectively, for the RC bridge deck, and that minor maintenance is applied every 4 years after initial construction. It is assumed that the UHPC bridge deck is free of major maintenance and deck replacement necessary within the 100-year service life due to its superior performance in deterioration simulation, and its minor maintenance is applied every 4 years after 24 years of service when setting the crack density of 1×10^{-3} mm^{-1} as the threshold. Routine inspections are completed every 2 years for all types of bridge decks.

The UHPC bridge deck demonstrates significantly greater durability, requiring less maintenance and no replacement over an investigated period of 100 years. In contrast, the concrete bridge deck demands frequent maintenance, which adds to its environmental burden over its life cycle. Consequently, the life cycle GHG emissions of the UHPC bridge deck are substantially lower than those of the concrete bridge deck. As shown in Figure 6, the total GHG emissions from raw material acquisition (A1) to disposal and crushing (C3) are 2595 kg CO_{2-eq} per m^2 for the concrete bridge deck and 952 kg CO_{2-eq} per m^2 for the UHPC bridge deck, respectively. The GHG emissions from the maintenance stage (B1-B3) accounted for 86% and 65% of the total emissions for the concrete and UHPC bridges, respectively. A similar trend was observed for air pollutants. NO_X emissions during the maintenance stage constituted 86% and 65% of the total emissions for the concrete and UHPC bridges, respectively. SO_X emissions from maintenance were 87% and 65% of the total for the concrete and UHPC bridges, respectively. Particulate matter, including $PM_{2.5}$ and PM_{10}, as well as (VOC_s), also accounted for 87% and 65% of the total emissions for the concrete and UHPC bridges, respectively. Similarly, CO emissions from the maintenance stage contributed 87% and 65% of the total emissions for the concrete and UHPC bridges, respectively. These results emphasize the significant environmental burden of the maintenance stage, particularly for the concrete bridge.

5.5. Life-cycle Costs

Figure 7 illustrates the life cycle costs of the concrete and UHPC bridge decks over a 100-year service life, including material, maintenance, construction, and social costs. At year 60, the to- tal costs (comprising life cycle cost net present value, LCCNVP, and social costs) of the concrete bridge ($14.8 million) surpassed those of the UHPC bridge ($13 .5 million). The lower total costs of the UHPC bridge after 60 years indicate its economic advantage, driven by reduced mainte- nance requirements, longer service life, and lower associated social costs. This demonstrates that, despite potentially higher initial costs, the UHPC bridge provides significant long-term cost sav- ings and sustainability benefits. To assess the sensitivity of how initial material costs influence the total costs of bridge decks, various UHPC material costs ($/m3) were considered. Specifically, UHPC material costs ($/m3) were evaluated from two to six times the unit material cost of conven- tional concrete. Accordingly, the initial unit UHPC deck costs examined were $1000/m2 , $1500/m2 , $2000/m2 ,$2500/m2 , $3000/m2 . The resulting initial and total costs are summarized in Table 4. When the material cost of UHPC reaches five times that of concrete, the total cost of an UHPC bridge deck consistently exceeds that of a concrete bridge deck.

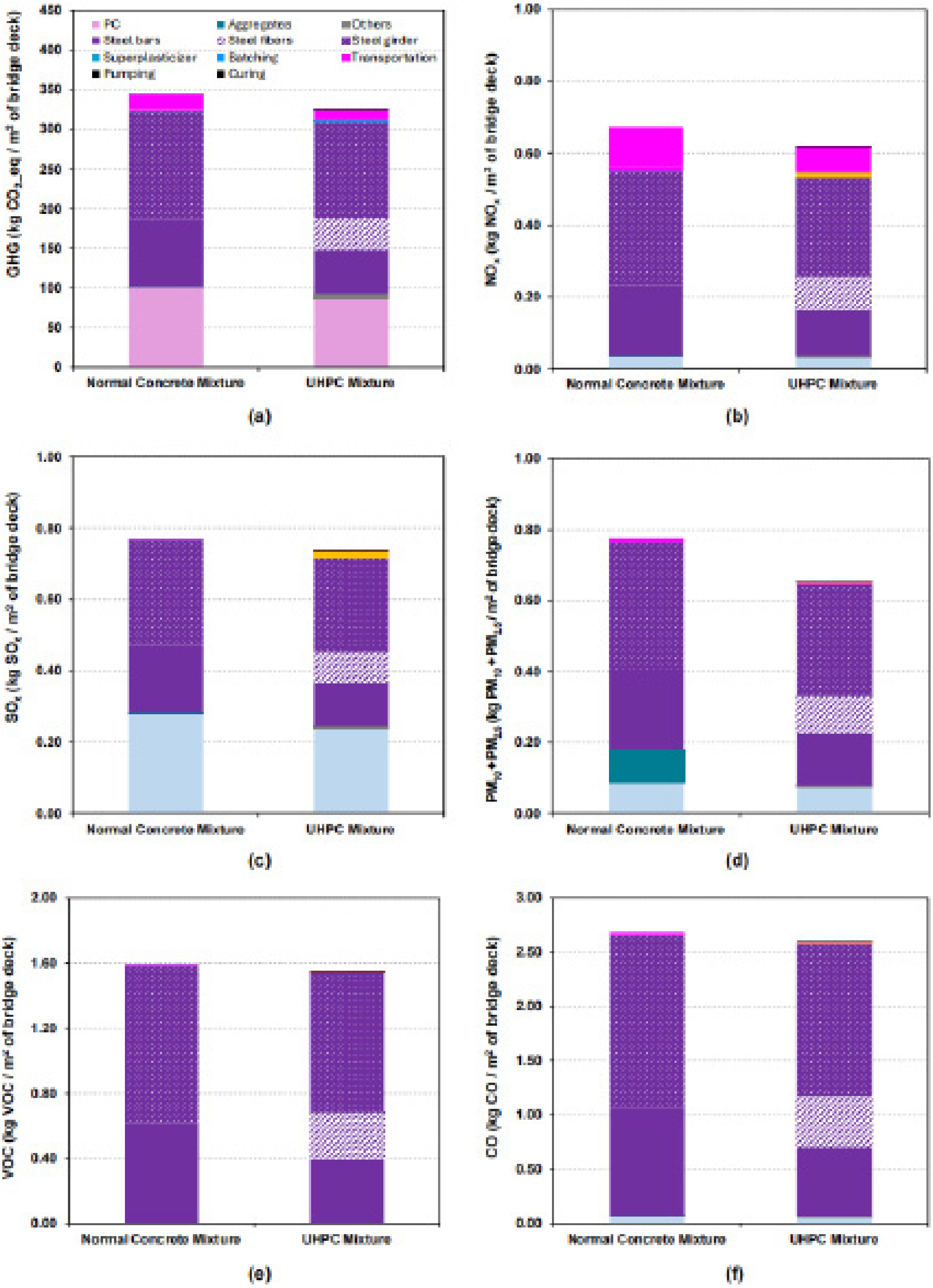

(a) (b)

(c) (d)

(e) (f)

Figure 5: Emissions from A1-A5: (a) GHG emissions; (b) NO_X emission; (c) SO_X emission; (d) $PM_{2.5}$ and PM_{10} emissions; (e) VOC_s emission; (f) CO emission.

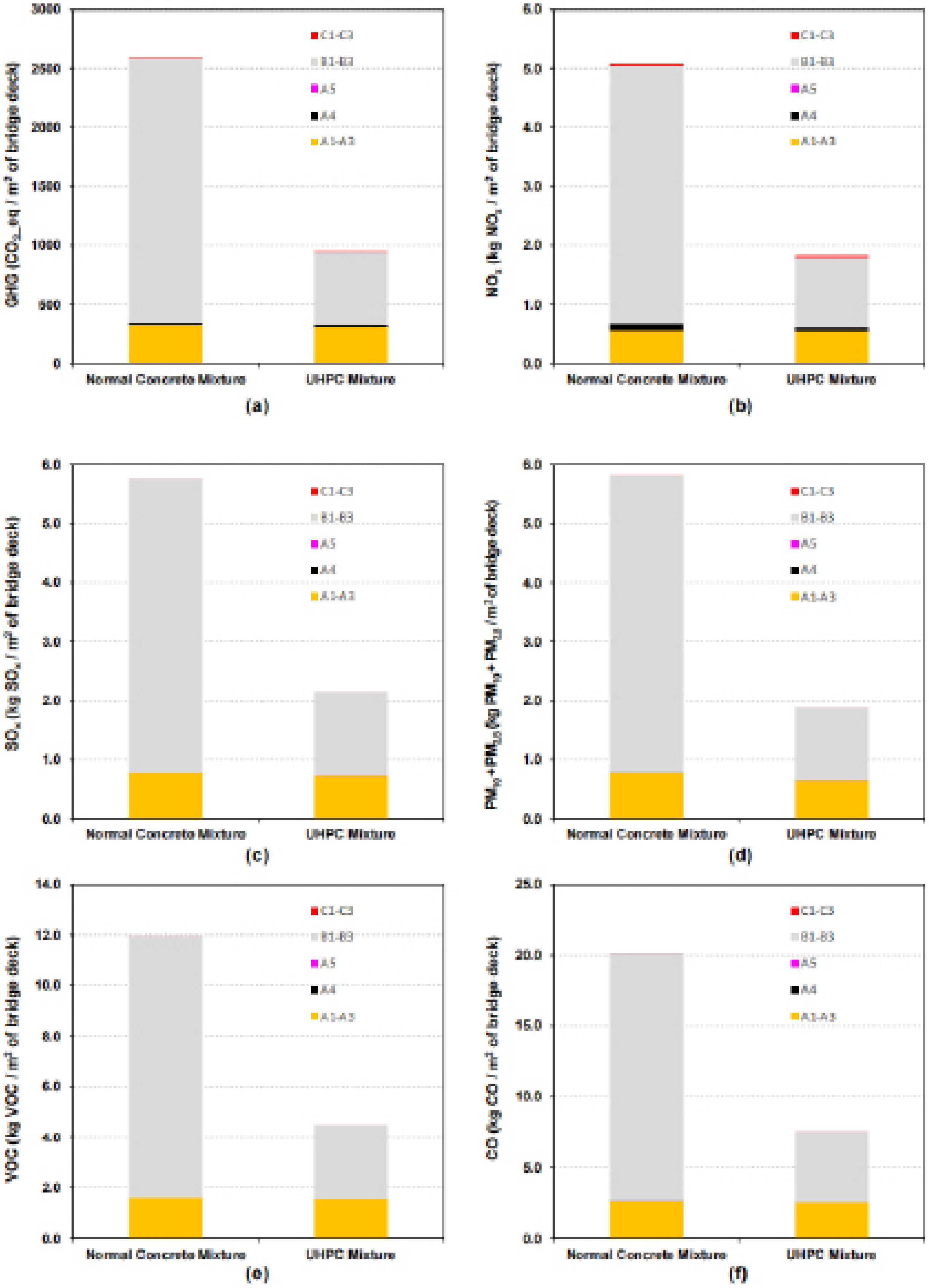

(a) (b) (c) (d) (e) (f)

Figure 6: Life Cycle Emissions from A1-C3: (a) GHG emissions; (b) NO_x emission; (c) SO_x emission; (d) $PM_{2.5}$ and PM_{10} emissions; (e) VOC_s emission; (f) CO emission

Table 4: Cost Comparison Between Concrete and UHPC Bridge Decks

	Concrete	UHPC				
Initial Material Cost ($/m^3)	4,000	8,000	12,000	16,000	20,000	24,000
Initial Unit Deck Cost ($/m^2)	1000	1000	1500	2000	2500	3000
Total Cost at Year 60 (million $/bridge deck)	14.8	6.9	10.4	13.5	16.8	20.1
Total Cost at Year 100 (million $/bridge deck)	16.3	7.4	10.8	14.1	17.5	20.9

The social costs associated with the concrete and UHPC bridge over 100 years of service life were $1.85 million and $0.68 million, respectively. According to the Intergovernmental Panel on Climate Change (IPCC), while applying SCC has been effective in reducing GHG emissions, achieving net- zero GHG emissions by 2050 will require significantly higher carbon prices [74]. The SCC value of 116 USD per ton CO_2 used in this study is a conservative estimate [75]. There are studies suggest that the social cost of carbon could be as high as 1000 USD per ton CO_2 [76]. When higher SCC were to applied, the UHPC bridge showed greater benefits due to the lower life-cycle GHG emissions compared to that of the concrete bridge. If a lower discount rate (2%) were used, the social costs of the concrete and UHPC bridge would increase to $2 .85 million and $1.04 million, respectively. These values highlight the potential for substantial variability in social cost estimates and underscore the importance of adopting an appropriate carbon price to drive meaningful emissions reductions.

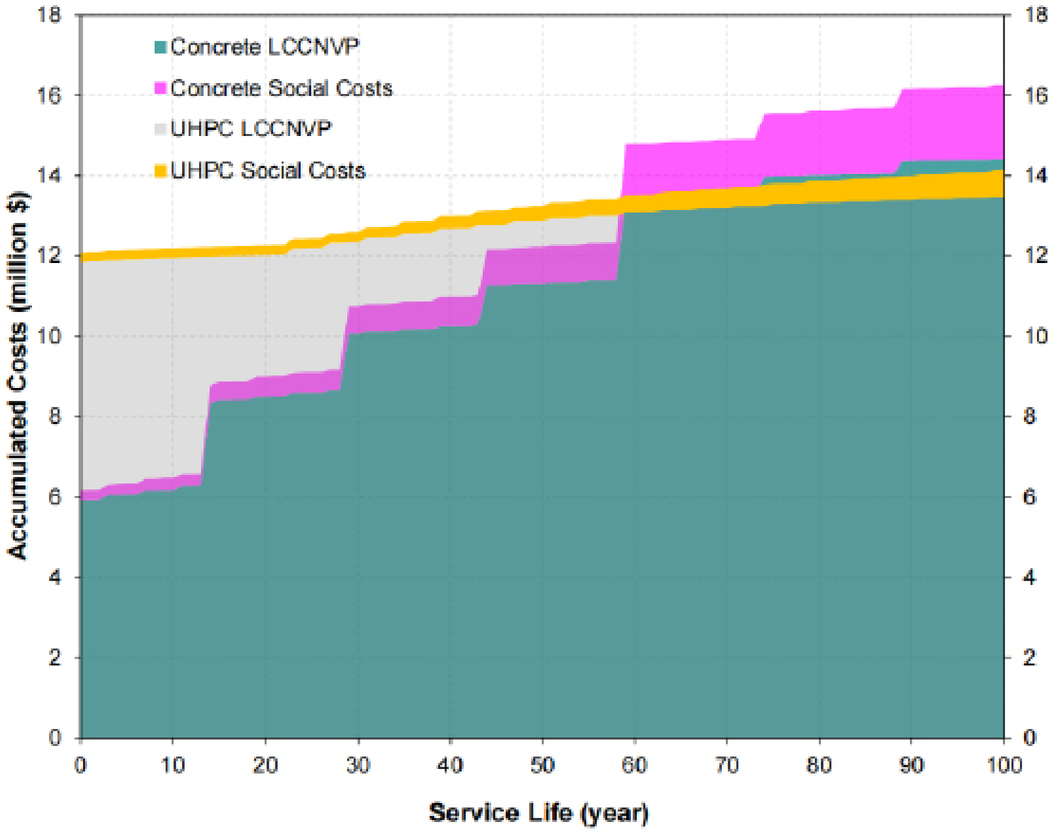

Figure 7: Life cycle GHG emission

6. Conclusions

This study compared reinforced concrete and ultra-high-performance concrete (UHPC) bridge decks over a 100-year service life, examining structural durability, environmental impacts, and life cycle costs under identical temperature fluctuations and exposure to de-icing materials. Results indicate that UHPC bridge decks offer superior performance across all evaluated metrics. The reinforced UHPC bridge deck demonstrated significantly slower structural deterioration, with reinforcing bar cross-section loss of only 5.3% after 140 years, compared to 12.0% for the reinforced concrete deck after just 30 years of exposure to chloride ingress. Similarly, UHPC decks exhibited higher resistance to damage and cracking, as evidenced by deterioration ratings of 92.8% and lower cracking densities even after extended service.

Environmental analysis revealed that the life cycle GHG emissions of the UHPC bridge deck were significantly lower, totaling 952 kg $CO_{2\text{-eq}}$ per m^2 compared to 2595 kg $CO_{2\text{-eq}}$ per m^2 for the concrete deck. This reduction was largely attributed to the UHPC's superior durability, which reduced maintenance-related emissions from stages B1 to B3, contributing 65% of total emissions for the UHPC bridge deck versus 86% for the concrete bridge deck. Comparable trends were observed for air pollutants, including nitrogen oxides (NO_x), sulfur oxides (SO_x), volatile organic compounds (VOC_s), particular matter less than 10 μm (PM_{10}), and particulate matter less than 2.5 μm ($PM_{2.5}$), and carbon monoxide (CO). Ongoing research into lower-carbon UHPC systems, if successful, will result in even more reductions in the life-cycle carbon emissions [77, 78].

Economically, UHPC bridge decks demonstrated long-term cost advantages despite higher initial material costs. By year 60, the total costs of the reinforced concrete bridge deck, including net present value and social costs, exceeded those of UHPC decks ($14.8 million vs. $13.5 million). The substantial improvement in service life performance lead to cost savings in maintenance and repair expenses over time. Additionally, despite the potential higher initial construction costs associated with UHPC, the reduced bridge deck cross-section of the reinforced UHPC bridge deck can help offset some of these upfront expenses.

The findings of this study emphasize the potential of UHPC materials as a sustainable and cost-effective alternative to conventional concrete materials. By minimizing environmental impacts, reducing life cycle costs, and extending service life, UHPC provides a compelling solution for ad- vancing sustainable infrastructure in the face of increasing environmental and economic challenges.

Acknowledgments

This material is based upon work supported by the New Jersey Department of Transportation through Contract ID 19-60155. Any opinions, findings, and conclusions or recommendations ex- pressed in this material are those of the author(s) and do not necessarily reflect the views of the New Jersey Department of Transportation (NJDOT). The authors gratefully acknowledge financial support of NJDOT and the John A. Reif, Jr. Department of Civil and Environmental Engineering at New Jersey Institute of Technology.

References

M. C. Summaries, et al., Mineral commodity summaries, US Geological Survey: Reston, VA, USA 200 (2021).

C. IEA, et al., Technology roadmap low-carbon transition in the cement industry, France/WBCSD, Geneva, Switzerland. IEA, Paris (2018).

S. A. Miller, A. Horvath, P. J. Monteiro, Readily implementable techniques can cut annual co2 emissions from the production of concrete by over 20%, Environmental Research Letters 11 (2016) 074029.

J. A. Olsson, S. A. Miller, M. G. Alexander, Near-term pathways for decarbonizing global concrete production, Nature Communications 14 (2023) 4574.

J. Fan, M. Adams, M. Bandelt, Service life prediction of RC and UHPC bridge decks exposed to regional environments, in: International Interactive Symposium on Ultra-High Performance Concrete, volume 3, Iowa State University Digital Press, 2023, p. 29.

D.-Y. Yoo, S.-T. Kang, Y.-S. Yoon, Enhancing the flexural performance of ultra-high-performance concrete using long steel fibers, Composite Structures 147 (2016) 220–230.

A. M. Tahwia, A. Essam, B. A. Tayeh, M. Abd Elrahman, Enhancing sustainability of ultra-high performance concrete utilizing high-volume waste glass powder, Case Studies in Construction Materials 17 (2022) e01648.

X. Wang, D. Wu, J. Zhang, R. Yu, D. Hou, Z. Shui, Design of sustainable ultra-high performance concrete: A review, Construction and Building Materials 307 (2021) 124643.

H. Kim, T. Koh, S. Pyo, Enhancing flowability and sustainability of ultra high performance concrete incorporating high replacement levels of industrial slags, Construction and Building Materials 123 (2016) 153–160.

Z. B. Haber, I. De la Varga, B. A. Graybeal, B. Nakashoji, R. El-Helou, Properties and behavior of UHPC-class materials, Technical Report, United States. Federal Highway Administration. Office of Infrastructure . . . , 2018.

Y. Shao, C.-C. Hung, S. L. Billington, Gradual crushing of steel reinforced HPFRCC beams: Experiments and simulations, Journal of Structural Engineering 147 (2021) 04021114.

V. Perry, D. Zakariasen, First use of ultra-high performance concrete for an innovative train station canopy, Concrete Technology Today 25 (2004) 1–2.

J. Fan, M. Adams, M. Bandelt, Multi-physics simulation of steel corrosion in reinforced UHPC beams under coupled sustained loading and chloride attack, in: Computational Modelling of Concrete and Concrete Structures, CRC Press, 2022, pp. 590–595.

C.-C. Hung, S. El-Tawil, S.-H. Chao, A review of developments and challenges for uhpc in structural engineering: Behavior, analysis, and design, Journal of Structural Engineering 147 (2021) 03121001.

B. Graybeal, E. Br¨uhwiler, B.-S. Kim, F. Toutlemonde, Y. L. Voo, A. Zaghi, International perspective on UHPC in bridge engineering, Journal of Bridge Engineering 25 (2020) 04020094.

C. Shi, Z. Wu, J. Xiao, D. Wang, Z. Huang, Z. Fang, A review on ultra high performance concrete: Part i. raw materials and mixture design, Construction and Building Materials 101 (2015) 741-751.

P. Aghdasi, A. E. Heid, S.-H. Chao, Developing ultra-high-performance fiber-reinforced concrete for large-scale structural applications., ACI Materials Journal 113 (2016).

C.-C. Hung, H.-H. Hung, Potential of sodium sulfate solution for promoting the crack-healing performance for strain-hardening cementitious composites, Cement and Concrete Composites 106 (2020) 103461.

Y. Shao, S. Billington, Utilizing full UHPC compressive strength in steel reinforced UHPC beams, in: International Interactive Symposium on Ultra-High Performance Concrete, volume 2, Iowa State University Digital Press, 2019, pp. 1-9.

Y. Shao, S. L. Billington, Impact of UHPC tensile behavior on steel reinforced uhpc flexural behavior, Journal of Structural Engineering 148 (2022) 04021244.

M. Ye, L. Li, H. Li, C. Zhou, Shear behavior of joints in precast UHPC segmental bridges under direct shear loading, Construction and Building Materials 357 (2022) 129212.

M. Ye, L. Li, D.-Y. Yoo, H. Li, X. Shao, C. Zhou, Mechanistic understanding of precast UHPC segmental beams with external tendons and epoxy joints subject to combined bending and shear, Engineering Structures 280 (2023) 115698.

B. Graybeal, J. Tanesi, Durability of an ultrahigh-performance concrete, Journal of materials in civil engineering 19 (2007) 848-854.

X.-g. Tang, Y.-j. Xie, G.-c. Long, Experimental study on performance of imitative rpc for sulphate leaching, Journal of Asian Ceramic Societies 4 (2016) 143-148.

N. A. Soliman, A. Tagnit-Hamou, Using glass sand as an alternative for quartz sand in uhpc, Construction and Building Materials 145 (2017) 243-252.

M.-G. Lee, Y.-C. Wang, C.-T. Chiu, A preliminary study of reactive powder concrete as a new repair material, Construction and building materials 21 (2007) 182-189.

Y. Shi, G. Long, C. Ma, Y. Xie, J. He, Design and preparation of ultra-high performance concrete with low environmental impact, Journal of Cleaner Production 214 (2019) 633-643.

C. D. Joe, M. Moustafa, Cost and ecological feasibility of using UHPC in bridge piers, in: International Interactive Symposium on Ultra-High Performance Concrete, volume 1, Iowa State University Digital Press, 2016, pp. 1-8.

H. Sameer, V. Weber, C. Mostert, S. Bringezu, E. Fehling, A. Wetzel, Environmental assessment of ultra-high-performance concrete using carbon, material, and water footprint, Materials 12 (2019) 851.

T. Stengel, P. Schießl, Life cycle assessment (lca) of ultra high performance concrete (UHPC) structures, in: Eco-efficient construction and building materials, Elsevier, 2014, pp. 528-564.

J. M´arquez, D. Jauregui, B. Weldon, C. Newtson, Potential environmental impact of using ultra-high performance concrete in simple, two and three-span continuous prestressed concrete bridges, in: Bridge Maintenance, Safety, Management, Life-Cycle Sustainability and Innovations, CRC Press, 2021, pp. 4076-4083.

Y. Dong, Performance assessment and design of ultra-high performance concrete (UHPC) structures incorporating life-cycle cost and environmental impacts, Construction and Building Materials 167 (2018) 414-425.

J. Fan, Y. Shao, M. J. Bandelt, M. P. Adams, C. P. Ostertag, Sustainable reinforced concrete design: The role of ultra-high performance concrete (uhpc) in life-cycle structural performance and environmental impacts, Engineering Structures 316 (2024) 118585.

J. Fan, S. M. Shirkhorshidi, M. P. Adams, M. J. Bandelt, Predicting corrosion in reinforced UHPC members through time-dependent multi-physics numerical simulation, Construction and Building Materials 340 (2022) 127805.

J. Crank, The mathematics of diffusion, Oxford university press, London, UK, 1979.

A. Djerbi, S. Bonnet, A. Khelidj, V. Baroghel-Bouny, Influence of traversing crack on chloride diffusion into concrete, Cement and Concrete Research 38 (2008) 877-883.

A. V. Saetta, R. V. Scotta, R. V. Vitaliani, Analysis of chloride diffusion into partially saturated concrete, Materials Journal 90 (1993) 441-451.

H.-W. Reinhardt, M. Jooss, Permeability and self-healing of cracked concrete as a function of temperature and crack width, Cement and Concrete Research 33 (2003) 981-985.

C. Cao, 3D simulation of localized steel corrosion in chloride contaminated reinforced concrete, Construction and Building Materials 72 (2014) 434-443.

J. Chen, W. Zhang, X. Gu, Modeling time-dependent circumferential non-uniform corrosion of steel bars in concrete considering corrosion-induced cracking effects, Engineering Structures 201 (2019) 109766.

J. P. Broomfield, Corrosion of steel in concrete: understanding, investigation and repair, Taylor & Francis, New York, NY, USA, 2007.

Y. Zhao, W. Jin, Steel corrosion-induced concrete cracking, Butterworth-Heinemann, Kidlington, Oxford, UK, 2016.

J. Warkus, M. Raupach, J. Gulikers, Numerical modelling of corrosion–theoretical backgrounds, Materials and Corrosion 57 (2006) 614–617.

S. Kranc, A. A. Sag¨u´es, Detailed modeling of corrosion macrocells on steel reinforcing in concrete, Corrosion Science 43 (2001) 1355–1372.

H. B¨ohni, Corrosion in reinforced concrete structures, CRC Press LLC, Boca Raton, Florida, USA, 2005.

R. W. Revie, Corrosion and corrosion control: an introduction to corrosion science and engineering, John Wiley & Sons, Hoboken, New Jersey, USA, 2008.

E. Bardal, Corrosion and protection, Springer, London, UK, 2003.

DIANA, DIANA User's Manual, Delft, The Netherlands, 2022.

COMSOL, COMSOL Multiphysics Reference Manual, Burlington, MA, USA, 2018.

ACI Committee 224, Control of cracking in concrete structures, Technical Report, American Concrete Institute, 2001.

M. M. Cheung, J. Zhao, Y. B. Chan, Service life prediction of rc bridge structures exposed to chloride environments, Journal of Bridge Engineering 14 (2009) 164–178.

Climate-Data.org, Climate: New brunswick - climate graph, temperature graph, climate table, https://en.climate-data.org/north-america/united-states-of-america/new-jersey/new-brunswick-1729/, ???? Accessed: 2022-12-17.

P. Feenstra, J. Rots, A. Arnesen, J. Teigen, K. Hoiseth, A 3D constitutive model for concrete based on a co-rotational concept, in: Computational Modelling of Concrete Structures. Proceedings of the Euro-C 1998 Conference on Computational Modelling of Concrete Structures, Badgastein, Austria, 31 March-3 April, Brookfield, 1998, p. 13.

M. J. Bandelt, S. L. Billington, Impact of reinforcement ratio and loading type on the deformation capacity of high-performance fiber-reinforced cementitious composites reinforced with mild steel, Journal of Structural Engineering 142 (2016) 04016084.

A. Rafiee, Computer modeling and investigation on the steel corrosion in cracked ultra high performance concrete, Ph.d. dissertation, Kassel University, Kassel, Germany, 2012.

J. Fan, M. Adams, M. J. Bandelt, Finite element simulation of mechanical-electrochemical coupling effects of steel corrosion in ecc structures, in: 2021 fib Symposium of Concrete Structures: New Trends for Eco-Efficiency and Performance, fib. The International Federation for Structural Concrete, 2021, pp. 371–380.

O. B. Isgor, A. G. Razaqpur, Modelling steel corrosion in concrete structures, Materials and Structures 39 (2006) 291–302.

Y. Cao, C. Gehlen, U. Angst, L. Wang, Z. Wang, Y. Yao, Critical chloride content in reinforced concrete—an updated review considering chinese experience, Cement and Concrete Research 117 (2019) 58–68.

A. Michel, B. J. Pease, A. Peterov´a, M. R. Geiker, H. Stang, A. E. A. Thybo, Penetration of corrosion products and corrosion-induced cracking in reinforced cementitious materials: Experimental investigations and numerical simulations, Cement and Concrete Composites 47 (2014) 75–86.

C. Cao, M. M. Cheung, B. Y. Chan, Modelling of interaction between corrosion-induced concrete cover crack and steel corrosion rate, Corrosion Science 69 (2013) 97–109.

C. Lu, W. Jin, R. Liu, Reinforcement corrosion-induced cover cracking and its time prediction for reinforced concrete structures, Corrosion Science 53 (2011) 1337–1347.

J. G. Canadell, P. M. Monteiro, M. H. Costa, L. Cotrim da Cunha, P. M. Cox, A. V. Eliseev, S. Henson, M. Ishii, S. Jaccard, C. Koven, et al., Intergovernmental panel on climate change (ipcc). global carbon and other biogeochemical cycles and feedbacks, in: Climate change 2021: The physical science basis. Contribution of working group I to the sixth assessment report of the intergovernmental panel on climate change, Cambridge University Press, 2023, pp. 673–816.

A. Kim, P. R. Cunningham, K. Kamau-Devers, S. A. Miller, Openconcrete: a tool for estimating the environmental impacts from concrete production, Environmental Research: Infrastructure and Sustainability 2 (2022) 041001.

M. J. Nahlik, A. T. Kaehr, M. V. Chester, A. Horvath, M. N. Taptich, Goods movement life cycle assessment for greenhouse gas reduction goals, Journal of Industrial Ecology 20 (2016) 317-328.

M. Marceau, M. A. Nisbet, M. G. Van Geem, Life cycle inventory of portland cement concrete, Portland Cement Association, 2007.

Interagency Working Group on Social Cost of Greenhouse Gases, United States Government, Technical Support Document: Social Cost of Carbon, Methane, and Nitrous Oxide: Interim Estimates under Executive Order 13990, Technical Report, United States Government, 2021.

D. M. Frangopol, Y. Dong, S. Sabatino, Bridge life-cycle performance and cost: analysis, prediction, optimisation and decision-making, in: Structures and Infrastructure Systems, Routledge, 2019, pp. 66-

84.
D. Cusson, Z. Lounis, L. Daigle, Benefits of internal curing on service life and life-cycle cost of high-performance concrete bridge decks-a case study, Cement and Concrete Composites 32 (2010) 339-350.
T. Ngo, Application of UHPC in Long Span Bridge Design, Master thesis, Kassel University, Delft,Netherlands, 2016.
J. Cao, X. Shao, L. Deng, Y. Gan, Static and fatigue behavior of short-headed studs embedded in a thin ultrahigh-performance concrete layer, Journal of Bridge Engineering 22 (2017) 04017005.
P. Szary, A. M. Roda, et al., Bridge resource program., Technical Report, Rutgers University. Center for Advanced Infrastructure & Transportation, 2013.
T. R. Schmitt, D. Darwin, Effect of material properties on cracking in bridge decks, Journal of Bridge Engineering 4 (1999) 8-13.
C. Schultz, P. R. Cunningham, J. Fan, S. A. Miller, Balancing the mechanical performance and environmental sustainability of fiber reinforced concrete, Journal of Materials in Civil Engineering TBD (2025).
Intergovernmental Panel on Climate Change, Climate Change 2022 - Mitigation of Climate Change: Working Group III Contribution to the Sixth Assessment Report of the Intergovernmental Panel on Climate Change, Cambridge University Press, 2022. doi:10.1017/9781009157926.013.
P. Colligan, E. Van Roijen, S. Kane, F. Moore, S. A. Miller, The unaccounted-for climate costs of materials, Environmental Research Letters 19 (2024) 114063.
K. Rennert, F. Errickson, B. C. Prest, L. Rennels, R. G. Newell, W. Pizer, C. Kingdon, J. Wingenroth, R. Cooke, B. Parthum, et al., Comprehensive evidence implies a higher social cost of co2, Nature 610 (2022) 687-692.
K. Cui, K. Liang, J. Chang, D. Lau, Investigation of the macro performance, mechanism, and durability of multiscale steel fiber reinforced low-carbon ecological uhpc, Construction and Building Materials 327 (2022) 126921.
X. Zhang, Z. Wu, J. Xie, X. Hu, C. Shi, Trends toward lower-carbon ultra-high performance concrete (uhpc)-a review, Construction and Building Materials 420 (2024) 135602.

The Mechanical Properties of Ultra-High Performance Concrete

Farzad Rezazadeh P.[1,*] , Amin Abrishambaf[2], Axel Dürrbaum[3] , Gregor Zimmermannb[4] ,Andreas Kroll [5]

[1] Department of Measurement and Control, University of Kassel, Mönchebergstr. 7, Kassel, 34125, Hessen, Germany

[2] German Technologies & Engineering Concepts - G. tecz Engineering GmbH, Kassel, 34123, Hessen, Germany

[3] Department of Measurement and Control, University of Kassel, Mönchebergstr. 7, Kassel, 34125, Hessen, Germany

[4] German Technologies & Engineering Concepts - G. tecz Engineering GmbH, Kassel, 34123, Hessen, Germany

[5] Department of Measurement and Control, University of Kassel, Mönchebergstr. 7, Kassel, 34125, Hessen, Germany

***Corresponding author, E-mail: farzad .rezazadeh@mrt .uni-kassel .de**

Abstract

Ultra-High Performance Concrete (UHPC) surpasses conventional concrete in performance. However, producing UHPC with consistent mechanical properties, even with an identical recipe, remains challenging. The quality of UHPC can be significantly influenced by material quality, environmental factors, and human intervention during large-scale production. This study, for the first time, takes a holistic view of the UHPC manufacturing process to investigate the impact of material quality, environmental conditions, measurement errors, and mixing and curing conditions on the final mechanical properties. This comprehensive approach to the UHPC manufacturing process presents two challenges. First, there is no publicly available dataset for this research. Therefore, 150 experiments were conducted, measuring both Compressive and Flexural Strength after 28 days of curing, resulting in two experimental datasets for this study. Second, this wide view increases data dimensionality and, coupled with the high cost of UHPC experiments, yields sparse data. Traditional evolutionary algorithms, while effective in feature selection, struggle in high-dimensional, small-sample data. To address this, an Informed Non- dominated Sorting Genetic Algorithm II (I-NSGA-II) is developed in this study, incorporating domain-specific knowledge to enhance prediction accuracy and solution stability. Comparative evaluations using different machine learning algorithms on the two experimental datasets and a dataset generated by a test function demonstrated the significant superiority of I-NSGA-II over the classic NSGA-II. Finally, the significance of each studied parameter on the mechanical behavior of UHPC is discussed.

Keywords: Ultra-High Performance Concrete; Concrete Manufacturing Process; Ensemble-based Outlier Detection; Multiobjective Feature Selection; Data-Driven Modeling

1. Introduction

Concrete is the second-most consumed resource globally, after water, and cement production, as the cornerstone of any type of concrete, accounts for around 7 % of CO_2 emissions worldwide [1].

Ultra-high performance concrete (UHPC) is an advanced cement-based composite known for its exceptional mechanical strength and durability. It typically contains a high volume of short steel fibers (around 2 % by volume) distributed within a dense matrix with a low water-to-binder ratio, often incorporating silica fume. This composition allows UHPC to exhibit uniaxial tensile hardening behavior, leading to stable microcracks and excellent transport properties even under demanding conditions. These characteristics make UHPC ideal for innovative applications such as bridge construction, structural strengthening, and waterproofing. However, the high cement and silica fume content contribute to increased production costs and a significant CO_2 footprint [2].

Additionally, the production process for UHPC is highly sensitive [3–6], with minor deviations from the recipe or changes in environmental conditions drastically impacting consistency and mechanical behavior, leading to increased waste. To address these issues, the construction industry requires an advanced support system capable of predicting UHPC properties in real time. Such a system would enhance quality control during production, reduce waste, improve product quality, and achieve cost savings.

To date, investigations into the UHPC manufacturing process have typically focused on individual factors rather than a comprehensive analysis of all relevant variables. Consequently, there are no published datasets that encompass the full spectrum of variables affecting UHPC production and quality. In this study, we conduct a systematic investigation of variations arising from all relevant factors around a reference UHPC production condition (Figure1). We examine the impact of raw material properties (such as impurities and particle size distribution), dosing system errors, mixing duration and speed, and environmental conditions (affecting both raw materials and specimen curing) on UHPC quality. Modeling the UHPC production process holistically presents significant challenges due to the complex physical and chemical subprocesses involved. Generating data for a single experimental point requires 28 days, making the process extremely time-consuming and costly. To address this, a two-phase experimental design was implemented in this study to generate 150 data points, optimally covering the input space. However, the high dimensionality and small sample size of the data further complicate modeling efforts. Standard methods, such as sequential feature selection and recursive feature elimination, often struggle to identify nuanced patterns in sparse data, frequently missing critical relationships and becoming trapped in local minima [7,8]. While evolutionary multiobjective feature selection methods can outperform grid search-based approaches, they are less effective when applied to high-dimensional, small-sized datasets.

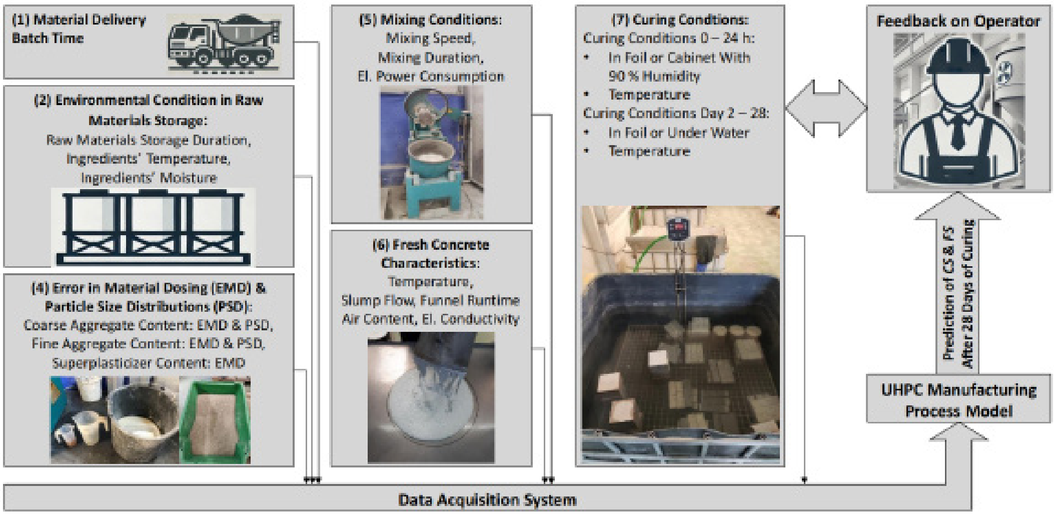

Figure 1: Modeling of Reproducible UHPC with Consistent Properties[1]

---

[1] Ultra-High Performance Concrete Manufacturing Process: Production and testing processes, influencing factors, and key considerations regarding the impact of material quality, measurement errors, and environmental conditions on final UHPC mechanical quality [6]. (El.: Electrical, CS: Compressive Strength, FS: Flexural Strength)

To address these challenges, this paper focuses on dimensionality reduction in multiple steps. By injecting domain knowledge into the classic Non-dominated Sorting Genetic Algorithm II (NSGA-II), prediction results and solution stability are enhanced. The proposed Informed NSGA-II (I-NSGA-II) in this study addresses high dimensionality issues with small sample sizes for evolutionary multiobjective feature selection.

To the authors' knowledge, this is the first study to provide a holistic view of the UHPC manufacturing process by investigating the causal effects of various variables on final product quality consistency from an application perspective. Additionally, this study uniquely addresses evolutionary multiobjective feature selection by incorporating prior knowledge into the Non-dominated Sorting Genetic Algorithm II, thereby enhancing prediction performance and solution stability for high-dimensional datasets with small sample sizes. The contributions of this paper are summarized as follows:

- Present a holistic approach to the UHPC manufacturing process.
- Investigate the impact of material quality, environmental conditions, measurement errors, and mixing and curing conditions on reproducibility of UHPC with consistent mechanical properties, as well as the relation of fresh UHPC characteristics with these mechanical properties.
- Introduce a Human-in-the-Loop Ensemble-based Outlier Detection Method, informed by expert insights, to enhance data quality.

2. Related Work

2.1. Machine Learning Applications in Predicting Concrete Mechanical Properties

The task of predicting concrete compressive strength (CS), particularly its 28-day CS, is typically addressed by two major approaches: traditional empirical models and modern machine learning techniques [11]. One of the earliest empirical methods, known as Abram's Law [12], is:

$$CS = \frac{a_0}{a_1^{w/c}}, \tag{1}$$

where a0 and a1 are empirical constants, and w and c represent the quantities of water and cement, respectively. An advancement of this method is multiple linear regression [13]:

$$CS = a_0 + a_1 \frac{W}{C} + a_2 CA + a_3 FA + C, \tag{2}$$

which incorporates the water-to-cement ratio w/c, amounts of coarse (CA) and fine aggregate (FA), and cement quantity (C). However, these models do not consider all the complex steps in the concrete production process. This makes it hard to accurately predict the properties of advanced concrete types like UHPC [14].

The significance of mix proportion parameters is emphasized by Ozbay et al. [15], yet environmental variables and curing conditions are overlooked. Farzampour [16] highlights certain mix proportion parameters while acknowledging environmental factors during curing; however, a comprehensive analysis of these aspects is lacking, and an in- depth examination of curing conditions is not conducted. The necessity of longer mixing times to achieve optimal homogeneity in UHPC, compared to CC and HPC, is pointed out by Safranek [17], which also cautions against high mixing speeds due to potential thermal effects.

The initial challenge in adopting machine learning techniques for concrete research is the scarcity of comprehensive and reliable datasets. The datasets on Compressive Strength [18] and Slump Flow Test [19], compiled by Yeh from various research sources, are widely used. Despite their extensive utilization [13, 20–28], these datasets exhibit significant shortcomings: limited coverage of input factors across the concrete production process and potential inconsistencies in material quality and production conditions, including mixing and curing processes. These issues compromise the utility of the datasets for both academic and practical applications [6,29].

Nguyen et al. [30] employed the XGBoost model to forecast the CS of UHPC using a dataset of 931 UHPC mix formulations, compiled from laboratory experiments and existing literature, encompassing 17 input variables. The study aimed to enhance precision in UHPC compressive strength estimates and facilitate the development of new UHPC mixtures, reducing both time and costs associated with their creation. Despite these ambitious objectives, Nguyen et al.'s methodology presents notable limitations. The amalgamation of data from varied sources without stringent standardization introduces biases, potentially skewing results. Moreover, the study's exclusive reliance on the XGBoost algorithm and intensive focus on hyperparameter tuning at the expense of feature selection restricts the research scope. Such a narrowed focus overlooks potential insights from a broader spectrum of algorithms and a comprehensive evaluation of input features' relevance. Additionally, the absence of possible uncertainties in material quality, material dosing, mixing, and curing conditions in the analysis undermines the model's practical applicability, given their critical role in determining UHPC's compressive strength.

Designing a pipeline for the concrete production process with sparse data is a topic that has been rarely researched [31–33]. The recently proposed pipeline for modeling concrete production and optimizing concrete mixtures [33] overlooks key aspects of managing high-dimensional datasets, especially the complexities of small datasets with high dimensionality and a comprehensive understanding of the concrete production process, including material quality and curing time. Its approach to data generation – limited to compiling data from various sources – risks introducing redundancy. Moreover, the reliance on a narrow set of tree-based machine learning algorithms may not adequately capture the complexity of the data. The study also lacks crucial preprocessing steps, such as outlier detection and appropriate handling of missing values, opting instead for simple mean imputation. Furthermore, its simplistic training- testing strategy, which relies on a single data split, fails to ensure model reliability across various data partitions.

Despite advancements in predicting concrete strength, significant gaps remain, underscoring the challenges in capturing the full spectrum of variables that influence end-product quality [34]. These gaps encompass limited data coverage, including material quality, measurement errors, and mixing and curing conditions, which lack a holistic view of the production process. These issues can cause discrepancies inUHPC's final quality even with identical recipes [35]. Other challenges include systematic data generation, ineffective feature selection methods struggling with the high- dimensional nature of the data, inadequate training-test strategies [36–45], and a narrow range of explored algorithms [14,46–53].

Addressing these challenges, this work takes a holistic view of the UHPC manufacturing process to investigate the effect of material quality, uncertainties in material dosing and particle size distribution, and mixing and environmental conditions on final mechanical UHPC properties. This is achieved by introducing an Automatic Modeling Pipeline that includes advanced data collection, data cleaning, and sophisticated feature selection techniques designed to fully capture the complexities of the UHPC manufacturing process. Employing a diverse array of 10 machine learning algorithms and adopting a Leave-One-Out Cross Validation (LOOCV) [54] training-test strategy with multiple initializations, the proposed methodology ensures the reliability of UHPC mechanical properties predictions.

2.2. Evolutionary Multiobjective Feature Selection

In the domain of machine learning, especially with high-dimensional and small datasets, feature selection (FS) is a pivotal process aimed at enhancing model interpretability, reducing overfitting, and improving prediction performance by eliminating irrelevant or redundant features from the dataset [55]. Traditionally, FS methods have been categorized into three approaches: filter, wrapper, and embedded [7]. However, these methods often suffer from a high possibility of selecting redundant features, experiencing nesting effects, and/or falling into local optima, especially in complex datasets with high dimensionality [7,8].

Feature selection faces three main challenges [8]: the exponential growth of the search space with the number of features; possibly complex interactions among features, where redundancy and complementarity significantly impact prediction performance; and the inherent multiobjective nature of feature selection, which requires a trade-off between maximizing prediction performance and minimizing feature count, which are often conflicting objectives. Significant advancements have been made with the incorporation of evolutionary multiobjective optimization (EMO) techniques into feature selection. However, due to the inherent randomness of the evolutionary process, the outcomes are often unstable, especially when dealing with complex datasets and conditions of data sparsity.

Despite the widespread adoption of multiobjective feature selection (MOFS) due to its capability in global optimization, which eliminates the need for prior assumptions in these algorithms, and their adeptness at handling high- dimensional cases, they typically require relatively large datasets. This necessity, coupled with the inherent randomness of evolutionary processes, contributes to the instability of results obtained from EMO, especially in complex datasets with high dimensionality. As a result, they have been applied primarily to high-dimensional datasets but with large data sizes, especially in classification tasks [56–60]. These challenges are more pronounced in scenarios involving high-dimensional datasets with limited samples, highlighting the need for innovative approaches.

To address the above challenges in high-dimensional datasets with small sizes, the integration of prior knowledge in the process of feature selection is necessary [61]. Evolutionary multiobjective feature selection methodologies distinguish themselves through various core design elements, including solution representation, evaluation functions, initialization strategies, offspring generation methods, environmental selection techniques, and decision-making processes [8]. One potential for the integration of prior knowledge is in the initialization of solutions and also in the mutation function of the feature selection process.

Kropp et al. [62] present a Sparse Population Sampling technique to enhance the efficiency of optimization algorithms in sparse settings by seeding the population with sparse initial solutions, reflecting a strategic use of prior knowledge for algorithm initialization. Similarly, a study by Xu et al. [63] introduces an evolutionary approach that employs duplication analysis to streamline the feature selection process, leveraging patterns of feature redundancy to implicitly incorporate prior insights. Song et al. [64] combine feature clustering based on correlations with particle swarm optimization, using prior knowledge of feature relationships to address feature selection challenges. Ren et al.[65] develop an algorithm for sparse optimization, hinting at the consideration of the distribution of non-zero elements to inform its strategy, thus possibly integrating domain-specific knowledge indirectly. Additionally, Wang et al. [66] apply multiobjective differential evolution to balance feature count minimization with classification performance, potentially adjusting evaluation criteria based on domain-specific feature importance, suggesting an indirect method of utilizing prior knowledge.

Despite these advancements, none of these methods explicitly utilize predefined features as prior knowledge, nor do they directly address problems characterized by high dimensionality combined with small sample sizes.

There is a significant gap in addressing the challenges of EMO in MOFS tasks, particularly in achieving stable results with high-dimensional datasets and small sample sizes. Integrating domain expertise and prior knowledge can influence initial conditions and evaluation trajectories, potentially enhancing the stability and performance of EMO in these contexts. This gap is addressed in this work by the direct utilization of domain knowledge in partially initializing algorithm populations and by finely adjusting mutation probabilities to balance exploration and exploitation. This approach embeds predefined, domain-specific knowledge at the outset of the optimization process, ensuring that evolutionary trajectories are informed by critical insights from the start.

3. Informed Automatic Modeling Pipeline for UHPC Production Process

This section outlines the establishment and application of a modeling pipeline specifically tailored for the UHPC production process, as depicted in Figure 2. The process begins with the Design of Experiments and Augmentation of Design techniques to compile comprehensive datasets. This step is followed by data preprocessing to prepare the data for modeling.

The next phase introduces the Ensemble-based Feature Importance Determination [6], utilizing the prepared data to identify significant features as prior knowledge for the next step. The culmination of the pipeline is the block of Informed Evolutionary Multiobjective Feature and Algorithm Selection (IEM-FAS), which implements a systematic approach to optimize feature and algorithm selection, specifically designed for high-dimensional, small datasets typical in UHPC production. This phase enables the progressive and systematic integration of proposed features based on their significance, thereby facilitating the model's development in the final stage.

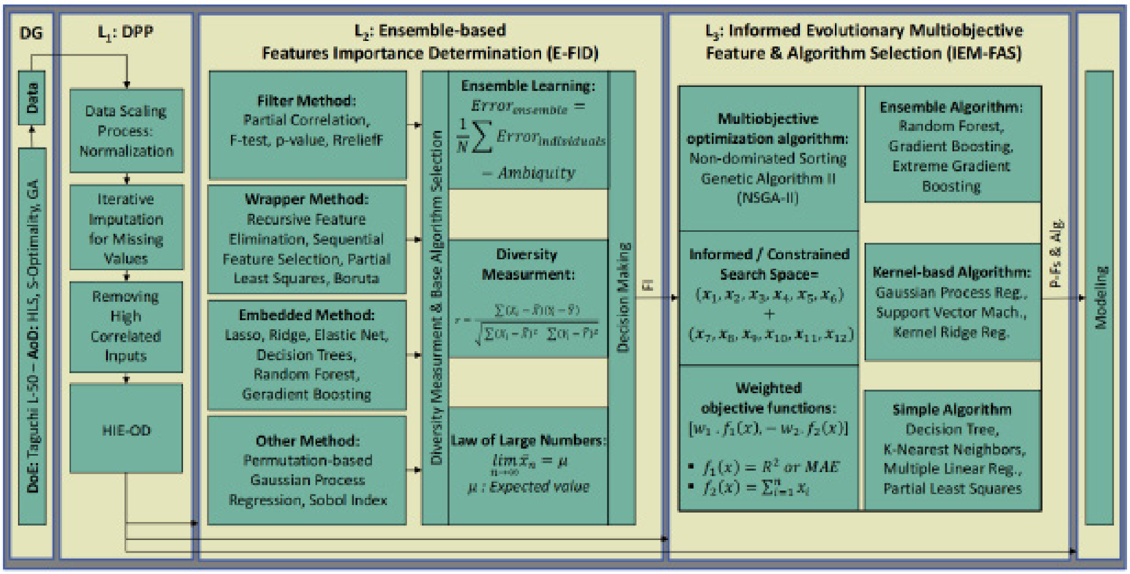

Figure 2: Modeling of Reproducible UHPC with Consistent Properties[2]

3.1. Data Generation

A dataset of x ∈ R22 with N = 150 observations and two outputs (Compressive and Flexural Strength on Day 28 after the mixing process) was generated for this work. For a detailed description of this dataset, including the complete data generation and analysis processes, readers are encouraged to refer to [67].

3.1.1. Key Factors and Characteristics in UHPC Production Process

For this study, a fixed reference recipe with a constant amount of materials is considered. However, the quality of UHPC can be influenced by various critical factors throughout its production process. These factors include material quality, particle size distribution, environmental conditions during raw material storage, measurement errors in the dosing system, and mixing and curing conditions (refer to Table 1). To evaluate the quality of UHPC, alongside mechanical tests at different ages, temperature, electrical conductivity, air content, slump flow test [68], and funnel runtime are also measured in the fresh state.

In the initial stage, the effect of material quality, environmental conditions during raw material storage, and impurities in silica fume are examined by considering variables such as Material Delivery Batch Time (DB), Cement Reactivity (CR), Ingredient Moisture (IM), Ingredient Temperatures (IT), and Graphite content (GRP). Materials are delivered in different batches, and even those from the same company (classified as DB1 and DB2) may exhibit subtle differences. These distinctions, though minor, can introduce variability in material quality at the microstructural level, emphasizing the need to account for such nuances in the production process. Cement Reactivity, influenced by its chemical composition and external factors such as storage duration and environmental conditions, is classified based on storage time. Varying humidity levels during storage can alter the cement's reactivity, impacting the final UHPC quality. Concrete raw materials in industrial settings are typically stored outside without protection from the sun, rain, and humidity. To simulate these conditions,

---

Figure 2: Proposed Automatic Modeling Pipeline for Ultra-High Performance Concrete Manufacturing Process: A Comprehensive Approach from Data Generation to Modeling. (DG: Data Generation, GA: Genetic Algorithm, LHS: Latin Hypercube Sampling, AoD: Augmentation of Design, DoE: Design of Experiments, L: Layer, DPP: Data Preprocessing, HIE-OD: Human-in-the-Loop Informed Ensemble-based Outlier Detection, FI: Feature Importance, MAE: Mean Absolute Error, P-Fs & Alg.: Proposed Features & Algorithm)

the temperature of raw materials before mixing is artificially set to different values. In addition to the fixed water value in the reference recipe, variations simulating humidity are considered. One of the crucial characteristics of UHPC is its low water content formulation; thus, impurities that absorb water are significant. High carbon content in silica fume can reduce workability by absorbing water, impacting cement hydration and final UHPC quality.

The formulation of the recipe, including appropriate ratios of aggregates, Superplasticizers (SPP), and silica fume, is critical for UHPC's strength and durability. Precision in measuring these ingredients and potential measurement errors, along with variations in particle size distribution, introduce complexities. Although these errors may be small (see Table 1), they can lead to significant variations in UHPC quality, especially when amplified by mixing parameters such as Speed (MS) and Duration (MD). Properties of fresh concrete, including Temperature (FCT), Electrical Conductivity (EC), Air Content (AC), Slump Flow (SF), and Funnel Runtime (FR), are crucial for assessing homogeneity, workability, and structural integrity of UHPC. These factors are considered to predict final product quality and provide feedback to operators to avoid off-spec products at the fresh stage of UHPC.

In real UHPC applications, the product is used worldwide under varying environmental conditions. To simulate this variability, different curing conditions, detailed in Figure 3, involving two main stages, are designed in this study. Initially, the UHPC transitions from paste to a hardened state with minimal strength. During the first 24 hours, it is either stored in a humidity-controlled cabinet at 90 % relative humidity and 20 °C (Figure 3a) or covered with plastic film and stored at 20 to 40 °C, depending on environmental conditions (Figure 3b). After the first 24 hours, the specimens are demolded and cured until day 28. They are either maintained in plastic film at 20 °C (Figure 3c) or submerged in water with temperatures varying from 20 to 40 °C(Figure 3d). Integrating these conditions into the developed pipeline provides an in-depth understanding of UHPC production, aiming for optimization and consistency in quality.

(c) Specimens Encased in Plastic Film

(a) Specimens Subjected to Different Humidity and Temperature Conditions

(b) Specimens Subjected to Different Temperature Conditions

(d) Specimens Submerged in Water

Figure 3: Illustration of Various Curing Conditions Employed in this Work on UHPC Production Process

By analyzing information at the fresh stage and adjusting curing conditions, operators can avoid waste and achieve the desired product quality.

3.1.2. Experimental Design and Methodology

This study initiated a structured experimental campaign, comprising 150 designed experiments performed at G.tecz Engineering GmbH in Germany, to delve into the UHPC manufacturing process. Addressing the challenges of data generation in this field, particularly the aspects of cost and time, we implemented a dual-phase approach: the Screening Phase for initial data analysis [6] and the Optimal Phase for detailed process modeling. The first phase established objectives, identified relevant variables, and carried out preliminary analyses, utilizing the Taguchi Orthogonal Array (TOA) [69]. TOA is favored for its efficiency in managing high-dimensional spaces with a limited number of experiments, ensuring a balanced distribution of input variables. In the subsequent phase, the experimental design was augmented through a process incorporating Latin Hypercube Sampling (LHS) [70], which strategically places additional points within the input space to optimize the experimental layout. A Genetic Algorithm [71] maximized the mean distance between these points (S-Optimality [72]), facilitating a comprehensive examination of the input space. The optimal integration of TOA and LHS data points established a robust foundation for further analysis.

The Screening Phase analysis led to the elimination of three variables: Cement Reactivity (CR), Mixing Speed (MS), and Mixing Duration (MD) [6]. These were determined to have negligible impacts on the final quality of the concrete and were therefore excluded from further consideration. For a more detailed understanding of the Screening Phase methodology and its results, interested readers are encouraged to consult [6].

3.1.3. General Setting

Throughout the experiments, the same mixing tool was used, with controlled environmental conditions for material storage and production to mitigate seasonal variations. The temperature of the mixer chamber was consistently maintained near the ambient laboratory temperature of 20 ℃ and was monitored before each experiment to ensure minimal impact on process variability.

3.2. Data Preprocessing

The collected data undergoes two stages of preprocessing: preliminary processing and outlier detection.

3.2.1. Preliminary Data Processing

Data standardization and normalization are utilized to enhance model performance. Standardization scales data to have a mean of zero and a standard deviation of one, while normalization scales data to fall within the range of [0, 1]. This normalization improved consistency and comparability across features, leading to better model performance in this study. As next step, to reduce dimensionality and prevent multicollinearity, Pearson's correlation coefficient [73] is used to identify and remove highly correlated inputs. This process helps in simplifying the model and improving its generalizability.

Iterative Imputation is employed to handle missing data, which constitutes 4 % of the dataset. Traditional imputation methods like mean or median imputation often fail to capture complex feature correlations and can result in biased estimates [74, 75]. Iterative Imputation [76–78], on the other hand, treats each variable with missing values as a function of other variables in a sequential process, offering a refined estimation that respects complex interdependencies among variables. This method, implemented using Scikit-Learn's IterativeImputer [79], employs Bayesian Ridge Regression [80–82] – the default model for the IterativeImputer function – to iteratively model and predict missing values, ensuring a more accurate and robust handling of the incomplete UHPC data.

3.2.2. Human-in-the-Loop Informed Ensemble-based Outlier Detection

Traditional techniques often struggle to identify outliers in complex datasets [83]. Several outlier detection methodologies, each beneficial in specific contexts, have been developed. These include statistical methods that detect deviations through probabilistic models, distance-based approaches that assess spatial separation, clustering-based strategies that identify outliers as ill-fitting data points within clusters, and density-based methods that pinpoint outliers due to their relative isolation in the data space [84,85].

However, these methods face challenges in specific scenarios, such as with small or sparsely distributed datasets, which are common in Design of Experiments contexts. This issue is particularly pronounced in high-dimensional datasets with small sample sizes, where the goal is to evenly cover the input space. Their reliance on proximity or density can lead to inaccuracies in outlier detection when data points lack sufficient neighborhood, cluster, or density characteristics (see Figure 4), potentially resulting in critical errors in measurement outputs [83, 85–88]. Furthermore, traditional methods such as box plots, histogram plots, and linear regression, which primarily focus on linear relationships, prove inadequate in non-linear contexts [83].

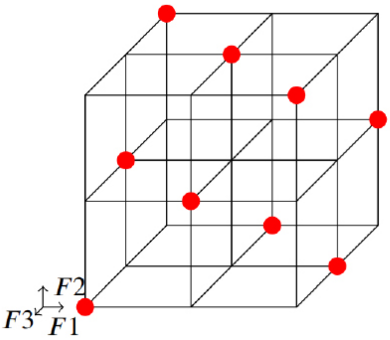

Figure 4: Visual Representation of an L9(33) Orthogonal Array [69]: Given the sparse data design by Taguchi Orthogonal Array, data points cannot be selected based on their distance, density, or neighborhood.

This paper introduces a novel method that combines expert knowledge and Human-in-the-Loop (HITL) insights with the robustness and generalization capabilities of ensemble methods to enhance outlier detection reliability in our case study. The proposed method, named Human-in-the-Loop Informed Ensemble-based Outlier Detection (HIE-OD) (Figure 5), is founded on five key principles:

- Diverse Base Learners
- Application of the Law of Large Numbers
- Domain Expertise for Informed Filtering
- Majority Voting for Ensemble Decision to Recommend Possible Outliers
- HITL Intervention for Final Decision-Making

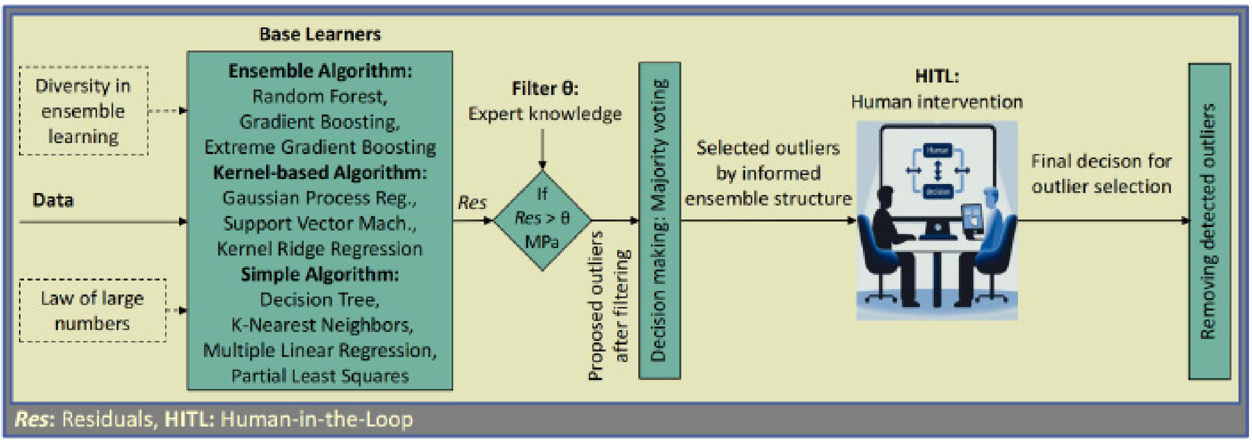

Figure 5: Human-in-the-Loop Informed Ensemble-based Outlier Detection (HIE-OD): Advancing outlier detection with informed ensemble-based method, leveraging expert knowledge and Human-in-the-Loop for precise anomaly detection. Possible outliers, recommended by the informed ensemble component of HIE-OD, are then subject to final decisions made through human intervention in a HITL process.

An ensemble learning approach, inspired by the wisdom of the crowd concept, enhances decision-making in machine learning by leveraging collective intelligence [89]. This method aggregates insights from various base learners (BLs), each contributing unique perspectives, thereby improving generalization and reducing overfitting [89]. The ensemble aims to achieve or exceed the average performance of its base learners, with diversity in the ensemble reducing error, as demonstrated by:

$$Error_{ensemble} = \frac{1}{M}\sum Error_{individuals} - Ambiguity, \tag{3}$$

where Errorindividuals is the ensemble base learners'(BLs) errors, M is the count of BLs, and Ambiguity measures their diversity [90]. This illustrates how diversity minimizes the overall error [91]. Depending on the application, the Law of Large Numbers supports this principle by indicating that a larger number of observations leads to a sample average that more accurately reflects the population mean, which is vital for effective outlier detection:

$$\lim_{N\to\infty} \bar{O}_N = \mu. \tag{4}$$

Here, *ON* represents the average of *N* observations, and μ is the mean value of the population, highlighting the improved reliability with an increasing number of observations. This convergence, as observed in our case study, assumes that the observations are independent, identically distributed, and exhibit finite variance. To leverage this principle, the proposed outlier detector incorporates 10 diverse BLs, ranging from linear to non-linear, parametric to non-parametric, and simple to complex algorithms, as illustrated in Figure 5.

For a dataset comprising N data points $\{d_1; d_2; \ldots ; d_N\}$ and a set of models, the residual R_{ij} for the j-th data point

against predictions from all models is calculated by the proposed method as:

$$R_{ij} = |y_j - \hat{y}_{ij}(d_j)|, \tag{5}$$

where yj is the actual value for the j-th data point, $\hat{y}_{ij}(d_j)$ denotes the predicted value for the *j*-th data point by the *i*-th model. A data point is flagged as a possible outlier if:

$$\max_i(R_{ij}) > \theta, \tag{6}$$

where   is the threshold defined by expert knowledge.

The ultimate decision on outliers is determined using a wisdom of the crowd approach, which requires more than 50 % agreement among the algorithms:

$$C(d) = \frac{1}{M}\sum_{i=1}^{M} \mathbb{1}_{\{f_i(d)=\hat{y}_i \text{ and } R_i(d)>\theta\}}, \tag{7}$$

where *C*(*d*) denotes the consensus for data point *d* , $f_i(d)$ represents the decision function of the *i*-th BL, *M* is the total number of BLs, and   is the consensus threshold set at 15 MPa. The indicator function **1** returns 1 if $R_i(d) >$. A data point *d* is considered a possible outlier if *C*(*d*) exceeds 0.5, indicating majority consensus. If *C*(*d*) exceeds 0.5, the data point *d* is recommended to the HITL for further analysis. The 50 % threshold is the minimum required for the effectiveness of wisdom of the crowd (majority voting), as a binary decision process requires more than half of the votes to favor an option for it to be selected [92]. Setting the threshold below this compromises the purpose of majority voting, while setting it above risks missing true positives. In this study, setting the threshold at 60 % ensures that at least 6 out of 10 base learners agree, which balances minimizing false positives with maintaining the effectiveness of the wisdom of the crowd. By leveraging a blend of multiple BLs, informed detection criteria, and a consensus- and HITL-enhanced decision framework, the HIE-OD presents a comprehensive, sophisticated, and flexible approach to outlier detection.

3.3. Ensemble-based Feature Importance Determination

Within the context of this work, the Ensemble-based Feature Importance Determination (E-FID) framework has been deployed to analyze factors influencing UHPC quality. Unlike approaches that rely on a single model, the ensemble method is recognized for integrating insights from a diverse array of predictive algorithms [89]. This strategy is primarily adopted to overcome limitations inherent in individual models, such as bias and variance issues [91]. Furthermore, it is particularly effective in scenarios characterized by high dimensionality and limited data, where the ensemble approach enhances generalization and reduces the risk of overfitting [89]. By synergistically leveraging the strengths of multiple algorithms, the ensemble framework significantly enhances the reliability of feature importance rankings. This approach effectively mitigates the the law of ensemble learning described in Equation3and leverages the Law of Large Numbers as detailed in Equation4, facilitating a nuanced understanding of the critical factors influencing UHPC quality.

For a comprehensive exposition of the E-FID framework's development and operational specifics, readers are referred to [6].

3.4. Informed Evolutionary Multiobjective Feature and Algorithm Selection Framework

In the Non-dominated Sorting Genetic Algorithm II (NSGA-II) [93], used for feature selection, an individual (chromosome) **x** is represented as a binary vector:

$$\mathbf{x} = [x1; x2; \ldots ; xn] \tag{8}$$

where n is the number of features, and each $x_i \in \{0; 1\}$ indicates the absence (0) or presence (1) of the i-th feature. The fitness of an individual is evaluated through multiple objective functions. Common objectives for feature selection in complex tasks include maximizing model prediction performance and minimizing the number of selected features.

The dominance relation between two individuals **x** and **y** in the case of a minimization problem is defined as:

$$\mathbf{x} \text{ dominates } \mathbf{y} \text{ if } \forall i; f_i(\mathbf{x}) \leq f_i(\mathbf{y}) \text{ and } \exists j; fj(\mathbf{x}) < fj(\mathbf{y}) \tag{9}$$

where f_i represents an objective function.

Crowding distance is a measure of the density of the solution space around a given individual, which helps maintaining diversity in the population. Crossover and mutation are genetic operators used to create new individuals [93]. These operators are typically implemented as follows:

- **Crossover** combines segments of two parent chromosomes to produce offsprings, introducing genetic diversity into the population. A common method used is single-point crossover.
- **Mutation** alters genes within a chromosome with a probability P_{mut} to introduce variability, often implemented as bit-flip mutation.

The algorithm iteratively performs selection, crossover, and mutation to generate new populations. After each iteration, both the parent and offspring populations are sorted based on non-dominance and crowding distance, preparing them for the next generation cycle [93].

The set of optimal solutions $\mathbf{X}^*$ is defined as [94]:

$$\mathbf{X}^* = \arg \min_{\mathbf{x} \in \mathbf{X}} / \max \{ f_1(\mathbf{x}), f_2(\mathbf{x}), \ldots, f_l(\mathbf{x}) \} \tag{10}$$

where l is the number of objectives, **X** is the set of all possible solutions, and f_i are the objective functions to be minimized (or maximized, depending on the problem definition).

In the proposed Informed Non-dominated Sorting Genetic Algorithm II (I-NSGA-II), an individual (ind) is represented as a binary vector (see algorithm 1):

$$\mathbf{X} = [\mathbf{xn}; \mathbf{hk}] = [x1; x2; \ldots ; xn; h_1; h_2; \ldots ; h_k]; \tag{11}$$

where $x_i \in \{0; 1\}$ indicates the absence (0) or presence (1) of the i-th feature, and h_j are hyperparameters for the machine learning algorithm. The total number of features is denoted by n, and the number of hyperparameters by k.

A crucial aspect of our algorithm is the incorporation of predefined features based on prior knowledge. Let $S \subseteq \{1; 2; \ldots ; p\}$ represent the set of indices corresponding to these predefined features (see Figure 6). During the initialization and mutation phases of the algorithm, these predefined features are enforced by setting $x_i = 1$ for each $i \in S$. Mathematically, this enforcement is represented as:

$$x_i = \begin{cases} 1 & \text{if } i \in S \\ x_i & \text{otherwise} \end{cases} \tag{12}$$

This approach ensures the inclusion of predefined features in each individual of the population across generations, thereby enhancing the robustness of the feature selection process. However, to introduce a controlled degree of variability and to avoid stagnation in local optima, the mutation operation is applied with a probability P_{mut}, typically a small value. For predefined features, the mutation probability is effectively reduced or nullified, denoted by P_{mut}^{predef} to minimize the alteration of these features. The mutation step for the i-th feature can thus be expressed as:

$$x_i' = \begin{cases} x_i & \text{if } i \in S \text{ and rand()} > P_{mut}^{predef} \\ 1 - x_i & \text{if } i \in S \text{ and rand()} < P_{mut}^{predef} \\ 1 - x_i & \text{if } i \notin S \text{ and rand()} < P_{mut} \\ x_i & \text{otherwise} \end{cases} \tag{13}$$

where rand(), a function, generates a real-valued random number between 0 and 1.

Algorithm 1 I-NSGA-II:

Require: D = $\{X;y\}$, where $X$is the feature matrix, $y$is the target variable, and $N$is the number of data points. **Require:** Predefined features F_{predef} with selection probability P* jc3 * hps14 \o\al\s\up 5premu$_t^{def}$, and Mutation selection probability P_{mut}.

Require: Population (pop) size Q, Number of generations G, Crossover probability Pc, Mutation probability P_m.

```
function INITIALIZEPOP($Q;$F)
    for $i \leftarrow$ 1 to $Q$ do
        ind$_i \leftarrow$ initialize with F$_{predef}$ and random features
        ind$_i \leftarrow$ append random hyperparameters
    return pop
function CALCULATEFITNESS(ind;$D_{train}$)
    $X_{subset} \leftarrow X$[F$_i$]; F$_i \leftarrow$ feature subset from ind
    H$_i \leftarrow$ hyperparameters from ind
    Train/Validate model on $X_{subset}$ using H$_i$ (CV=10)
    $fit_1 \leftarrow$ model's $R2$ score; $fit_2 \leftarrow -$count(F$_i$)
    return weighted fitness (2 . $fit_1$ ;1 . $fit_2$)
function MUTATE(ind;$P$mut;$P$\* jc3 \* hps14 \o\al\s\up 4premu$_t^{def}$;Fpredef)
    for each feature $f$ in ind do
        if $f \in$ F$_{predef}$ and rand() > $P$\* jc3 \* hps14 \o\al\s\up 4premu$_t^{def}$ then
            Keep $f$ unchanged
        else if $f \notin$ F$_{predef}$ and rand() < $P_{mut}$ then
            Toggle inclusion of $f$ in ind
        else
            Keep $f$ unchanged
    for each hyperparameter $h$ in ind do
        if rand() < $P_{mut}$ then
            Adjust hyperparameter $h$
    return ind
function GA($D_{train}$;$Q$;$G$;$Pc$;$Pm$;$P$mut;$P$\* jc3 \* hps14 \o\al\s\up 4premu$_t^{def}$)
```

```
    $pop \leftarrow$ INITIALIZEPOP($Q$;F)
    **for** $g \leftarrow 1$ to $G$ **do**
        Assess and assign fitness to each ind $\in pop$ using CALCULATEFITNESS(ind;$D_{train}$)
        $offspring \leftarrow$ apply crossover with probability $P_c$ on selected parents; Select parents from $pop$
        Apply mutation with probability $P_m$ on $offspring$
        **for** each ind $\in offspring$ **do**
            ind $\leftarrow$ MUTATE(ind;$P$mut;$P$\* jc3 \* hps14 \o\al\s\up 5premu$_t^{def}$;Fpredef)
            Ensure compliance with F$_{predef}$
            Recalculate fitness using CALCULATEFITNESS(ind;$D_{train}$)
        $pop \leftarrow$ next generation from $pop \cup offspring$
    Fopt;H$_{opt}$ $\leftarrow$ best ind in $pop$ based on multiobjective criteria
    **return** Fopt;H$_{op}$
**for** each run $r \leftarrow 1$ to $R$ **do**    ▹LOOCV with different random initialization of the algorithm in each iteration.
    $D_{train}$;$D_{test}$ $\leftarrow$ Split dataset D using LOOCV
    F$^r_{opt}$;H$^r_{opt}$ $\leftarrow$ GA($D_{train}$;$Q$;$G$;$Pc$;$Pm$;$P$mut;$P$\* jc3 \* hps14 \o\al\s\up 4premu$_t^{def}$)
    Evaluate F$^r_{opt}$;H$^r_{opt}$ on $D_{test}$
    Record the true and predicted values
```

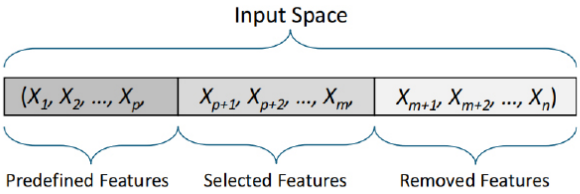

Figure 6: Overview of I-NSGA-II Search Space for Feature Selection: I-NSGA-II is designed to explore a constrained search space, prioritizing predefined features (X_1 to X_p) with a high likelihood of selection during each individual generation. It aims to identify the most significant features (X_{p+1} to X_m) whose interactions with predefined features greatly impact the objectives. This structure limits the search space by integrating prior knowledge into the search space of NSGA-II, enhancing its performance and ensuring stable solutions by addressing the challenges of multiobjective feature selection, especially for high-dimensional data with small sample sizes.

In the mutation operation, if neither condition for mutating predefined ($i \in S$) nor non-predefined features is satisfied – specifically, when rand() $\geq P^{predef}_{mut}$ for predefined features and rand() $\geq P_{mut}$ for others – the feature indicator x_i remains unaltered (N). This *otherwise* case ensures the integrity of the individual by stabilizing the feature composition against unnecessary random perturbations, thereby preserving the current selection state for both sets of features and maintaining the evolutionary approach's balance between exploring the solution space and respecting predefined feature sets. This strategic design guides the genetic algorithm towards effective solutions that adhere to problem-specific constraints.

In the optimization framework of the I-NSGA-II, emphasis is placed on both maximizing the model's predictive accuracy and minimizing the size of the feature set. Weights are assigned to reflect the relative importance of these objectives, with predictive accuracy deemed twice as significant as the simplicity of the model. Consequently, the objective formulation is expressed as:

where $f_1(\mathbf{x}) = R2(\mathbf{x})$ represents the model's predictive accuracy.

The simplicity criterion, [illegible] the model's complexity by the sum of selected features, with each x_i indicating the inclusion (1) or exclusion (0) of the i-th feature. This weighting scheme methodically emphasizes the enhanced priority of accuracy over minimizing feature count, balancing the trade-off between high predictive performance and model simplicity.

The general process of the I-NSGA-II is recorded in Algorithm 1. The core of our methodology relies on a dataset D = $\{X; y\}_{j=1}^{N}$, where X represents the set of feature values, y is the target variable value, and N is the number of data points. The algorithm commences with a predefined set of features $\mathrm{F}_{\mathrm{predef}}$ and operates under specific operational parameters.

The initialization phase, InitializePop, creates a population of Q individuals, each initialized with the prede- fined feature set $\mathrm{F}_{\mathrm{predef}}$ and a random selection of additional features, augmented by randomly chosen hyperparameters. The fitness of each individual is assessed in the CalculateFitness function. This function extracts a feature subset F_i and hyperparameters H_i from each individual, trains a model on X_{subset} using Hi, and calculates fitness based on model accuracy and the count of features used. The dual objectives are to achieve high accuracy and minimize the feature set, while also respecting the constraints imposed by predefined features.

Mutation, handled by the Mutate function, toggles the inclusion of features in an individual based on Pmut, provided the features are not part of $\mathrm{F}_{\mathrm{predef}}$. The genetic algorithm (GA), detailed in the GA function, iteratively performs the following steps: evaluates the population, selects parents, and applies crossover and mutation according to P_c and P_m. Offsprings undergo mutation, compliance adjustment to ensure adherence to predefined feature constraints, and fitness recalculation to update their fitness values based on the new feature set and hyperparameters. After G generations, the algorithm selects the best individual based on the optimized feature subset $\mathrm{F}_{\mathrm{opt}}$ and hyperparameters $\mathrm{H}_{\mathrm{opt}}$.

In the nested validation and evaluation loop, a single test data point is extracted at the start of the IEMFAS framework using the LOOCV mechanism for the final test phase. Then, for training and validation of each algorithm and finding the optimal features and hyperparameters in the I-NSGA-II algorithm, 10-fold CV is used on the training data from LOOCV. After finalizing the model and identifying the optimal features and hyperparameters, the model is evaluated using the unseen data points from LOOCV. These steps are repeated across LOOCV with different initializations for each fold, and the average prediction performance and frequency of selection of each feature are recorded.

3.4.1. Parameter Optimizationfor I-NSGA-II

To configure and run the I-NSGA-II algorithm optimally, we conducted a series of trial-and-error experiments to determine the most effective parameter values. The parameters include a mutation selection probability $P_{\mathrm{mut}} = 0{:}05$, a population size $Q = 100$, a number of generations $G = 100$, a crossover probability $P_c = 0{:}9$, and a mutation probability $P_m = 0{:}2$.

The objective function, also known as the fitness function, consists of two objectives: prediction accuracy and the number of features. To reflect the importance of prediction accuracy over the number of features, the fitness function assigns a weight of 2 to prediction accuracy and a weight of 1 to the number of features. The prediction accuracy is

calculated using the $R2$ metric, chosen after evaluating several metrics including *MAE*, *RMSE*, *R** jc3 * hps14 \o\al\s\up 32*adj*, and $R2$.

The search space for feature selection in I-NSGA-II consists of 16 possible bits. Of these, 6 bits are allocated for predefined features and 6 bits for other features, allowing 4 features to be potentially removed from the pool of 16 features in each run. These configurations are also derived from trial-and-error experiments aimed at achieving the best performance.

3.4.2. Machine Learning Algorithms

Within the IEM-FAS framework (see Figure 2), the feature selection methodology employs a comprehensive set of 10 different machine learning algorithms, ranging from parametric and non-parametric methods, including simple linear, advanced ensemble, and Bayesian approaches. The specific algorithms used are Multiple Linear Regression (MLR) [95], Partial Least Squares (PLS) [95, 96], Kernel Ridge Regression (KRR) [95, 97], K-Nearest Neighbors (KNN) [95, 98], Support Vector Regression (SVR) [95, 99], Decision Tree (DT) [95, 100], Random Forest (RF) [95, 101], Gradient Boosting (GB) [95, 102], Extreme Gradient Boosting (XGB) [103], and Gaussian Process Regression (GPR) [95, 104]. The selected machine learning algorithms are commonly used in industry prediction applications [105], particularly for predicting the mechanical properties of concrete.

3.4.3. Evaluation Metrics of Models Performance

In the process of evaluating the performance of trained models within the testing phase, a comprehensive approach is adopted, utilizing different evaluation metrics tailored specifically for regression tasks. The R^2 metric provides a measure of how well variations regarding the average of output in the observed outcomes are explained by the model:

$$R^2 = 1 - \frac{\sum_{i=1}^{N}(y_i - \hat{y}_i)^2}{\sum_{i=1}^{N}(y_i - y)^2} \tag{15}$$

The R_{adj}^2 adjusts the R^2 statistic based on the number of predictors in the model, preventing overestimation of the model's explanatory power when more predictors are added:

(16)

where D is the number of predictors. The R_{adj}^2 thus accounts for the model's complexity and is always lower than or equal to R^2.

The *MAE* (Mean Absolute Error) measures the average magnitude of the errors in a set of predictions, without considering their direction:

(17)

The*MAPE* (Mean Absolute Percentage Error) expresses the error as a percentage of the observed values, providing a simple interpretation of the error magnitude:

(18)

The*RMSE* (Root Mean Squared Error) is a quadratic scoring rule that measures the average magnitude of the error.

It is calculated as the square root of the average squared differences between the predictions and actual observations:

(19)

In all metrics, yi represents the observed values, $\hat{y}i$ the predicted values, y the mean of the observed values, and N the number of observations.

3.5. UHPC Manufacturing Process Modeling

Building on the ranked features and the best algorithm (with its optimal hyperparameter configuration) proposed by the IEM-FAS framework (see Figure 2), this section outlines a streamlined modeling phase, as detailed in Algorithm 2. The methodology employs the proposed algorithm with LOOCV, beginning with data loading and normalization. The approach incrementally introduces features based on their importance ranking determined by the E-FID and the IEM-FAS frameworks, preparing them alongside the target variable for analysis.

Algorithm 2 UHPC Production Process Modeling

```
function PREPAREDATA($data$, $features$, $target$)
    $X \leftarrow data[features]$
    $y \leftarrow data[target]$
    Normalize $X$ to have values between 0 and 1
    return $X$, $y$
function LOOCV($X$, $y$)
    Initialize $predictions$ as empty list
    for each split in LOOCV of $X$, $y$ do
        Train model on the training set
        $predictions \leftarrow$ Predict on the test set and save it
    return average of the $MAE$, $R^2$ ; $R^2_{adj}$
function MAIN
    $data \leftarrow$ A dataset with $X \in \mathbf{R}^{N\times D}$ and $Y \in \mathbf{R}^{N\times 1}$
    Define $features$, $target$
    for $i \leftarrow 1$ to length($features$) do
        $currentFeatures \leftarrow features[1 : i]$
        $X, y \leftarrow$ PREPAREDATA($data$, $currentFeatures$, $target$)
        $avgMAE$, $avgR^2$ ; $avg\ R^2_{adj} \leftarrow$ LOOCV($X$, $y$)
```

The model is trained and evaluated iteratively, using each data point as a test case while the remaining data points serve as the training set. During this process, features are systematically added according to their importance to assess their cumulative impact on the model's performance. The performance metrics, R^2, R^2_{adj}, and MAE, are calculated based on predictions made on the test data. This approach allows for an effective evaluation of the model's predictive accuracy and provides insight into the impact of each feature as recommended by the IEM-FAS framework.

4. Results and Discussions

4.1. Assessing Data Preprocessing

4.1.1. Correlation Patterns in Studied Factors and UHPC Mechanical Properties

In the preprocessing phase of this study, based on the results of the Screening Phase [6], which led to the removal of three features (Cement Reactivity, Mixing Speed, and Mixing Duration), 19 factors from an initial pool of 22 (Table 1) were selected for further analysis based on their relevance to the final quality of UHPC.

Table 1: This dataset [67] includes a primary Ultra-High Performance Concrete (UHPC) recipe, highlighting variations in material quality, potential measurement errors in the primary recipe, mixing conditions, fresh concrete characteristics, and curing conditions. The cement and silica fume content are fixed across all experiments in this study.

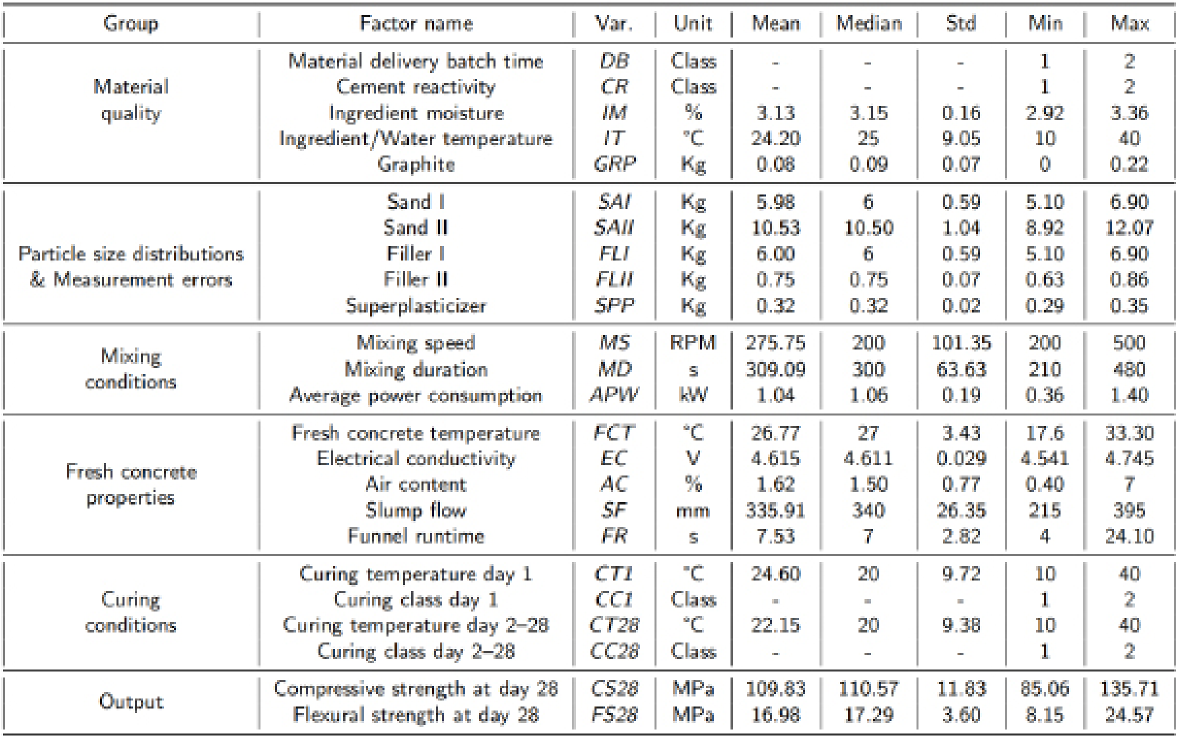

Group	Factor name	Var.	Unit	Mean	Median	Std	Min	Max
Material quality	Material delivery batch time	*DB*	Class	-	-	-	1	2
	Cement reactivity	*CR*	Class	-	-	-	1	2
	Ingredient moisture	*IM*	%	3.13	3.15	0.16	2.92	3.36
	Ingredient/Water temperature	*IT*	°C	24.20	25	9.05	10	40
	Graphite	*GRP*	Kg	0.08	0.09	0.07	0	0.22
Particle size distributions & Measurement errors	Sand I	*SAI*	Kg	5.98	6	0.59	5.10	6.90
	Sand II	*SAII*	Kg	10.53	10.50	1.04	8.92	12.07
	Filler I	*FLI*	Kg	6.00	6	0.59	5.10	6.90
	Filler II	*FLII*	Kg	0.75	0.75	0.07	0.63	0.86
	Superplasticizer	*SPP*	Kg	0.32	0.32	0.02	0.29	0.35
Mixing conditions	Mixing speed	*MS*	RPM	275.75	200	101.35	200	500
	Mixing duration	*MD*	s	309.09	300	63.63	210	480
	Average power consumption	*APW*	kW	1.04	1.06	0.19	0.36	1.40
Fresh concrete properties	Fresh concrete temperature	*FCT*	°C	26.77	27	3.43	17.6	33.30
	Electrical conductivity	*EC*	V	4.615	4.611	0.029	4.541	4.745
	Air content	*AC*	%	1.62	1.50	0.77	0.40	7
	Slump flow	*SF*	mm	335.91	340	26.35	215	395
	Funnel runtime	*FR*	s	7.53	7	2.82	4	24.10
Curing conditions	Curing temperature day 1	*CT1*	°C	24.60	20	9.72	10	40
	Curing class day 1	*CC1*	Class	-	-	-	1	2
	Curing temperature day 2–28	*CT28*	°C	22.15	20	9.38	10	40
	Curing class day 2–28	*CC28*	Class	-	-	-	1	2
Output	Compressive strength at day 28	*CS28*	MPa	109.83	110.57	11.83	85.06	135.71
	Flexural strength at day 28	*FS28*	MPa	16.98	17.29	3.60	8.15	24.57

To refine the dataset and reduce dimensionality, correlations among the factors were examined using the Pearson correlation method. The correlation analysis, illustrated in the heatmap presented in Figure 7, identified strong correlations among certain pairs of variables: *SAI* and *SAII* (Sand Type I and II), *FLI* and *FLII* (Filler Type I and II), and *IT* and *FCT* (Ingredient Temperature and Fresh Concrete Temperature). Due to the high correlations, *SAII*, *FLII*, and *FCT* were removed to avoid factor redundancy. This decision led to a reduction of the factor pool to 16.

Subsequent correlation analysis between the refined set of input factors and key outputs, specifically Compressive Strength at day 28 (*CS28*) and Flexural Strength at day 28 (*FS28*), revealed significant relationships. This analysis highlighted the impact of curing temperature during the second stage (*CT28*) on both mechanical properties of the final UHPC product. Notably, the conditions under which specimens were cured – whether submerged underwater or encased in air within a plastic film from day 2 to day 28 (*CC28*) – were determined to critically affect *FS28*.

This highlights the importance of maintaining a continuously wet surface on UHPC during the curing process. Due to its high binder content (cement and silica fume) and low water content, UHPC does not contain enough water to fully hydrate all the binders. As a result, it is essential to compensate for this water deficit by absorbing moisture from the environment.

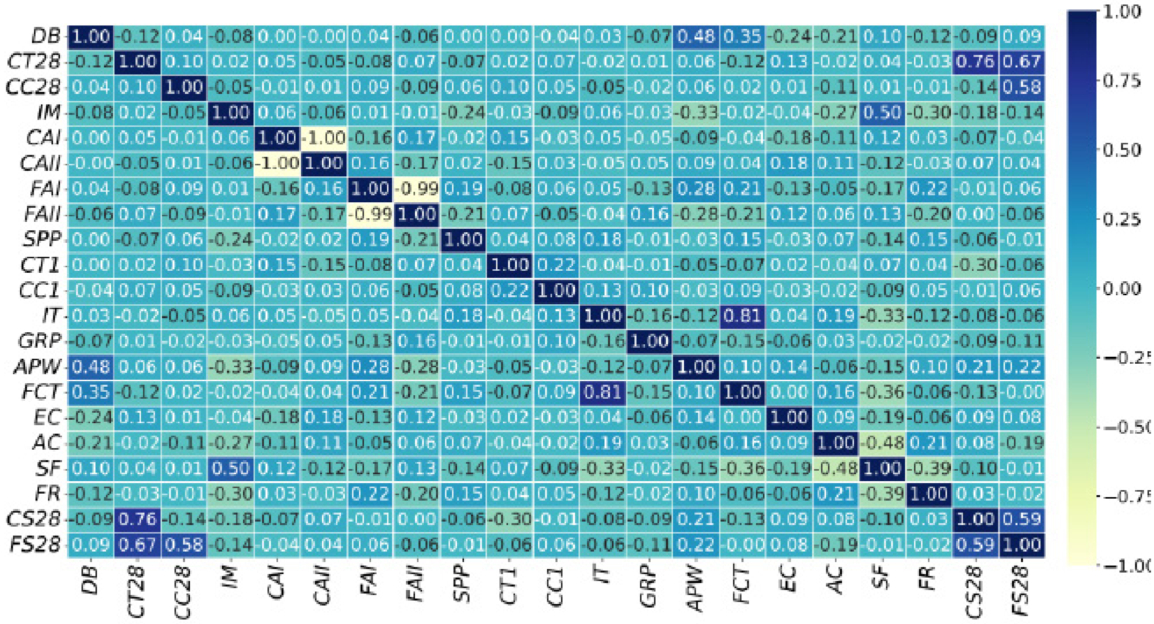

	DB	CT28	CC28	IM	CAI	CAII	FAI	FAII	SPP	CT1	CC1	IT	GRP	APW	FCT	EC	AC	SF	FR	CS28	FS28
DB	1.00	-0.12	0.04	-0.08	0.00	-0.00	0.04	-0.06	0.00	0.00	-0.04	0.03	-0.07	0.48	0.35	-0.24	-0.21	0.10	-0.12	-0.09	0.09
CT28	-0.12	1.00	0.10	0.02	0.05	-0.05	-0.08	0.07	-0.07	0.02	0.07	-0.02	0.01	0.06	-0.12	0.13	-0.02	0.04	-0.03	0.76	0.67
CC28	0.04	0.10	1.00	-0.05	-0.01	0.01	0.09	-0.09	0.06	0.10	0.05	-0.05	-0.02	0.06	0.02	0.01	-0.11	0.01	-0.01	-0.14	0.58
IM	-0.08	0.02	-0.05	1.00	0.06	-0.06	0.01	-0.01	-0.24	-0.03	-0.09	0.06	-0.03	-0.33	-0.02	-0.04	-0.27	0.50	-0.30	-0.18	-0.14
CAI	0.00	0.05	-0.01	0.06	1.00	-1.00	-0.16	0.17	-0.02	0.15	-0.03	0.05	-0.05	-0.09	-0.04	-0.18	-0.11	0.12	0.03	-0.07	-0.04
CAII	-0.00	-0.05	0.01	-0.06	-1.00	1.00	0.16	-0.17	0.02	-0.15	0.03	-0.05	0.05	0.09	0.04	0.18	0.11	-0.12	-0.03	0.07	0.04
FAI	0.04	-0.08	0.09	0.01	-0.16	0.16	1.00	-0.99	0.19	-0.08	0.06	0.05	-0.13	0.28	0.21	-0.13	-0.05	-0.17	0.22	-0.01	0.06
FAII	-0.06	0.07	-0.09	-0.01	0.17	-0.17	-0.99	1.00	-0.21	0.07	-0.05	-0.04	0.16	-0.28	-0.21	0.12	0.06	0.13	-0.20	0.00	-0.06
SPP	0.00	-0.07	0.06	-0.24	-0.02	0.02	0.19	-0.21	1.00	0.04	0.08	0.18	-0.01	-0.03	0.15	-0.03	0.07	-0.14	0.15	-0.06	-0.01
CT1	0.00	0.02	0.10	-0.03	0.15	-0.15	-0.08	0.07	0.04	1.00	0.22	-0.04	-0.01	-0.05	-0.07	0.02	-0.04	0.07	0.04	-0.30	-0.06
CC1	-0.04	0.07	0.05	-0.09	-0.03	0.03	0.06	-0.05	0.08	0.22	1.00	0.13	0.10	-0.03	0.09	-0.03	-0.02	-0.09	0.05	-0.01	0.06
IT	0.03	-0.02	-0.05	0.06	0.05	-0.05	0.05	-0.04	0.18	-0.04	0.13	1.00	-0.16	-0.12	0.81	0.04	0.19	-0.33	-0.12	-0.08	-0.06
GRP	-0.07	0.01	-0.02	-0.03	-0.05	0.05	-0.13	0.16	-0.01	-0.01	0.10	-0.16	1.00	-0.07	-0.15	-0.06	0.03	-0.02	-0.02	-0.09	-0.11
APW	0.48	0.06	0.06	-0.33	-0.09	0.09	0.28	-0.28	-0.03	-0.05	-0.03	-0.12	-0.07	1.00	0.10	0.14	-0.06	-0.15	0.10	0.21	0.22
FCT	0.35	-0.12	0.02	-0.02	-0.04	0.04	0.21	-0.21	0.15	-0.07	0.09	0.81	-0.15	0.10	1.00	0.00	0.16	-0.36	-0.06	-0.13	-0.00
EC	-0.24	0.13	0.01	-0.04	-0.18	0.18	-0.13	0.12	-0.03	0.02	-0.03	0.04	-0.06	0.14	0.00	1.00	0.09	-0.19	-0.06	0.09	0.08
AC	-0.21	-0.02	-0.11	-0.27	-0.11	0.11	-0.05	0.06	0.07	-0.04	-0.02	0.19	0.03	-0.06	0.16	0.09	1.00	-0.48	0.21	0.08	-0.19
SF	0.10	0.04	0.01	0.50	0.12	-0.12	-0.17	0.13	-0.14	0.07	-0.09	-0.33	-0.02	-0.15	-0.36	-0.19	-0.48	1.00	-0.39	-0.10	-0.01
FR	-0.12	-0.03	-0.01	-0.30	0.03	-0.03	0.22	-0.20	0.15	0.04	0.05	-0.12	-0.02	0.10	-0.06	-0.06	0.21	-0.39	1.00	0.03	-0.02
CS28	-0.09	0.76	-0.14	-0.18	-0.07	0.07	-0.01	0.00	-0.06	-0.30	-0.01	-0.08	-0.09	0.21	-0.13	0.09	0.08	-0.10	0.03	1.00	0.59
FS28	0.09	0.67	0.58	-0.14	-0.04	0.04	0.06	-0.06	-0.01	-0.06	0.06	-0.06	-0.11	0.22	-0.00	0.08	-0.19	-0.01	-0.02	0.59	1.00

Figure 7: Pearson Correlation Coefficients for Variables in UHPC Production: This heatmap outlines the correlations between material composition, processing parameters, and environmental factors, as well as their correlations with the compressive (CS28) and flexural (FS28) strengths of UHPC at day 28 of curing. For a detailed explanation of the variables used in this heatmap, see Table 1.

4.1.2. Outlier Detection by HIE-OD

Figure 8 illustrates the distribution of the outputs (*CS28* and *FS28*) using box, histogram, and scatter plots. The box and histogram plots suggest the presence of two potential outliers. As discussed in Section 3.2.2, and further evidenced by the scatter plots in Figure 8, these data points do not provide a clear basis for assessment using clustering and distance-based perspectives commonly applied in outlier detection.

During the first stage of outlier detection, the two potential outliers identified from the box and histogram plots were examined and confirmed as true outliers by domain experts. Additionally, one data point, which exhibited some missing values in fresh concrete characteristics and outputs, was also identified as problematic. Consequently, these three data points were removed from the initial dataset of 150 data points, reducing the dataset to 147 data points.

The results from the HIE-OD method are detailed in Table 2. This table provides a comprehensive summary of votes from an ensemble of 10 BLs for the detected experiments, indicating that the experiments listed were identified as possible outliers by at least one BL. Experiments not listed in the table were not detected as possible outliers by any of the 10 BL.

The criterion for outlier detection by each BL was set to exceed an informed threshold of $\theta = 15$ MPa in residuals. The criterion for outlier detection by the informed ensemble-based part was established using majority voting, with a benchmark of six or more votes required for potential outlier identification. This threshold is depicted in Table 2with red rectangles for easy reference. The experiments marked with red rectangles – numbers 4, 16, 29, 44, 54, 96, 98, and 144 – were identified by the informed ensemble-based part as potential outliers. This threshold of six votes was strategically chosen to balance the need for sensitivity in detecting outliers against the risk of false positives.

Remarkably, each data point identified as an outlier by the informed ensemble part of the HIE-OD method, using the majority voting criterion, underwent subsequent examination by domain experts. This review process validated the ensemble method's recommendations, with all highlighted experiments being confirmed as true outliers.

Following expert validation, all eight data points recommended as outliers were removed from the dataset. This action reduced the dataset to a total of $N = 139$ data points.

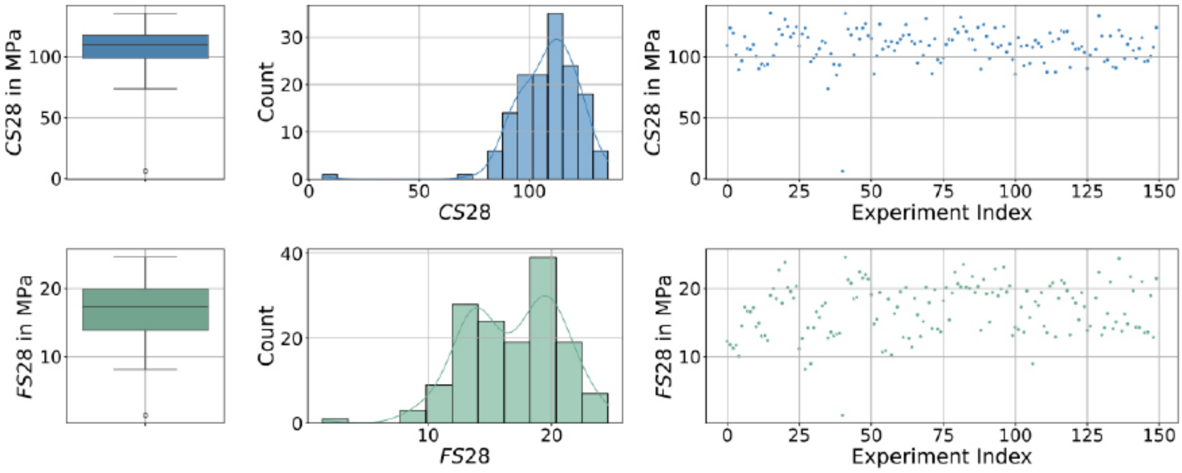

Figure 8: Distribution of Compressive Strength (CS28) and Flexural Strength (FS28) at Day 28 Using Box, Histogram, and Scatter Plots: The box and scatter plots reveal one possible outlier in both outputs, while the histograms suggest two possible outliers, especially for CS28.

Table 2: Summary of detection outcomes from 10 base learners on data points identified as containing potential outliers, with red rectangles highlighting experiments receiving six or more votes indicating a consensus on outlier status. All flagged data points were validated by domain experts. (BL: Base Learner, Exp.: Experiment)

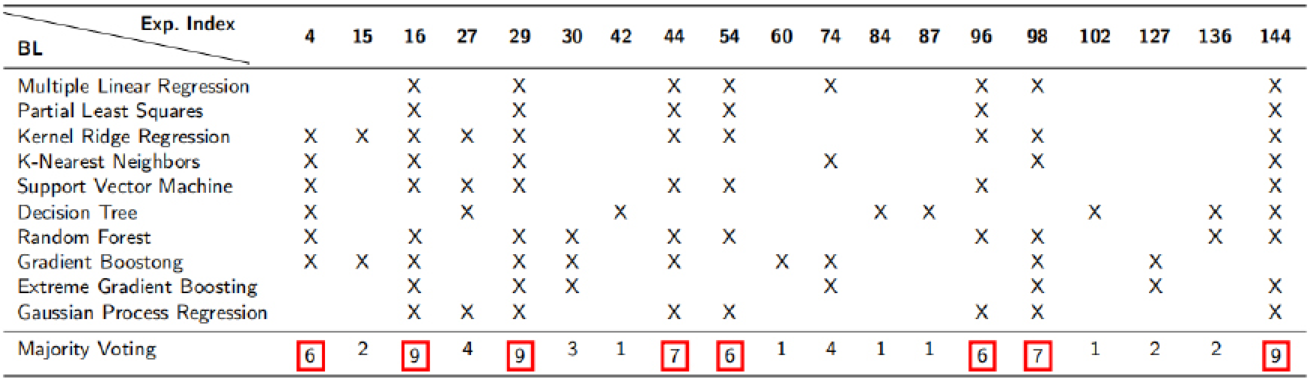

Exp. Index BL	4	15	16	27	29	30	42	44	54	60	74	84	87	96	98	102	127	136	144
Multiple Linear Regression			X		X			X	X		X			X	X				X
Partial Least Squares			X		X			X	X					X					X
Kernel Ridge Regression	X	X	X	X	X			X	X					X	X				X
K-Nearest Neighbors	X		X		X						X				X				X
Support Vector Machine	X		X	X	X			X	X					X					X
Decision Tree	X			X			X					X	X			X		X	X
Random Forest	X		X		X	X		X	X					X	X			X	X
Gradient Boostong	X	X	X		X	X		X		X	X				X		X		
Extreme Gradient Boosting			X		X	X					X				X		X		X
Gaussian Process Regression			X	X	X			X	X					X	X				X
Majority Voting	$\boxed{6}$	2	$\boxed{9}$	4	$\boxed{9}$	3	1	$\boxed{7}$	$\boxed{6}$	1	4	1	1	$\boxed{6}$	$\boxed{7}$	1	2	2	$\boxed{9}$

4.2. Gaining Insights into Feature Importance for UHPC Mechanical Properties Using E-FID

The feature importance analysis for *CS28* (Figure9) highlights the paramount importance of Curing Temperature from day 2 to 28 (*CT28*), underscoring the critical role that environmental conditions play during the second phase of the curing process. Interestingly, the Initial Curing Temperature (*CT1*) on the first day of curing also emerged as a significant factor, albeit with less influence than *CT28*. This suggests that the curing conditions on the first day establish a significant foundational strength, which is further enhanced by the curing conditions from day 2 to day 28. This confirms the well-known fact that higher temperatures accelerate cement hydration. However, it is equally important not to overlook the need for sufficient moisture in such environments.

Ingredient Moisture (*IM*) shows a crucial impact on the final compressive strength of the UHPC, highlighting the importance of moisture content within the mix. Similarly, Average Power Consumption (*APW*), while not a controllable factor, serves as an informative indicator, reflecting the rheology of concrete paste (energy input) during the mixing process and helping to predict the final compressive strength. The addition of Graphite (*GRP*) (to simulate the impurity in silica fume) and of the Curing Conditions from day 2 to day 28 (*CC28*) also play notable roles in the analysis. The presence of carbon (Graphite) as an impurity in silica fume significantly absorbs water in the mixture, leading to a reduction in flowability. This is a critical factor, especially in UHPC, which has a very low water content.

For *FS28*, as detailed in Figure 9, the dominance of curing temperature from day 2 to day 28 (*CT28*) remains unchallenged, reinforcing the overarching influence of the curing processes. However, in a notable departure from the findings related to compressive strength, the curing condition from day 2 to day 28 (*CC28*) stands out as the second most critical factor for flexural strength as well. This distinction highlights the different impact of environmental conditions on the material's resistance to bending stresses.

Ingredient Moisture (*IM*) and initial Curing Temperature (*CT1*) retain their significance, reflecting a consistent theme across both strength characteristics regarding the importance of moisture and initial curing conditions. Notably, Air Content (*AC*), measured after the mixing step in fresh concrete, emerges as a more informative factor for predicting *FS28* compared to *CS28*. This indicates its role in affecting the material's flexural properties, likely through its influence on the pore structure and distribution within the concrete matrix. The comparative analysis of *CS28* and *FS28* results from the E-FID framework reveals a nuanced landscape of feature importance, with several key takeaways:

- Curing Conditions' Primacy: The curing temperature at various stages unequivocally influences both compressive and flexural strength, emphasizing the need for controlled environmental conditions throughout the curing process.

- Differential Impact of Factors: Certain factors, such as *CC28* and *AC*, exhibit a varied influence on *CS28* versus *FS28*. *AC*, particularly, serves as an informative indicator rather than a direct influencing factor, highlighting its role in affecting the material's flexural properties through its influence on the pore structure and distribution.

However, this aspect needs further study, as the presence of carbon is expected to influence compressive strength similarly to flexural strength.

- Importance of moisture and energy consumption of the mixer: The consistent significance of Ingredient Moisture (*IM*) across both analyses underscores the fundamental role of ingredient quality in determining UHPC's mechanical properties. This further emphasizes the necessity of maintaining adequate moisture levels to ensure proper binder hydration and optimal performance. Simultaneously, *APW*, as an informative indicator of mixing efficiency, aids in predicting UHPC's strength outcomes rather than directly influencing them.

4.3. Enhanced Predictive Modeling of UHPC Mechanical Properties Using I-NSGA-II

4.3.1. Impact of I-NSGA-II on Model Performance and Algorithm Selection

This study presents a comprehensive evaluation of various machine learning algorithms for predicting the *CS28* and *FS28* of the UHPC. In the IEM-FAS framework, each algorithm is trained and tested using the LOOCV approach, with different random initializations in each fold. The entire process employs both I-NSGA-II and NSGA-II for both outputs. After training, the performance of each model is tested using the test dataset based on several metrics: $R2$, *MAE*, *MAPE*, and *RMSE*. The results from the average of all folds in the LOOCV loop during the test step are summarized in Table 3afor *CS28* and in Table 3bfor *FS28*.

In Table 3a, models employing the I-NSGA-II demonstrated substantial improvements in $R2$ values. For instance, the MLR model experienced an increase from 72.47 % under traditional Feature Selection (FS) using NSGA-II to 76.37 % with Informed Feature Selection (I-FS) using I-NSGA-II. This improvement indicates a more robust model fit, which can be attributed to the effective integration of domain-specific knowledge within the feature selection process. Moreover, reductions in *MAE*, *MAPE*, and *RMSE* across models further validate the efficacy of I-NSGA-II. KRR and GB also exhibited significant improvements with the application ofI-NSGA-II. Notably, KRR demonstrated an increase in $R2$ from 62.38 % to 76.26 %, marking one of the highest improvements observed. This enhancement is accompanied by a notable decrease in *RMSE* from 7.33 to 5.66, underscoring the effectiveness of I-NSGA-II in reducing prediction errors.

In the context of flexural strength (*FS28*), the SVR model demonstrated the most substantial gains with I-NSGA-

II, as detailed in Table 3b. The $R2$ value surged from 72.62 % under NSGA-II (FS) to 81.75 % under I-NSGA-II (I-FS), highlighting a significant enhancement in the model's ability to capture the variability in flexural strength data. Moreover, the *MAE* reduced dramatically from 1.56 MPa to 0.93 MPa, indicating a higher accuracy in the model's predictive performance. Similarly, the *MAPE* and *RMSE* mirrored this trend, improving from 8.54 % to 7.08 % and from 2.04 to 1.37, respectively. GPR also showed improved performance metrics with the application of I-NSGA-II (FS). The $R2$ value increased from 72.67 % to 81.70 %, and there were significant reductions in both *MAE*, *MAPE*, and *RMSE*, reinforcing the effectiveness ofI-NSGA-II in enhancing the predictive accuracy of complex regression models.

In summary, the application of I-NSGA-II across various machine learning models consistently outperforms the traditional NSGA-II method in all assessed metrics for both compressive and flexural strengths after 28 days (Table 3). This comprehensive analysis conclusively demonstrates the superior predictive capabilities ofthe I-NSGA-II approach, establishing its efficacy in enhancing model performance. Notably, for compressive strength (*CS28*), the MLR model exhibits the most notable enhancement, emerging as the optimal model. Similarly, for flexural strength (*FS28*), the SVR model stands out with the most substantial improvements in all key performance indicators, marking it as the best-performing model under the I-NSGA-II framework. Conversely, for both outputs, the DT model demonstrates the lowest performance, illustrating the weakness of this algorithm in capturing the patterns effectively.

Table 3: Comparative analysis of modeling performance for compressive strength after 28 days (CS28) and flexural strength after 28 days (FS28) using informed feature selection with I-NSGA-II (I-FS) and normal feature selection with NSGA-II (FS). The tables display performance metrics such as R2 , Mean Absolute Error (MAE), Mean Absolute Percentage Error (MAPE), and Root Mean Square Error (RMSE) for various machine learning models.

		R^2 in %		*MAE* in MPa		*MAPE* in %		*RMSE* in MPa	
Models	Abb.	I-FS	FS	I-FS	FS	I-FS	FS	I-FS	FS
Multiple Linear Regression	**MLR**	**76.21**	**72.47**	**4.66**	**5.26**	**4.20**	**4.79**	**5.65**	**6.27**
Partial Least Squares	PLS	75.59	71.35	4.71	5.37	4.26	4.87	5.71	6.40
Kernel Ridge Regression	**KRR**	**76.23**	**62.38**	**4.54**	**6.00**	**4.10**	**5.46**	**5.66**	**7.33**
K-Nearest Neighbors	KNN	70.61	63.25	5.28	5.91	4.89	5.39	6.29	7.25
Support Vector Regression	SVR	73.18	68.93	5.05	5.54	4.56	5.05	6.00	6.66
Decision Tree	DT	60.21	55.34	5.88	6.50	5.34	5.90	7.32	7.99
Random Forest	RF	72.21	64.98	5.01	5.94	4.55	5.43	6.12	7.08
Gradient Boosting	**GB**	**71.53**	**60.77**	**5.01**	**6.00**	**4.54**	**5.46**	**6.20**	**7.49**
Extreme Gradient Boosting	XGB	73.76	65.77	4.76	5.70	4.30	5.18	5.95	7.00
Gaussian Process Regression	GPR	75.36	67.47	4.76	5.73	4.31	5.22	5.71	6.82

(a) Prediction Performance of Various Machine Learning Models For Compressive Strength After 28 Days (*CS28*)

		R^2 in %		*MAE* in MPa		*MAPE* in %		*RMSE* in MPa	
Models	Abb.	I-FS	FS	I-FS	FS	I-FS	FS	I-FS	FS
Multiple Linear Regression	MLR	78.06	74.02	1.15	1.53	8.09	8.64	1.51	1.99
Partial Least Squares	PLS	78.29	72.49	1.14	1.67	8.03	9.26	1.51	2.04
Kernel Ridge Regression	KRR	78.33	73.10	1.07	1.63	8.00	8.90	1.50	2.02
K-Nearest Neighbors	KNN	76.66	73.00	1.22	1.56	8.93	8.71	1.60	1.99
Support Vector Regression	**SVR**	**81.75**	**72.62**	**0.93**	**1.56**	**7.08**	**8.54**	**1.37**	**2.04**
Decision Tree	DT	75.60	71.08	1.18	1.66	8.30	9.19	1.60	2.09
Random Forest	RF	78.80	71.77	1.09	1.67	8.09	9.31	1.49	2.07
Gradient Boosting	GB	77.10	72.26	1.05	1.60	7.82	8.91	1.55	2.05
Extreme Gradient Boosting	XGB	79.46	70.36	1.05	1.59	7.82	8.91	1.51	2.12
Gaussian Process Regression	**GPR**	**81.70**	**72.67**	**0.96**	**1.57**	**7.23**	**8.58**	**1.37**	**2.04**

(b) Prediction Performance of Various Machine Learning Models For Flexural Strength After 28 Days (*FS28*)

4.3.2. Impact of I-NSGA-II on Model Interpretability, Solution Stability, and Feature Selection

The results illustrated in Figures10and11demonstrate the impact of incorporating predefined feature importances on model interpretability within feature selection algorithms. Data from two experimental setups – one utilizing predefined feature importances through I-NSGA-II and the other without, using standard NSGA-II – were collected and analyzed. Each setup involved 139 LOOCV runs across various models, with feature selection frequencies recorded for each model, as discussed in Section 4.3.1.

Figure 10a demonstrates that the first six features, defined a priori as critical (I-NSGA-II), are invariably selected with the highest frequency (139 times) across all model evaluations. In contrast, under the NSGA-II scenario, depicted in Figure 10b, which lacks predefined feature guidance, the same six features also emerge as the most frequently selected. This consistent trend underscores the accuracy of the initial feature importance assessment by the E-FID method. Such parallelism in results validates the initial assumption about the critical nature of these features, thus supporting the effectiveness of informed feature preselection in I-NSGA-II.

A notable divergence between the I-NSGA-II and the standard NSGA-II is observed in the stability of feature selection. I-NSGA-II consistently identifies the predefined features in every model iteration, reflecting enhanced stability and reliability in feature selection. This consistency is absent in the NSGA-II approach, where feature selection exhibits higher variability. This indicates potential instability and unpredictability in model performance without the injection of prior knowledge, which is a critical point of view for evaluating every algorithm.

Moreover, additional features such as Sand Type I (*SAI*), Ingredient Temperature (*IT*), and Material Delivery Batch Time (*DB*) exhibit significantly higher selection frequencies in the I-NSGA-II models. This observation suggests that the algorithm not only reinforces the importance of predefined features but also effectively identifies and elevates other relevant features based on the dataset's intrinsic characteristics.

Conversely, features such as Superplasticizer (*SPP*) and Initial Curing Conditions (*CC1*), which exhibit low or zero selection frequencies in some models under I-NSGA-II, highlight the algorithm's capacity to deprioritize less impactful features.

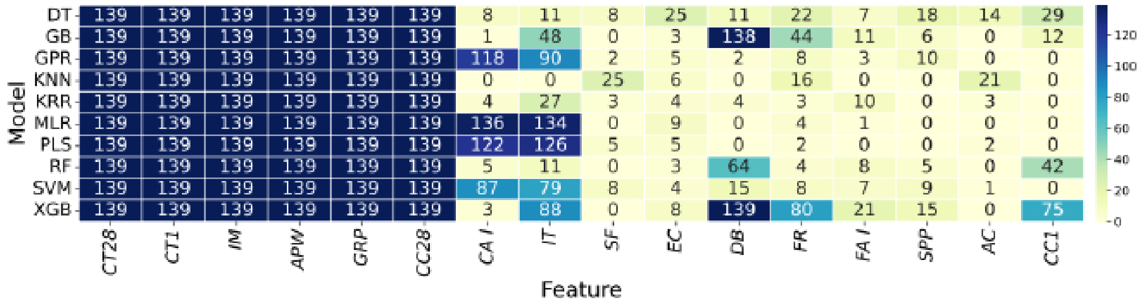

Model	CT28	CT1	IM	APW	GRP	CC28	CA I	IT	SF	EC	DB	FR	FA I	SPP	AC	CC1
DT	139	139	139	139	139	139	8	11	8	25	11	22	7	18	14	29
GB	139	139	139	139	139	139	1	48	0	3	138	44	11	6	0	12
GPR	139	139	139	139	139	139	118	90	2	5	2	8	3	10	0	0
KNN	139	139	139	139	139	139	0	0	25	6	0	16	0	0	21	0
KRR	139	139	139	139	139	139	4	27	3	4	4	3	10	0	3	0
MLR	139	139	139	139	139	139	136	134	0	9	0	4	1	0	0	0
PLS	139	139	139	139	139	139	122	126	5	5	0	2	0	0	2	0
RF	139	139	139	139	139	139	5	11	0	3	64	4	8	5	0	42
SVM	139	139	139	139	139	139	87	79	8	4	15	8	7	9	1	0
XGB	139	139	139	139	139	139	3	88	0	8	139	80	21	15	0	75

(a) Heatmap illustrating the frequency of feature selection in models employing I-NSGA-II for Compressive Strength at 28 days (*CS28*). Features predefined as critical consistently appear with high selection frequency, demonstrating the stability and focus of the I-NSGA-II algorithm.

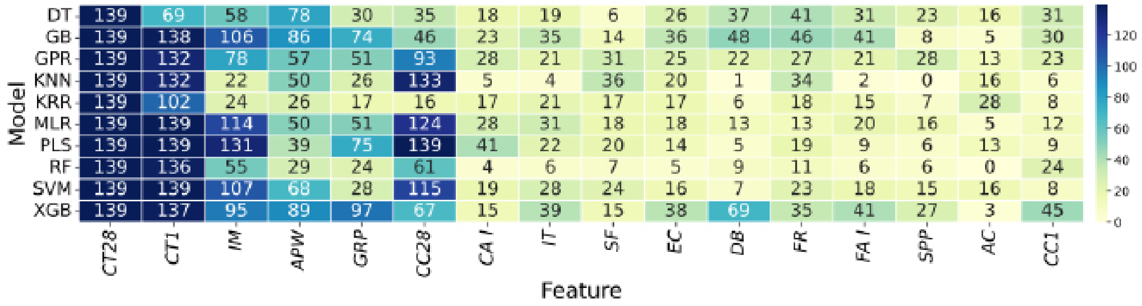

Model	CT28	CT1	IM	APW	GRP	CC28	CA I	IT	SF	EC	DB	FR	FA I	SPP	AC	CC1
DT	139	69	58	78	30	35	18	19	6	26	37	41	31	23	16	31
GB	139	138	106	86	74	46	23	35	14	36	48	46	41	8	5	30
GPR	139	132	78	57	51	93	28	21	31	25	22	27	21	28	13	23
KNN	139	132	22	50	26	133	5	4	36	20	1	34	2	0	16	6
KRR	139	102	24	26	17	16	17	21	17	17	6	18	15	7	28	8
MLR	139	139	114	50	51	124	28	31	18	18	13	13	20	16	5	12
PLS	139	139	131	39	75	139	41	22	20	14	5	19	9	6	13	9
RF	139	136	55	29	24	61	4	6	7	5	9	11	6	6	0	24
SVM	139	139	107	68	28	115	19	28	24	16	7	23	18	15	16	8
XGB	139	137	95	89	97	67	15	39	15	38	69	35	41	27	3	45

(b) Heatmap displaying the frequency of feature selection in models using NSGA-II for *CS28*. This shows more variability in feature selection, highlighting the non-deterministic nature of NSGA-II without predefined feature guidance.

Figure 10: Comparative Analysis of Feature Selection Frequencies in I-NSGA-II and NSGA-II for CS28 : It highlights the increased stability and efficacy of feature selection when domain-specific knowledge is incorporated via I-NSGA-II. The comparison of the results demonstrates the reliability of E-FID for integrating priors into I-NSGA-II. For details about the variables, refer to Table 1. (I-NSGA-II: Informed Non-Dominated Sorting Genetic Algorithm II, CS28 : Compressive Strength at Day 28)

This selective enhancement by I-NSGA-II not only augments the model's interpretability but also clearly delineates which features are consistently valuable. It takes into account the interactions with predefined features to boost prediction performance while simultaneously preserving model simplicity and ensuring stability in the solutions.

In case of *FS28*, the analysis presented in Figure 11 reveals distinct differences in feature selection patterns between the two testing scenarios. In the I-NSGA-II scenario (Figure 11a), features such as Curing Temperature from day 2 to day 28 (*CT28*), Curing Conditions from day 2 to day 28 (*CC28*), Ingredient Moisture (*IM*), Initial Curing Temperature (*CT1*), Air Content (*AC*), and Material Delivery Batch Time (*DB*) show maximum selection frequency (139 times) across all models. This uniformity indicates that these features are consistently deemed crucial when predefined importances are considered, suggesting a strong alignment with the predefined importances and highlighting the influence of domain knowledge in guiding the selection process.

Conversely, the NSGA-II scenario (Figure 11b) demonstrates more variability in feature selection. Features such as *IM*, *CT1*, *AC*, and *DB*, while still frequently selected, show reduced counts compared to the I-NSGA-II scenario.

Additionally, the interaction assessed by I-NSGA-II reveals that Average Power Consumption (*APW*), although significant in the NSGA-II scenario, is less emphasized in I-NSGA-II due to the more critical interactions with predefined features. Conversely, the importance of Graphite (*GRP*) and especially Electrical Conductivity (*EC*) appears less crucial by NSGA-II but shows relatively good interactions with predefined features by I-NSGA-II.

Furthermore, interesting results emerge from the comparison of both scenarios – using I-NSGA-II and NSGA-II

– as illustrated in Figures 10 and 11 for both *CS28* and *FS28*. Notably, I-NSGA-II sets the frequency of selection for some factors to zero in many cases. By comparing both scenarios, it can be concluded that I-NSGA-II tends to definitively decide whether a feature is selected or not, which leads to more stable solutions, higher accuracy in prediction performance, and better interpretability for use cases.

As discussed in Section 4.3.1, the selected algorithm for *CS28* is MLR and for *FS28* is SVR when employing I-NSGA-II, due to their superior prediction accuracy. From Figure 10, the MLR model selects features *CT28*, *CT1*, *IM*, *APW*, *GRP*, *CC28*, *SAI*, *IT*, *EC*, *FR*, and *FLI* for their critical importance in the subsequent investigation phase of the modeling process. Similarly, for SVR, as illustrated in Figure 11, the features *CT28*, *CT1*, *IM*, *APW*, *GRP*, *CC28*, *SAI*, *IT*, *DB*, *SPP*, *SF*, *FR*, *FLI*, and *EC* are selected for the next phase of investigation due to their pivotal roles.

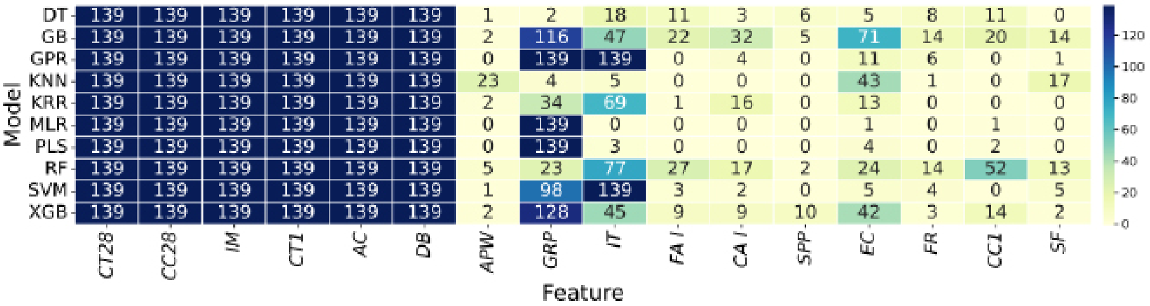

Model	CT28	CC28	IM	CT1	AC	DB	APW	GRP	IT	FA I	CA I	SPP	EC	FR	CC1	SF
DT	139	139	139	139	139	139	1	2	18	11	3	6	5	8	11	0
GB	139	139	139	139	139	139	2	116	47	22	32	5	71	14	20	14
GPR	139	139	139	139	139	139	0	139	139	0	4	0	11	6	0	1
KNN	139	139	139	139	139	139	23	4	5	0	0	0	43	1	0	17
KRR	139	139	139	139	139	139	2	34	69	1	16	0	13	0	0	0
MLR	139	139	139	139	139	139	0	139	0	0	0	0	1	0	1	0
PLS	139	139	139	139	139	139	0	139	3	0	0	0	4	0	2	0
RF	139	139	139	139	139	139	5	23	77	27	17	2	24	14	52	13
SVM	139	139	139	139	139	139	1	98	139	3	2	0	5	4	0	5
XGB	139	139	139	139	139	139	2	128	45	9	9	10	42	3	14	2

(a) Heatmap illustrating the frequency of feature selection by I-NSGA-II across all models for FS28, showing high selection consistency for predefined features.

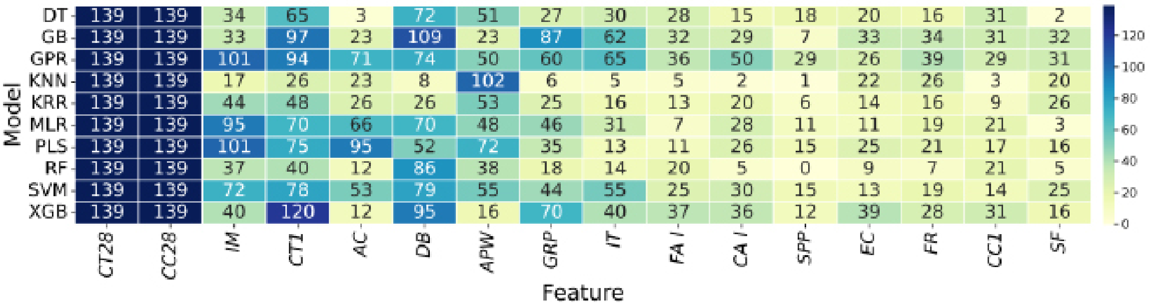

Model	CT28	CC28	IM	CT1	AC	DB	APW	GRP	IT	FA I	CA I	SPP	EC	FR	CC1	SF
DT	139	139	34	65	3	72	51	27	30	28	15	18	20	16	31	2
GB	139	139	33	97	23	109	23	87	62	32	29	7	33	34	31	32
GPR	139	139	101	94	71	74	50	60	65	36	50	29	26	39	29	31
KNN	139	139	17	26	23	8	102	6	5	5	2	1	22	26	3	20
KRR	139	139	44	48	26	26	53	25	16	13	20	6	14	16	9	26
MLR	139	139	95	70	66	70	48	46	31	7	28	11	11	19	21	3
PLS	139	139	101	75	95	52	72	35	13	11	26	15	25	21	17	16
RF	139	139	37	40	12	86	38	18	14	20	5	0	9	7	21	5
SVM	139	139	72	78	53	79	55	44	55	25	30	15	13	19	14	25
XGB	139	139	40	120	12	95	16	70	40	37	36	12	39	28	31	16

(b) Heatmap displaying the frequency of feature selection by NSGA-II across all models for *FS28*. Variability in feature selection underlines the challenges of NSGA-II without domain-specific guidance, resulting in less consistent feature prioritization.

Figure 11: Comparative Analysis of Feature Selection Frequencies in the Models Using I-NSGA-II versus NSGA-II for FS28 : These heatmaps highlight the impact of incorporating predefined feature importances on the stability and reliability of the feature selection process. The variables are explained in Table 1. (I-NSGA-II: Informed Non-Dominated Sorting Genetic Algorithm II, FS28 : Flexural Strength at Day 28)

4.4. UHPC Manufacturing Process Modeling

The IEM-FAS framework identified the MLR algorithm as the optimal choice for predicting *CS28*. As illustrated in Table 3a and Figure 10, a set of 11 critical features were selected to enhance the accuracy of the MLR model. In contrast, for predicting *FS28*, the framework recommended the SVR algorithm, supported by a distinct pool of 14 significant features (Table 3b, Figure 11).

The modeling process (Algorithm 2) for *CS28* commenced with the inclusion of the most influential factor, *CT28*.

Utilizing *CT28* as a solitary predictor yielded an $R2$ value of 57.10 %, demonstrating the substantial role of curing temperature in explaining the variance of *CS28*. Subsequently, incorporating the first 24 hours of curing temperature (*CT1*) led to a significant enhancement in model performance, increasing $R2$ to 66.61 %. This improvement suggests that *CT1* provides additional variance information not captured by *CT28*. The further inclusion of the impact factor (*IM*) elevated the $R2$ to 70.53 %, indicating its critical contribution to the predictive model.

The addition of (*APW*) resulted in a slight performance boost, with $R2$ increasing to 71.16 %. Incorporating (*GRP*) and (*CC28*) further refined the model, yielding a notable $R2$ improvement to 75.40 %. Although the inclusion of additional features such as *SAI* and *IT* only marginally increased $R2$ to 75.77 %, these features were retained based on domain expertise, recognizing their potential significance in practical scenarios. Ultimately, the model achieved its highest adjusted $R2$ of 74.28 % with a core subset of six predictors: *CT28*, *CT1*, *IM*, *APW*, *GRP*, and *CC28*. This subset represents a balance between model accuracy and computational efficiency, highlighting the key variables necessary for optimal *CS28* prediction.

In the modeling of *FS28*, the process began with the inclusion of *CT28*, which yielded an initial average $R2$ of 46.23 %, indicating the significant impact of temperature on flexural strength at day 28. The subsequent inclusion of *CC28* substantially improved the model's performance, raising the average $R2$ to 74.32 %. This notable improvement underscores the importance of the interaction between curing conditions after 24 hours until day 28 in predicting *FS28*. However, the introduction of additional variables such as *IM*, *CT1*, and *AC* led to fluctuations in model accuracy. Specifically, the incorporation of *IM* slightly decreased the average $R2$ to 74.02 %, while *CT1* and *AC* further reduced it to 72.56 % and 71.51 %, respectively. These variations suggest that while some features introduce valuable new information, others may contribute to model complexity without a corresponding increase in predictive power. The highest average $R2$ of 78.89 % was achieved with a specific combination of features, including *DB* and *IT*, highlighting their importance in enhancing model accuracy.

These findings (Figure 12) emphasize the critical role of curing conditions in optimizing the mechanical properties of UHPC. Moreover, factors such as delivery batch timing and raw material storage conditions, which affect material moisture and temperature, significantly influence the quality of UHPC. Additionally, measurement errors in key materials, such as sand and impurities in silica fume (simulated as Graphite content), have a substantial impact on UHPC performance.

(a) Prediction Performance of MLR for *CS28*: Average R^2, R^2_{adj}, and *MAE* in the test phase as the number of features increases. The Sub:6 consists of *CT28*, *CT1*, *IM*, *APW*, *GRP*, and *CC28*. The Sub:8 consists of all features from Sub:6 plus *SAI* and *IT*.

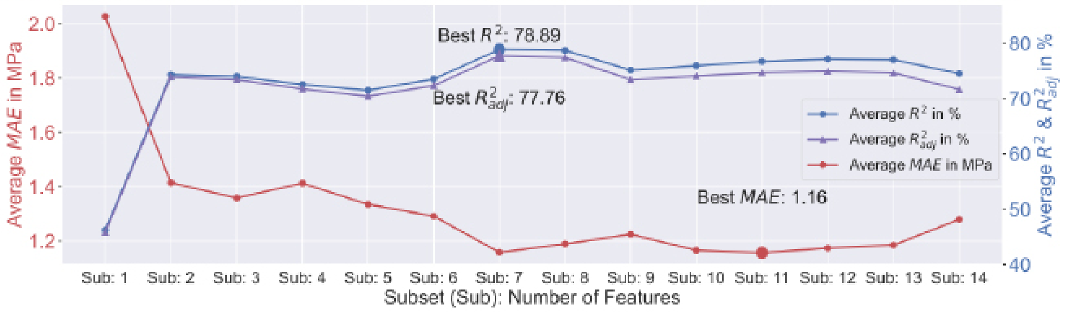

(b) Prediction Performance of SVR for *FS28*: Average R^2, R^2_{adj}, and *MAE* in the test phase as the number of features increases. The Sub:7 consists of *CT28*, *CC28*, *IM*, *CT1*, *AC*, *DB*, and *IT*.

Figure 12: Comparative Performance Evaluation of MLR (Multiple Linear Regression) and SVR (Support Vector Regression) in the Test Phase: This figure highlights the impact of adding features on the prediction metrics for Compressive Strength at day 28 (CS28) and Flexural Strength at day 28 (FS28). The variables are explained in Table 1.

The proposed modeling strategy offers a robust approach to improving UHPC quality, particularly in the event of production faults. By enabling real-time prediction of mechanical properties, this strategy allows for prompt adjustments to the UHPC mixture to ensure target performance values are met. If predictions indicate that the mixture will not achieve the desired properties, corrective actions can be taken in two primary ways:

- Modifying the fresh mix based on the identified importance of each parameter, followed by additional mixing and re-evaluation of the predicted outcomes.
- Adjusting the curing regime, including conditions and temperature, to further enhance the mechanical properties of the UHPC.

5. Conclusions and Future Work

This study presents an Informed Automatic Modeling Pipeline, spanning from the Design of Experiments to the modeling phase, aimed at predicting the mechanical properties of UHPC in real-time. By adopting a holistic approach to UHPC manufacturing, the pipeline addresses the challenge of replicating UHPC products with consistent mechanical properties using the same recipe, despite inherent uncertainties in the production process. This comprehensive perspective on UHPC manufacturing and its impact on mechanical properties is, to the authors' knowledge, uniquely addressed in this work. The research contributes to a larger project aimed at developing a self-healing production system for the construction industry, capable of continuously monitoring UHPC quality and recommending real-time corrective actions.

Dueto the lack of datasets with a holistic view of the UHPC manufacturing process, 150 experiments were designed and conducted at the laboratory of G.tecz Engineering GmbH. The limited number of experiments, coupled with the complex nature of the manufacturing process, resulted in data sparsity. To mitigate this challenge, the study emphasizes dimensionality reduction and feature selection for modeling UHPC's mechanical properties.

A key contribution of this research is addressing the significant challenges associated with MOFS in high-dimensional contexts. These challenges include an exponentially expanding search space, ambiguity in identifying optimal interactions in complex and sparse datasets, and conflicts among objectives. The development ofthe I-NSGA- II, which incorporates insights from the E-FID framework into the traditional NSGA-II algorithm, effectively addresses these issues. The I-NSGA-II not only overcomes the instability typically associated with MOFS in high-dimensional, limited-sample scenarios but also enhances the interpretability and stability of feature selection.

The findings demonstrate that the I-NSGA-II outperforms the standard NSGA-II in two critical aspects. First, it achieves superior prediction performance. Second, it improves the interpretability of the models and the consistency of the feature selection process. Specifically, I-NSGA-II stabilizes feature selection frequency, either consistently selecting or excluding features across all iterations, in contrast to the considerable variability observed with NSGA-II.

The analysis revealed that curing temperature and curing humidity are the most critical factors influencing UHPC quality. Additional key parameters include sand (in terms of content and particle size distribution), graphite content (as an impurity in silica fume), and the moisture and temperature conditions during raw material storage. These findings highlight the necessity of careful control over these variables to improve UHPC quality.

The proposed modeling strategy can significantly improve UHPC quality control by addressing potential production faults and enabling real-time prediction of mechanical properties. This allows mixer operators to assess whether the UHPC mixture will meet the target specifications.

While the results are promising, this study is limited to datasets concerning the compressive and flexural strength of UHPC. Future research should explore a broader range of datasets to validate and refine the proposed methodologies in real-world UHPC manufacturing settings. Addressing these aspects will enable the developed framework to contribute more comprehensively to the field of concrete production, ensuring higher quality and performance across various concrete types.

Data availability

Research dataset (generated by the Welch test function [9, 10]) will be made available upon request. Our experimental datasets, supplied by our industry project partner, contains sensitive and confidential information and, therefore, cannot be publicly disclosed.

Acknowledgment

This project [HA project no. 1011/21-13] is financed with funds of LOEWE – Landes-Offensive zur Entwicklung Wissenschaftlich-ökonomischer Exzellenz, Förderlinie 3: KMU-Verbundvorhaben (State Offensive for the Develop- ment of Scientific and Economic Excellence).

Appendix: Evaluation ofI-NSGA-II on Data Generated by the Welch Test Function

The Welch test function, characterized by its complex interactions and nonlinear effects, serves as a benchmark for evaluating optimization algorithms [9,10]. The function y is defined as follows:

$$\begin{aligned} y = & \frac{5x_{12}}{1+x_1} + 5(x_4 - x_{20})^2 + x_5 + 40x_{19}^3 - 5x_{19} + 0.05x_2 + 0.08x_3 - 0.03x_6 + 0.03x_7 \\ & - 0.09x_9 - 0.01x_{10} - 0.07x_{11} + 0.25x_{13}^2 - 0.04x_{14} + 0.06x_{15} - 0.01x_{17} - 0.03x_{18}, \end{aligned} \tag{20}$$

where the input domain is $x_i \in [-0{:}5; 0{:}5]$ for $i = 1; \ldots ; 20$. From the Welch function (Equation 20), it is evident that inputs $x1, x4, x5, x12, x13, x19$, and $x20$ are the most significant features.

To assess the performance ofthe I-NSGA-II algorithm on data generated by the Welch test function ($X \in \mathbf{R}250{\times}20$), the most significant features were identified using the E-FID framework ($x4, x12, x13, x19, x20$) and incorporated as prior knowledge into the IEM-FAS framework. The optimization process was conducted using advanced machine learning algorithms, and the results comparing I-NSGA-II with the classical NSGA-II are presented in Table 4 and Figure 14. The results show that I-NSGA-II outperforms classical NSGA-II in two key aspects: prediction accuracy and solution stability.

As demonstrated in Table4, the I-NSGA-II significantly enhances the prediction accuracy of models. For instance, the SVR model's $R2$ value improved from 66.74 % with NSGA-II to 81.62 % with I-NSGA-II. Regarding the stability of solutions across different algorithm initializations and data partitioning, Figure 14aillustrates the frequency of feature selection by I-NSGA-II, while Figure 14b shows the selection frequency using classical NSGA-II over 250 iterations in a LOOCV strategy. The results indicate that I-NSGA-II tends to produce more stable solutions compared to classical NSGA-II. For example, in both MLR and SVR models, the importance of features $x1$ and $x5$ is more pronounced when using I-NSGA-II. These features are also crucial according to the Welch function (Equation 20), demonstrating that I-NSGA-II is more likely to identify significant features with strong interactions with predefined features compared to classical NSGA-II.

Table 4: Comparative analysis of modeling performance on data generated by the Welch test function

using informed feature selection with I-NSGA-II (I-FS) and normal feature selection with NSGA-II (FS). The table displays performance metrics such as R2 , Mean Absolute Error (MAE), and Root Mean Square Error (RMSE) for various machine learning models.

		R^2 in %		MAE in MPa		RMSE in MPa	
Models	Abb.	I-FS	FS	I-FS	FS	I-FS	FS
Multiple Linear Regression	**MLR**	**84.15**	**78.88**	**0.6959**	**0.7973**	**0.8481**	**0.9789**
Kernel Ridge Regression	KRR	81.98	74.08	0.7255	0.8651	0.9042	1.0845
Support Vector Regression	**SVR**	**81.62**	**66.74**	**0.7163**	**0.9329**	**0.9132**	**1.2284**
Decision Tree	DT	49.85	46.76	1.1592	1.1833	1.5085	1.5542
Random Forest	RF	71.01	68.81	0.8814	0.9016	1.1470	1.1896

References:

T. Czigler, S. Reiter, P. Schulze, K. Somers, Laying the foundation for zero-carbon cement, volume 9, McKinsey & Company, 2020.

A. Abrishambaf, M. Pimentel, S. Nunes, C. Costa, Multi-level study on uhpfrc incorporating ecat, volume 318, Construction and Building Materials, 2022, p. 125976. URL: http://dx.doi.org/10.1016/j.conbuildmat.2021.125976. doi:10.1016/j.conbuildmat.2021.125976.

S. Abbas, M. L. Nehdi, M. A. Saleem, Ultra-high performance concrete: Mechanical performance, durability, sustainability and implementation challenges, volume 10, International Journal of Concrete Structures and Materials, 2016, pp. 271–295. URL: http://dx.doi.org/10.1007/s40069-016-0157-4. doi:10.1007/s40069-016-0157-4.

J. Du, W. Meng, K. H. Khayat, Y. Bao, P. Guo, Z. Lyu, A. Abu-Obeidah, H. Nassif, H. Wang, New development of ultra-high-performance concrete (UHPC), volume 224, Composites Part B: Engineering, 2021, p. 109220.

M. T. Marvila, A. R. G. de Azevedo, P. R. de Matos, S. N. Monteiro, C. M. F. Vieira, Materials for production of high and ultra- high performance concrete: Review and perspective of possible novel materials, volume 14, Materials, 2021, p. 4304. URL: http://dx.doi.org/10.3390/ma14154304. doi:10.3390/ma14154304.

F. Rezazadeh P., A. Dürrbaum, G. Zimmermann, A. Kroll, Leveraging ensemble structures to elucidate the impact of factors that influence the quality of ultra-high performance concrete, 2023 IEEE Symposium Series on Computational Intelligence (SSCI), 2023, pp. 180–187. URL: http://dx.doi.org/10.1109/ssci52147.2023.10371800. doi:10.1109/ssci52147.2023.10371800.

M. Amoozegar, B. Minaei-Bidgoli, Optimizing multi-objective PSO based feature selection method using a feature elitism mechanism, volume 113, Expert Systems with Applications, 2018, pp. 499–514. URL: http://dx.doi.org/10.1016/j.eswa.2018.07.013. doi:10.1016/j.eswa.2018.07.013.

R. Jiao, B. H. Nguyen, B. Xue, M. Zhang, A survey on evolutionary multiobjective feature selection in classification: Approaches, applications, and challenges, IEEE Transactions on Evolutionary Computation, 2024, p. 1. URL: http://dx.doi.org/10.1109/tevc.2023.3292527. doi:10.1109/tevc.2023.3292527.

E. N. Ben-Ari, D. M. Steinberg, Modeling data from computer experiments: An empirical comparison of kriging with mars and projection pursuit regression, volume 19, Quality Engineering, 2007, p. 327–338. URL: http://dx.doi.org/10.1080/08982110701580930. doi:10.1080/08982110701580930.

W. J. Welch, R. J. Buck, J. Sacks, H. P. Wynn, T. J. Mitchell, M. D. Morris, Screening, predicting, and computer experiments, volume 34, Technometrics, 1992, p. 15. URL: http://dx.doi.org/10.2307/1269548. doi:10.2307/1269548.

P. Ziolkowski, M. Niedostatkiewicz, Machine learning techniques in concrete mix design, volume 12, Materials, 2019, p. 1256. URL: http://dx.doi.org/10.3390/ma12081256. doi:10.3390/ma12081256.

S. Popovics, Analysis of concrete strength versus water-cement ratio relationship, volume 87, ACI Materials Journal, 1990, pp. 517–529. URL: http://dx.doi.org/10.14359/1944. doi:10.14359/1944.

M. Zain, S. M. Abd, K. Sopian, M. Jamil, A. Che-Ani, Mathematical regression model for the prediction of concrete strength, volume 10, WSEAS, Mathematics and Computers in Science and Engineering, 2008, pp. 313–330.

D. Dutta, S. V. Barai, Prediction of compressive strength of concrete: machine learning approaches, Springer, Recent Advances in Structural Engineering, Volume 1: Select Proceedings of SEC 2016, 2019, pp. 503–513.

E. Ozbay, A. Oztas, A. Baykasoglu, H. Ozbebek, Investigating mix proportions of high strength self compacting concrete by using Taguchi method, volume 23, Construction and Building Materials, 2009, pp. 694–702. URL: http://dx.doi.org/10.1016/j.conbuildmat.2008.02.014. doi:10.1016/j.conbuildmat.2008.02.014.

A. Farzampour, Compressive behavior of concrete under environmental effects, in: Compressive Strength of Concrete, IntechOpen, 2020, pp. 92–104. URL: http://dx.doi.org/10.5772/intechopen.85675. doi:10.5772/intechopen.85675.

K. Safranek, Influence of different mixing processes on the strength of ultra-high strength concretes, reposiTUm, Vienna University of Technology, 2007. URL: https://repositum.tuwien.at/handle/20.500.12708/10881.

I.-C. Yeh, Modeling of strength of high-performance concrete using artificial neural networks, volume 28, Cement and Concrete Research, 1998, pp. 1797–1808. URL: http://dx.doi.org/10.1016/s0008-8846(98)00165-3. doi:10.1016/s0008-8846(98)00165-3.

I.-C. Yeh, Modeling slump flow of concrete using second-order regressions and artificial neural networks, volume 29, Cement and Concrete Composites, 2007, pp. 474–480. URL: http://dx.doi.org/10.1016/j.cemconcomp.2007.02.001. doi:10.1016/j.cemconcomp.2007.02.001.

A. Kabir, M. Hasan, K. Miah, Predicting 28 days compressive strength of concrete from 7 days test result, Proceedings of the International Conference on Advances in Design and Construction of Structures, 2012, pp. 18–22.

H. Y. Aydogmus, H. I. Erdal, O. Karakurt, E. Namli, Y. S. Turkan, H. Erdal, A comparative assessment of bagging ensemble models for modeling concrete slump flow, volume 16, Computers and Concrete, 2015, pp. 741–757. URL: http://dx.doi.org/10.12989/cac.2015.16.5.741. doi:10.12989/cac.2015.16.5.741.

R. Jin, Q. Chen, A. B. Soboyejo, Non-linear and mixed regression models in predicting sustainable concrete strength, volume 170, Construction and Building Materials, 2018, pp. 142–152. URL: http://dx.doi.org/10.1016/j.conbuildmat.2018.03.063. doi:10.1016/j.conbuildmat.2018.03.063.

H. U. Ahmed, A. A. Abdalla, A. S. Mohammed, A. A. Mohammed, Mathematical modeling techniques to predict the compressive strength of high-strength concrete incorporated metakaolin with multiple mix proportions, volume 5, Cleaner Materials, 2022, p. 100132. URL: http://dx.doi.org/10.1016/j.clema.2022.100132. doi:10.1016/j.clema.2022.100132.

A. Marani, A. Jamali, M. L. Nehdi, Predicting ultra-high-performance concrete compressive strength using tabular generative adversarial networks, volume 13, Materials, 2020, p. 4757. URL: http://dx.doi.org/10.3390/ma13214757. doi:10.3390/ma13214757.

M. H. Rafiei, W. H. Khushefati, R. Demirboga, H. Adeli, Neural network, machine learning, and evolutionary approaches for concrete material characterization, volume 113, ACI Materials Journal, 2016, pp. 781–789. URL: http://dx.doi.org/10.14359/51689360. doi:10.14359/51689360.

B. A. Young, A. Hall, L. Pilon, P. Gupta, G. Sant, Can the compressive strength of concrete be estimated from knowledge of the mixture proportions?: New insights from statistical analysis and machine learning methods, volume 115, Cement and Concrete Research, 2019, pp. 379–388. URL: http://dx.doi.org/10.1016/j.cemconres.2018.09.006. doi:10.1016/j.cemconres.2018.09.006.

M. Shi, W. Shen, Automatic modeling for concrete compressive strength prediction using auto-sklearn, volume 12, Buildings, 2022, p. 1406. URL: http://dx.doi.org/10.3390/buildings12091406. doi:10.3390/buildings12091406.

J. Yu, R. Pan, Y. Zhao, High-dimensional, small-sample product quality prediction method based on MIC-stacking ensemble learning, volume 12, Applied Sciences, 2021, p. 23. URL: http://dx.doi.org/10.3390/app12010023. doi:10.3390/app12010023.

F. Rezazadeh, A. Kroll, Predicting the compressive strength of concrete up to 28 days-ahead: comparison of 16 machine learning algorithms on benchmark datasets, 32. Workshop Computational Intelligence, 2022, pp. 53–75.

N.-H. Nguyen, J. Abellán-García, S. Lee, E. Garcia-Castano, T. P. Vo, Efficient estimating compressive strength of ultra-high performance concrete using xgboost model, volume 52, Journal of Building Engineering, 2022, p. 104302. URL: http://dx.doi.org/10.1016/j.jobe.2022.104302. doi:10.1016/j.jobe.2022.104302.

E. Saleh, A. Tarawneh, M. Naser, M. Abedi, G. Almasabha, You only design once (yodo): Gaussian process-batch Bayesian optimization framework for mixture design of ultra high performance concrete, volume 330, Construction and Building Materials, 2022, p. 127270. URL: http://dx.doi.org/10.1016/j.conbuildmat.2022.127270. doi:10.1016/j.conbuildmat.2022.127270.

S. Mahjoubi, W. Meng, Y. Bao, Auto-tune learning framework for prediction of flowability, mechanical properties, and porosity of ultra- high-performance concrete (UHPC), volume 115, Applied Soft Computing, 2022, p. 108182. URL: http://dx.doi.org/10.1016/j.asoc.2021.108182. doi:10.1016/j.asoc.2021.108182.

E. M. Golafshani, A. Behnood, T. Kim, T. Ngo, A. Kashani, A framework for low-carbon mix design of recycled aggregate concrete with supplementary cementitious materials using machine learning and optimization algorithms, volume 61, Structures, 2024, p. 106143. URL: http://dx.doi.org/10.1016/j.istruc.2024.106143. doi:10.1016/j.istruc.2024.106143.

Z. Li, J. Yoon, R. Zhang, F. Rajabipour, W. V. Srubar III, I. Dabo, A. Radlińska, Machine learning in concrete science: applications, challenges, and best practices, volume 8, npj Computational Materials, 2022. URL: http://dx.doi.org/10.1038/s41524-022-00810-x. doi:10.1038/s41524-022-00810-x.

F. Rezazadeh P., A. Dürrbaum, G. Zimmermann, A. Kroll, Holistic modeling of ultra-high performance concrete production process: Synergizing mix design, fresh concrete properties, and curing conditions, 33. Workshop Computational Intelligence, 2023, pp. 215–237. URL: http://dx.doi.org/10.58895/ksp/1000162754-15. doi:10.58895/ksp/1000162754-15.

P. Chopra, R. K. Sharma, M. Kumar, Prediction of compressive strength of concrete using artificial neural network and genetic programming, volume 2016, Advances in Materials Science and Engineering, 2016, pp. 1–10. URL: http://dx.doi.org/10.1155/2016/7648467. doi:10.1155/2016/7648467.

R. Mustapha, E. A. Mohamed, High-performance concrete compressive strength prediction based weighted support vector machines, volume 07, International Journal of Engineering Research and Applications, 2017, pp. 68–75. URL: http://dx.doi.org/10.9790/9622-0701016875. doi:10.9790/9622-0701016875.

T. T. Nguyen, L. T. Ngoc, H. H. Vu, T. P. Thanh, Machine learning-based model for predicting concrete compressive strength, volume 20, International Journal of GEOMATE, 2021, pp. 197–204. URL: http://dx.doi.org/10.21660/2020.77.j2019. doi:10.21660/2020.77.j2019.

R. Rajeshwari, S. Mandal, Prediction of compressive strength of high-volume fly ash concrete using artificial neural network, Sustainable Construction and Building Materials, 2018, pp. 471–483. URL: http://dx.doi.org/10.1007/978-981-13-3317-0_42. doi:10.1007/978-981-13-3317-0_42.

P. Chopra, R. Sharma, M. Kumar, Ridge regression for the prediction of compressive strength of concrete, volume 2, Int. J. Innov. Eng. Technol, 2013, pp. 106–111.

K. Güçlüer, A. Özbeyaz, S. Göymen, O. Günaydın, A comparative investigation using machine learning methods for concrete compressive strength estimation, volume 27, Materials Today Communications, 2021, p. 102278. URL: http://dx.doi.org/10.1016/j.mtcomm.2021.102278. doi:10.1016/j.mtcomm.2021.102278.

H. Naderpour, A. H. Rafiean, P. Fakharian, Compressive strength prediction of environmentally friendly concrete using artificial neural networks, volume 16, Journal of Building Engineering, 2018, pp. 213–219. URL: http://dx.doi.org/10.1016/j.jobe.2018.01.007. doi:10.1016/j.jobe.2018.01.007.

I. B. Topcu, M. Sarıdemir, Prediction of compressive strength of concrete containing fly ash using artificial neural networks and fuzzy logic, volume 41, Computational Materials Science, 2008, pp. 305–311. URL: http://dx.doi.org/10.1016/j.commatsci.2007.04.009. doi:10.1016/j.commatsci.2007.04.009.

J. Sun, J. Zhang, Y. Gu, Y. Huang, Y. Sun, G. Ma, Prediction of permeability and unconfined compressive strength of pervious concrete using evolved support vector regression, volume 207, Construction and Building Materials, 2019, pp. 440–449. URL: http://dx.doi.org/10.1016/j.conbuildmat.2019.02.117. doi:10.1016/j.conbuildmat.2019.02.117.

R. Kumar, B. Rai, P. Samui, A comparative study of prediction of compressive strength of ultra-high performance concrete using soft computing technique, volume 24, Structural Concrete, 2023, pp. 5538–5555. URL: http://dx.doi.org/10.1002/suco.202200850. doi:10.1002/suco.202200850.

M. K. Keleş, A. E. Keleş, Ü. Kiliç, Prediction of concrete strength with data mining methods using artificial bee colony as feature selector, 2018 International Conference on Artificial Intelligence and Data Processing (IDAP), 2018, pp. 1–4. URL: http://dx.doi.org/10.1109/idap.2018.8620905. doi:10.1109/idap.2018.8620905.

T. Nguyen, A. Kashani, T. Ngo, S. Bordas, Deep neural network with high-order neuron for the prediction of foamed concrete strength, volume 34, Computer-Aided Civil and Infrastructure Engineering, 2018, pp. 316–332. URL: http://dx.doi.org/10.1111/mice.12422. doi:10.1111/mice.12422.

J. Zhang, G. Ma, Y. Huang, J. sun, F. Aslani, B. Nener, Modelling uniaxial compressive strength of lightweight self-compacting concrete using random forest regression, volume 210, Construction and Building Materials, 2019, pp. 713–719. URL: http://dx.doi.org/10.1016/j.conbuildmat.2019.03.189. doi:10.1016/j.conbuildmat.2019.03.189.

A. Sharafati, S. B. Haji Seyed Asadollah, N. Al-Ansari, Application of bagging ensemble model for predicting compressive strength of hollow concrete masonry prism, volume 12, Ain Shams Engineering Journal, 2021, pp. 3521–3530. URL: http://dx.doi.org/10.1016/j.asej.2021.03.028. doi:10.1016/j.asej.2021.03.028.

N.-D. Hoang, A.-D. Pham, Q.-L. Nguyen, Q.-N. Pham, Estimating compressive strength of high performance concrete with Gaussian process regression model, volume 2016, Advances in Civil Engineering, 2016, pp. 1–8. URL: http://dx.doi.org/10.1155/2016/2861380. doi:10.1155/2016/2861380.

N. K. Nagwani, S. V. Deo, Estimating the concrete compressive strength using hard clustering and fuzzy clustering based regression techniques, volume 2014, The Scientific World Journal, 2014, pp. 1–16. URL: http://dx.doi.org/10.1155/2014/381549. doi:10.1155/2014/381549.

D. Chakraborty, I. Awolusi, L. Gutierrez, An explainable machine learning model to predict and elucidate the compressive behavior of high-performance concrete, volume 11, Results in Engineering, 2021, p. 100245. URL: http://dx.doi.org/10.1016/j.rineng.2021.100245. doi:10.1016/j.rineng.2021.100245.

A. Kandiri, F. Sartipi, M. Kioumarsi, Predicting compressive strength of concrete containing recycled aggregate using modified ann with different optimization algorithms, volume 11, Applied Sciences, 2021, p. 485. URL: http://dx.doi.org/10.3390/app11020485. doi:10.3390/app11020485.

P. Refaeilzadeh, L. Tang, H. Liu, Cross-validation, Encyclopedia of Database Systems, 2009, pp. 532–538. URL: http://dx.doi.org/10.1007/978-0-387-39940-9_565. doi:10.1007/978-0-387-39940-9_565.

J. Li, K. Cheng, S. Wang, F. Morstatter, R. P. Trevino, J. Tang, H. Liu, Feature selection: A data perspective, volume 50, ACM computing surveys (CSUR), 2017, pp. 1–45.

B. Ahadzadeh, M. Abdar, F. Safara, A. Khosravi, M. B. Menhaj, P. N. Suganthan, SFE: A simple, fast, and efficient feature selection algorithm for high-dimensional data, volume 27, IEEE Transactions on

Evolutionary Computation, 2023, pp. 1896–1911. URL: http://dx.doi.org/10.1109/tevc.2023.3238420. doi:10.1109/tevc.2023.3238420.

L. Li, M. Xuan, Q. Lin, M. Jiang, Z. Ming, K. C. Tan, An evolutionary multitasking algorithm with multiple filtering for high-dimensional feature selection, volume 27, IEEE Transactions on Evolutionary Computation, 2023, pp. 802–816. URL: http://dx.doi.org/10.1109/tevc.2023.3254155. doi:10.1109/tevc.2023.3254155.

K. Chen, B. Xue, M. Zhang, F. Zhou, Evolutionary multitasking for feature selection in high-dimensional classification via particle swarm optimization, volume 26, IEEE Transactions on Evolutionary Computation, 2022, pp. 446–460. URL: http://dx.doi.org/10.1109/tevc.2021.3100056. doi:10.1109/tevc.2021.3100056.

K. Chen, B. Xue, M. Zhang, F. Zhou, An evolutionary multitasking-based feature selection method for high-dimensional classification, volume 52, IEEE Transactions on Cybernetics, 2022, pp. 7172–7186. URL: http://dx.doi.org/10.1109/tcyb.2020.3042243. doi:10.1109/tcyb.2020.3042243.

J. Luo, D. Zhou, L. Jiang, H. Ma, A particle swarm optimization based multiobjective memetic algorithm for high-dimensional feature selection, volume 14, Memetic Computing, 2022, pp. 77–93. URL: http://dx.doi.org/10.1007/s12293-022-00354-z. doi:10.1007/s12293-022-00354-z.

L. von Rueden, S. Mayer, K. Beckh, B. Georgiev, S. Giesselbach, R. Heese, B. Kirsch, M. Walczak, J. Pfrommer, A. Pick, R. Ramamurthy, J. Garcke, C. Bauckhage, J. Schuecker, Informed machine learning - a taxonomy and survey of integrating prior knowledge into learning systems, IEEE Transactions on Knowledge and Data Engineering, 2021, pp. 614–633. URL: http://dx.doi.org/10.1109/tkde.2021.3079836. doi:10.1109/tkde.2021.3079836.

I. Kropp, A. P. Nejadhashemi, K. Deb, Benefits of sparse population sampling in multi-objective evolutionary computing for large-scale sparse optimization problems, volume 69, Swarm and Evolutionary Computation, 2022, p. 101025. URL: http://dx.doi.org/10.1016/j.swevo.2021.101025. doi:10.1016/j.swevo.2021.101025.

H. Xu, B. Xue, M. Zhang, A duplication analysis-based evolutionary algorithm for biobjective feature selection, volume 25, IEEE Transactions on Evolutionary Computation, 2021, pp. 205–218. URL: http://dx.doi.org/10.1109/tevc.2020.3016049. doi:10.1109/tevc.2020.3016049.

X.-F. Song, Y. Zhang, D.-W. Gong, X.-Z. Gao, A fast hybrid feature selection based on correlation-guided clustering and particle swarm optimization for high-dimensional data, volume 52, IEEE Transactions on Cybernetics, 2022, pp. 9573–9586. URL: http://dx.doi.org/10.1109/tcyb.2021.3061152. doi:10.1109/tcyb.2021.3061152.

J. Ren, F. Qiu, H. Hu, Multiple sparse detection-based evolutionary algorithm for large-scale sparse multiobjective optimization problems, volume 9, Complex and Intelligent Systems, 2023, pp. 4369–4388. URL: http://dx.doi.org/10.1007/s40747-022-00963-8. doi:10.1007/s40747-022-00963-8.

P. Wang, B. Xue, J. Liang, M. Zhang, Multiobjective differential evolution for feature selection in classification, volume 53, IEEE Transactions on Cybernetics, 2023, pp. 4579–4593. URL: http://dx.doi.org/10.1109/tcyb.2021.3128540. doi:10.1109/tcyb.2021.3128540.

F. Rezazadeh P., A. Abrishambaf, A. Dürrbaum, G. Zimmermann, A. Kroll, Systematic data generation to study measurement errors and environmental impacts on ultra-high performance concrete, Submitted, Unpublished Results.

A. Dürrbaum, F. Rezazadeh P., A. Kroll, Automatic camera-based advanced slump flow testing for improved reliability, 2023 IEEE SENSORS, 2023, pp. 1–4. URL: http://dx.doi.org/10.1109/sensors56945.2023.10325030. doi:10.1109/sensors56945.2023.10325030.

G. Taguchi, System of experimental design; engineering methods to optimize quality and minimize costs, New York: UNIPUB/Kaus International, 1987.

M. Stein, Large sample properties of simulations using Latin hypercube sampling, volume 29, Technometrics, 1987, p. 143. URL: http://dx.doi.org/10.2307/1269769. doi:10.2307/1269769.

M. Mitchell, Genetic algorithms: An overview, An Introduction to Genetic Algorithms, 1998, pp. 31–39.

URL: http://dx.doi.org/10.7551/mitpress/3927.003.0003. doi:10.7551/mitpress/3927.003.0003.

A. Hedayat, Study of optimality criteria in design of experiments, Statistics and Related Topics, North-Holland Publishing Company, 1981, pp. 39–56.

J. Benesty, J. Chen, Y. Huang, I. Cohen, Pearson correlation coefficient, Springer Topics in Signal Processing, 2009, pp. 1–4. URL: http://dx.doi.org/10.1007/978-3-642-00296-0_5. doi:10.1007/978-3-642-00296-0_5.

A. R. T. Donders, G. J. van der Heijden, T. Stijnen, K. G. Moons, Review: A gentle introduction to imputation of missing values, volume 59, Journal of Clinical Epidemiology, 2006, pp. 1087–1091. URL: http://dx.doi.org/10.1016/j.jclinepi.2006.01.014. doi:10.1016/j.jclinepi.2006.01.014.

O. Troyanskaya, M. Cantor, G. Sherlock, P. Brown, T. Hastie, R. Tibshirani, D. Botstein, R. B. Altman, Missing value estimation methods for DNA microarrays, volume 17, Bioinformatics, 2001, pp. 520–525. URL: http://dx.doi.org/10.1093/bioinformatics/17.6.520. doi:10.1093/bioinformatics/17.6.520.

S. F. Buck, A method of estimation of missing values in multivariate data suitable for use with an electronic computer, volume 22, Journal of the Royal Statistical Society: Series B (Methodological), 1960, pp. 302–306. URL: http://dx.doi.org/10.1111/j.2517-6161.1960.tb00375.x. doi:10.1111/j.2517-6161.1960.tb00375.x.

S. v. Buuren, K. Groothuis-Oudshoorn, mice: Multivariate imputation by chained equations inr, volume 45, Journal of Statistical Software, 2011, pp. 1–67. URL: http://dx.doi.org/10.18637/jss.v045.i03. doi:10.18637/jss.v045.i03.

R. J. Little, D. B. Rubin, Statistical analysis with missing data, volume 793, John Wiley & Sons, 2019.

F. Pedregosa, G. Varoquaux, A. Gramfort, V. Michel, B. Thirion, O. Grisel, M. Blondel, P. Prettenhofer, R. Weiss, V. Dubourg, et al., Scikit-learn: Machine learning in python, volume 12, Journal of Machine Learning Research, 2011, pp. 2825–2830.

C. M. Bishop, N. M. Nasrabadi, Pattern recognition and machine learning, volume 4, Springer, 2006.

D. J. C. MacKay, Bayesian Interpolation, Maximum Entropy and Bayesian Methods, 1992, pp. 39–66. URL: http://dx.doi.org/10.1007/978-94-017-2219-3_3. doi:10.1007/978-94-017-2219-3_3.

M. E. Tipping, Sparse Bayesian learning and the relevance vector machine, volume 1, Journal of machine learning research, 2001, pp. 211–244.

A. Smiti, A critical overview of outlier detection methods, volume 38, Computer Science Review, 2020, p. 100306. URL: http://dx.doi.org/10.1016/j.cosrev.2020.100306. doi:10.1016/j.cosrev.2020.100306.

X. Su, C.-L. Tsai, Outlier detection, volume 1, Wiley Interdisciplinary Reviews: Data Mining and Knowledge Discovery, 2011, pp. 261–268.

V. Hodge, J. Austin, A survey of outlier detection methodologies, volume 22, Artificial Intelligence Review, 2004, pp. 85–126. URL: http://dx.doi.org/10.1023/b:aire.0000045502.10941.a9. doi:10.1023/b:aire.0000045502.10941.a9.

U. Habib, G. Zucker, M. Blochle, F. Judex, J. Haase, Outliers detection method using clustering in buildings data, IECON 2015 - 41st Annual Conference of the IEEE Industrial Electronics Society, 2015. URL: http://dx.doi.org/10.1109/iecon.2015.7392181. doi:10.1109/iecon.2015.7392181.

A. Boukerche, L. Zheng, O. Alfandi, Outlier detection: Methods, models, and classification, volume 53, ACM Computing Surveys, 2020, pp. 1–37. URL: http://dx.doi.org/10.1145/3381028. doi:10.1145/3381028.

H. Wang, M. J. Bah, M. Hammad, Progress in outlier detection techniques: A survey, volume 7, IEEE Access, 2019, pp. 107964–108000. URL: http://dx.doi.org/10.1109/access.2019.2932769. doi:10.1109/access.2019.2932769.

O. Sagi, L. Rokach, Ensemble learning: A survey, volume 8, WIREs Data Mining and Knowledge Discovery, 2018. URL: http://dx.doi.org/10.1002/widm.1249. doi:10.1002/widm.1249.

A. Krogh, J. Vedelsby, Neural network ensembles, cross validation, and active learning, volume 7, Advances in neural information processing systems, 1994.

D. Wood, T. Mu, A. M. Webb, H. W. Reeve, M. Lujan, G. Brown, A unified theory of diversity in ensemble learning, volume 24, Journal of Machine Learning Research, 2023, pp. 1–49.

J. Surowiecki, The wisdom of crowds, Anchor, 2005.

K. Deb, A. Pratap, S. Agarwal, T. Meyarivan, A fast and elitist multiobjective genetic algorithm: NSGA-II, volume 6, IEEE Transactions on Evolutionary Computation, 2002, pp. 182–197. URL: http://dx.doi.org/10.1109/4235.996017. doi:10.1109/4235.996017.

N. Gunantara, A review of multi-objective optimization: Methods and its applications, volume 5, Cogent Engineering, 2018, p. 1502242. URL: http://dx.doi.org/10.1080/23311916.2018.1502242. doi:10.1080/23311916.2018.1502242.

F. Pedregosa, G. Varoquaux, A. Gramfort, V. Michel, B. Thirion, O. Grisel, et al., Scikit-learn: Machine learning in Python, volume 12, 2011, pp. 2825–2830.

J. A. Wegelin, et al., A survey of partial least squares (PLS) methods, with emphasis on the two-block case, University of Washington, Tech. Rep, 2000.

K. P. Murphy, Machine learning: a probabilistic perspective, MIT press, 2012.

E. Fix, J. L. Hodges, Discriminatory analysis. nonparametric discrimination: Consistency properties, volume 57, International Statistical Review / Revue Internationale de Statistique, 1989, p. 238. URL: http://dx.doi.org/10.2307/1403797. doi:10.2307/1403797.

C.-C. Chang, A library for support vector machines, 2023. URL: https://www.csie.ntu.edu.tw/~cjlin/libsvm/.

M. Dumont, R. Marée, L. Wehenkel, P. Geurts, VISAPP, Proceedings of the Fourth International Conference on Computer Vision Theory and Applications, 2009. URL: http://dx.doi.org/10.5220/0001800001960203. doi::10.5220/0001800001960203.

L. Breiman, Random forests, volume 45, Machine learning, 2001, pp. 5–32.

J. H. Friedman, Greedy function approximation: a gradient boosting machine, JSTOR, 2001, pp. 1189–1232.

T. Chen, C. Guestrin, Xgboost: A scalable tree boosting system, Proceedings of the 22nd ACM SIGKDD International Conference on Knowledge Discovery and Data Mining, 2016, pp. 785–794. URL: http://dx.doi org/10 1145/2939672 . doi...2939785:10.1145/ 2939672.2939785.

C. E. Rasmussen, Gaussian processes in machine learning, Summer school on machine learning, 2003, pp. 63–71.

Z. Ge, Z. Song, S. X. Ding, B. Huang, Data mining and analytics in the process industry: The role of machine learning, volume 5, IEEE Access, 2017, p. 20590–20616. URL:http://dx.doi.org/10.1109/access.2017.2756872. doi:10.1109/access.2017.2756872.

Publication Ethics and Malpractice Statement

The *Artificial Intelligence and Sustainable Materials Journal* is an academic journal published by Mason Publish Group. It is necessary to agree upon standards of expected ethical behavior for all parties involved in the act of publishing: the journal editor, the author, the peer reviewer and the publisher. This ethic statement is based on COPE's Best Practice Guidelines for Journal Editors.

Duties of Editor

- The evaluation should be objective and fair, and give clear opinions on whether it meets the standards of public publication.
- Ensure that journals are published on time and on schedule, and prevent plagiarism and repeated publication of papers.
- According to the importance, originality and relevance of the paper to the journal, the author has the right to reject and accept the paper, and allows the author to appeal the review decision.
- The editor shall ensure that all research material they publish conforms to internationally accepted ethical guidelines.

Duties of Authors

- Authors have to make sure that they write completely original works that have not been published elsewhere before.
- The data of the paper is authentic and reliable, and forgery, tampering and plagiarism are prohibited.
- Reference information shall be indicated when quoting opinions.
- The author shall ensure that the published paper is authorized and approved by the coauthor, and there is no signed dispute.
- All authors must contribute to the research of the paper.
- The author shall provide the original data related to his manuscript for the editor's review, and must keep these data.

Duties of Reviewers

In the process of review, the reviewer shall be objective and keep all information of the paper confidential. Reviewers must ensure that the author has identified all data sources used in the study. If invited to review a paper, it shall be completed within the specified time.

Duties of Advisory Board Members

The advisory board is composed of distinguished scholars and professors in the field of electrical and electronic engineering. Members can review submitted manuscripts, identify topics for special issues, or attract new authors and submissions as necessary.

Artificial Intelligence and Sustainable Materials

Call for Papers

Artificial Intelligence is a cutting-edge cross-cutting field driving scientific and technological innovation, while sustainable materials research is a core pathway to solving global resource and environmental challenges. The deep integration of the two is providing disruptive solutions for green manufacturing, energy transition and circular economy. Artificial Intelligence and Sustainable Materials is dedicated to building an interdisciplinary communication platform, focusing on the empowering role of AI in materials innovation, environmental monitoring and resource optimization, and inviting researchers from all over the world to share theoretical breakthroughs and practical cases.

Call for Reviewers

In order to further improve the academic level and quality of the journal, enrich the team of reviewers and implement the anonymous reviewer system, the editorial department is now calling for reviewers. We welcome experts and scholars in the fields of the Artificial Intelligence and Sustainable Materials to recommend themselves or recommend suitable candidates, so as to jointly promote the progress and development of periodicals. Please contact us (masonpublish@gmail.com) if you are interested.